OXYGEN REDUCTION REACTION ON CARBON SUPPORTED DISPERSED PLATINUM NANOPARTICLES AND EXTENDED PLATINUM SURFACES

University of Cape Town

Dissertation

Submitted in partial fulfilment of the requirements for the degree of
Master of Science in Chemical Engineering

Prepared by:
Susan M. Taylor

Prepared for:
Dr. Olaf Conrad
Dr. Pieter B.J. Levecque

Department of Chemical Engineering
National Hydrogen Catalysis Competence Centre
University of Cape Town

August 2013

The copyright of this thesis vests in the author. No quotation from it or information derived from it is to be published without full acknowledgement of the source. The thesis is to be used for private study or non-commercial research purposes only.

Published by the University of Cape Town (UCT) in terms of the non-exclusive license granted to UCT by the author.

University of Cape Town

SYNOPSIS

To date, the cost of high platinum loadings in polymer electrolyte fuel cells (PEFCs) remains one of the main deterrents preventing their broad commercialisation. The reaction of interest in this work is the oxygen reduction reaction (ORR) occurring at the cathode side of the PEFC. The ORR has been studied at great length owing to the sluggish kinetics of this reaction and thus the necessity of the higher platinum loadings required on the cathode side of the PEFC. Platinum particle size and surface morphology are thought to be directly related to the catalytic activity of platinum towards the ORR (Mayrhofer *et al.*, 2005) A better understanding of the effects of platinum particle size and surface morphology on the mechanism and kinetics of the ORR is critical if platinum loadings are to be reduced whilst maintaining the US Department of Energy (DoE) target performance levels (Schwanitz *et al.*, 2012).

This study focuses on the effects of platinum surface morphology on ORR activity by the development of platinum supported carbon electrodes. The surface morphology was modified by varying the platinum loading, such that the surface was taken from isolated nanoparticles to an extended surface. The effects of the changes in surface morphology and particle size on the ORR were then investigated. First a model electrode system was developed by magnetron sputter deposition of platinum onto a carbon black (VulcanXC72) surface supported on a glassy carbon electrode. The model system was then translated into a practical system, whereby platinum supported on carbon catalysts were prepared by metal-organic chemical vapour deposition (MOCVD) with increasing weight percentages of platinum. Similar trends were observed for the MOCVD catalyst system and the model electrode system. The trends of particular interest were the effects of platinum loading on hydrogen peroxide formation during the ORR and the double voltammeric CO oxidation peak observed with increased platinum loading during CO stripping voltammetry experiments.

Hydrogen peroxide formation was observed at potentials below 0.8 V vs. SHE/RHE and it was found that hydrogen peroxide formation was predominant on dispersed platinum nanoparticles compared with platinum agglomerates. This is most likely related to peroxide species, a partial reduction product from oxygen to water, being able to desorb from the active surface without being further reduced to water on an adjacent site as the inter-particle distance is greater for the low loading samples relative to the higher loading samples in both systems.

University of Cape Town

A clear indication of differing surface morphology between the low and high loading samples was observed by the double voltammeric peak detected during CO stripping voltammetry experiments. The low potential peak attributed to platinum agglomerates was seen to increase in amplitude as platinum loading increased. The corresponding high potential peak attributed to isolated nanoparticles, decreased in amplitude with increasing platinum loading. This observation alludes to an increase in particle agglomeration with platinum loading, and physical characterisation methods such as TEM and XRD showed an increase in the average particle size with increasing platinum loading, which supports the CO stripping voltammetry findings.

The findings indicate a profound dependence of the ORR on platinum particle size and surface morphology. A better insight into these properties could assist in improved catalyst design and the enhancement of platinum utilisation and ORR activity of platinum.

University of Cape Town

ACKNOWLEDGEMENTS

The past 18 months of my life have been filled with new experiences and new people who have supported and guided me through this phase of my life, and to whom I owe sincere gratitude.

Olaf Conrad for inspiring me right from the very beginning of my journey to join HySA catalaysis. Your passion and knowledge for fuel cells and electrochemistry honestly inspired and excited me about my own work. Your personable and kind natured approach to supervising made it a very happy working environment. I am especially grateful for the opportunity I had to spend a part of my studies overseas, which opened so many doors for me and I have you to thank for that and I will never forget that.

I would like to thank Pieter Levecque for his unfailing patience, encouragement and invaluable input throughout my work. You would never hesitate to drop what you were doing to help or guide me You noticed when I was down and struggling, you helped encourage me and show me that the end was in sight. You have such a big heart, and I am so grateful to have had a supervisor as approachable and caring as you. I honestly couldn't have done it without you Pieter, thank you.

Thomas Schmidt who hosted me at PSI and gave me such a wonderful opportunity to experience world class facilities and learn from the best. Thank you.

Guenther Scherer for your generosity and kindness. It was such a comfort to see a familiar face the day you fetched me from the airport in Switzerland, when I was really quite terrified to be in a new place and felt quite alone. You were so kind and helpful in getting me settled in and I am honestly so grateful for that kind hand, and it will never be forgotten, danke!

Nabeel Hussain who was always available for any query or question and was always willing to give assistance and much appreciated advice, thank you.

Archie Fortuin, who helped me save time with my experimental work by making the right mistakes before me. Thank you for your support and help with my write-up.

My PSI family,who were all so welcoming and kind and made me feel a part of the group from day one, thank you.

University of Cape Town

Emilianna who looked after me so well and never once made me feel out of place, you truly are an inspiration to me, from your amazing achievements to your kind heart and a smile that puts everyone in a good mood, thank you.

Mohammed Jaffer for efficiently analysing my samples under TEM and always making time for me, thank you.

Subelia for the time and effort I know you spent analysing my samples, it is much appreciated and the results were beautiful.

Cobus van der Merwe thank you for your patience with my continuous nagging about my reactor. I appreciate all your time and help.

Thank you to my friends Colleen, Catherine and Nicolas for their much appreciated support.

Last but not least my family, my parents, brother and sister, who have consistently supported me throughout my studies. Your love and support has not gone unnoticed.

University of Cape Town

TABLE OF CONTENTS

University of Cape Town

University of Cape Town

University of Cape Town

University of Cape Town

LIST OF FIGURES

University of Cape Town

University of Cape Town

University of Cape Town

University of Cape Town

University of Cape Town

University of Cape Town

LIST OF TABLES

University of Cape Town

NOMENCLATURE

Symbols

Symbol	Unit	Description
A_E	cm^2	Electrode area
a	%	Fraction carbon surface available
B	$C.cm^3/mol.s^{1/2}$	Grouped constant with a value of $0.620nFAD^{2/3}\nu^{-1/6}$
C	mol/cm^3	Reactant concentration
D	cm^2/s	Diffusion co-efficient
d_c	cm	Diameter carbon particle
d_{Pt}	cm	Diameter platinum particle
$d_{(C+Pt)}$	cm	Diameter carbon + platinum particle
d_E	cm	Diameter electrode
i	mA/cm^2	Current density
i_d	mA/cm^2	Diffusion limiting current density
i_k	mA/cm^2	Kinetic current density
$i_{k\ (0.9\ V)}$	mA/cm^2	Kinetic current density at 0.9 V vs RHE/SHE
i_{2e-}	mA/cm^2	2 electron current density
i_{4e-}	mA/cn^2	4 electron current density
i_{Disk}	mA/cm^2	Disk current density
i_{Ring}	mA/cm^2	Ring current density
$i_{k,\ mass}$	mA/cm^2	Mass specific activity

University of Cape Town

$i_{k,\ mass\ (0.9\ V)}$	mA/cm^2	Mass specific activity at 0.9 V vs. RHE/SHE
$i_{k,\ spec}$	mA/cm^2	Area specific activity
$i_{k,\ spec\ (0.9\ V)}$	mA/cm^2	Area specific activity at 0.9 V vs. RHE/SHE
<L>	nm	Average crystallite size
$m_{Pt,\ total}$	g	Total mass of platinum on electrode surface
$m_{C,\ total}$	g	Total mass of carbon on electrode surface
$m_{Pt,\ loading}$	$\mu g/cm^2$	Platinum loading on electrode surface
n	-	Number of electrons
N	%	Collection efficiency of the ring
n_C	-	Number of carbon particles
r_C	cm	Radius of a carbon particle
r_{Pt}	cm	Radius of a platinum particle
$r_{(Pt+C)}$	cm	Radius of a carbon particle and platinum particle
r_E	cm	Radius of electrode
SA_C	cm^2	Surface area of a carbon particle
$SA_{C,\ total}$	cm^2	Total surface area of carbon particles
$SA_{Pt,film}$	cm^2	Surface area of a platinum film covering a carbon particle
$SA_{Pt,\ total}$	cm^2	Total surface area of platinum films on n_c carbon particles
V_C	cm^3	Volume of a carbon particle
$V_{(Pt+C)}$	cm^3	Volume of a carbon particle covered in a platinum film
$V_{Pt\ film}$	cm^3	Volume of a platinum film covering a carbon particle
$V_{Pt,\ total}$	cm^3	Total volume of platinum films covering n_C carbon particles

University of Cape Town

$V_{C,\,total}$	cm^3	Total volume of carbon particles
$X_{H_2O_2}$	%	Percentage hydrogen peroxide (H_2O_2) formed on the ring relative to the total current
w_{Pt}	%	Weight percent platinum supported on carbon
ω	rpm	Rotation speed of the electrode
ν	cm^2/s	Kinematic viscosity
λ	nm	X-ray wavelength
θ	radians	Bragg angle
β	-	Peak width

Constants

Constant	Value	Units	Description
ρ_C	1.8	g/cm^3	Density of Vulcan XC72
ρ_{Pt}	21.46	g/cm^3	Density of platinum metal
F	96 485	C/mol	Faraday's constant
K	1	-	Dimensionless crystallite shape factor
rf	1.8	-	Roughness factor of paltinum

University of Cape Town

GLOSSARY

Abbreviation	Description
ALE	Atomic layer epitaxy
ALD	Atomic layer deposition
ads	adsorption
CVD	Chemical vapour deposition
CV	Cyclic voltammetry
DL	Double layer
DFT	Density function theory
ECSA	Electrochemically active surface area
EIS	Electrochemical impedence spectroscopy
ESA	Extended surface area
GC	Glassy carbon
HSA	High surface area
LSV	Linear sweep voltammetry
MAD	Mass average distribution
MOCVD	Metal-organic chemical vapour deposition
MPL	Microporous layer
NSTF	Nanostructured thin film
ORR	Oxygen reduction reaction
PVD	Physical vapour deposition
PCVD	Plasma enhanced chemical vapour deposition

University of Cape Town

pztc	Potential of zero total charge
Pt/C	Platinum supported on carbon
PSI	Paul Scherrer Institute
PEFC	Polymer electrolyte fuel cell
RHE	Reversible hydrogen electrode
RDE	Rotating disk electrode
RRDE	Rotating ring disk electrode
SEM	Scanning electron microscope
STEM	Scanning transmission electron microscopy
SHE	Standard hydrogen electrode
TEM	Transmission electron microscopy
TGA	ThermoGravimteric analysis
upd	Under potential deposition
XRD	X-ray diffraction

University of Cape Town

1. INTRODUCTION

The growing scarcity of fossil fuels and the increase in green-house gas emissions over the past decade has created the need for an alternative source of clean energy. Polymer electrolyte fuel cells (PEFCs) play a critical role in most future energy solutions and have the potential for higher efficiencies compared to internal combustion engines (Karakoc *et al.*, 2013). Fuel cell development itself is shifting quickly from fundamental research to practical development (Rabis *et al*., 2012).

A critical component of a PEFC is the platinum based electrocatalyst. South Africa is known to possess approximately 80% of the world's platinum reserves (US Geological Survey, 2010). In recognition of this fact the Department of Science and Technology (DST) in South Africa have set up Hydrogen South Africa (HySA) - a homegrown hydrogen and fuel cell technology organisation which focuses on catalysis, systems and infrastructure. HySA has been established to ambitiously capture 25% of the global catalyst market by 2020 (Fuel Cell Today, 2013).

At the recent biennial conference *Hydrogen + Fuel cells* held in Vancouver in June 2013, Anglo American Platinum (AAP) in collaboration with Ballard Power Systems committed to provide renewable methanol powered fuel cell electricity to support rural African residences by 2014. If successful, this joint venture could see full commercialisation of more than 7000 units by 2016 (Fuel Cell Today, 2013). South Africa and HySA have the potential to contribute significantly to the world wide hydrogen economy. It is therefore prudent that extensive research into the current challenges associated with PEFCs is undertaken by the research and development sector of HySA, namely the Hydrogen Catalysis Competence Centre (HySA/Catalysis). HySA/Catalysis is hosted by the University of Cape Town Chemical Engineering Department and South Africa's national Minerals Research Council, Mintek.

Platinum is the catalyst of choice used to enhance the electrochemical reactions occurring in PEFCs. Recent achievements in the field of electrochemistry and catalyst development have led to a significant decrease in the amount of precious metal used in the catalyst layer of PEFCs (Zhang *et al*., 2013). The oxygen reduction reaction (ORR) is the most extensively researched electrochemical reaction in this field and remains a serious challenge to PEFC commercialisation. Issues such as the effect of platinum particle size on the ORR kinetics and hydrogen peroxide formation must be fully understood in order to optimise the catalyst performance. Research into platinum based catalyst development has shifted from isolated supported nanoparticles to extended platinum surfaces. Advantages associated with thinner catalyst layers and improved catalytic activity have meant that companies such as 3M have invested significantly in extended surface platinum type catalysts. 3M's

University of Cape Town

novel nanostructured thin film (NSTF) catalyst is based on an extended platinum surface and has been proven to display superior performance compared with conventional supported nanoparticle catalysts (Debe, 2012).

Further insight into the challenges associated with platinum electrocatalysts will ultimately allow PEFCs to become a cost competitive energy conversion device for portable, automotive and stationary applications.

University of Cape Town

2. LITERATURE REVIEW

2.1 Current state of the art catalysts and catalyst requirements

Platinum and its alloys are the most commonly used catalysts for fuel cell applications, as platinum offers the highest catalytic activity, chemical stability, high exchange current density and superior work function compared to other metals (Sharma and Pollet, 2012). However, the main shortcoming of using platinum as the catalyst, is the global scarcity of the mineral and hence the cost.

The United States Department of Energy (DoE) is generally regarded at setting the targets for fuel cell performance adopted by researchers around the world. Table 2.1 below shows a comparison of the DoE targets for 2017 and 2020 for PEFCs.

Table 2.1 : Progress towards meeting DOE targets (Adapted from U.S. Department of Energy, 2011)

Characteristic	Units	2011 Status	Targets	
			2017	2020
Platinum group metal total content (both electrodes)	g/kW (rated)	0.19	0.125	
Platinum group metal total Loading	mg PGM/cm^2 electrode area	0.15	0.125	
Loss in initial catalytic activity	% mass activity loss	48	<40	
Electro catalyst support Stability	% mass activity loss	<10	<10	
Mass activity	A/mg Pt @ 900 $mV_{iR\text{-}free}$	0.24	0.44	
Non-Pt catalyst activity per volume of supported catalyst	A/cm^3 @ 800 $mV_{iR\text{-}free}$	60 (@0.8 V) 165 (extrapolated from >0.85 V)	300	

In a landmark study by Gasteiger *et al*. (2005) the performance of a range of commercial catalysts was investigated. This was done both by in-situ fuel cell testing as well as ex-situ rotating disk electrode (RDE) testing. The materials included in the study were from typical manufacturers such as Johnson-Matthey (JM), Tanaka Kikinzuko Kogyo (TKK) and ETEK. The mass activity $i_{mass\ (0.9V)}$ for a 20 wt.% Pt catalyst ranged from 0.029 to 0.16 A/mg_{Pt}. Although not so recent, the study is still used as a guide for fuel cell catalyst researchers, both from the point of view of the methodology employed as well as the benchmark values obtained.

University of Cape Town

2.2 Carbon supported platinum catalysts

2.2.1 Motivation for supported nanoparticles

The earliest catalyst layer preparation methods for PEFCs was based on high platinum loadings of 4 mg_{Pt}/cm^2 dispersed on the membrane itself (Barbir, 2005). The degree of platinum dispersion in this case is limited to what can be achieved with platinum black, which has a minimum particle size of 10 nm (Gottesfeld and Zawodzinski, 1997). This mode of catalyst layer preparation results in a low catalyst utilisation originating form inefficient use of the available metal.

The platinum loading was reduced from 4 mg_{Pt}/cm^2 to 0.3-0.4 mg_{Pt}/cm^2 by supporting platinum nanoparticles on carbon black (Barbir, 2005). Platinum particle sizes of 2 nm are easily achieved when supported on typical carbon support particles such as Vulcan XC72 with an average particle size of 40 nm. Carbon supported catalysts allow for fine dispersion and increased stability of catalyst nanoparticles (Auer *et al.*, 1998).

Carbon black as a platinum nanoparticle support offers various advantages including its wide availability and affordability. With specific reference to its use as a catalyst support in PEFCs, carbon black provides the required electrical conductivity for the electrons produced during the electrochemical reactions. Furthermore, carbon black is stable in the acidic conditions present in a PEFC, which is not the case for other typical support materials such as alumina or silica (Auer *et al.*, 1998). Carbon black supports also permit an economic recovery of precious metal if the carbon support is burnt off to ash. Extensive research into the fundamental differences between platinum blacks and supported platinum nanoparticles has shown that increased catalyst utilisation at reduced platinum loadings can be achieved by supported platinum catalysts (Paulus *et al.*, 2003).

University of Cape Town

2.2.2 Important shortcomings of Pt/C catalysts

A major drawback of using carbon supported platinum nanoparticles in fuel cells is that a large part of the platinum metal remains unutilised or is lost during operation. Some of the major phenomena leading to the metal loss and low metal utilisation are outlined below.

2.2.2.1 Loss of platinum active area

Platinum active area is lost through different mechanisms, the main ones being particle coarsening, Ostwald ripening and platinum migration (Zhang *et al.*, 2009). Catalyst degradation is strongly dependent on operating conditions and the nature of the support material (Meier *et al.*, 2012). Figure 2.1 below summarises the main platinum surface area loss mechanisms.

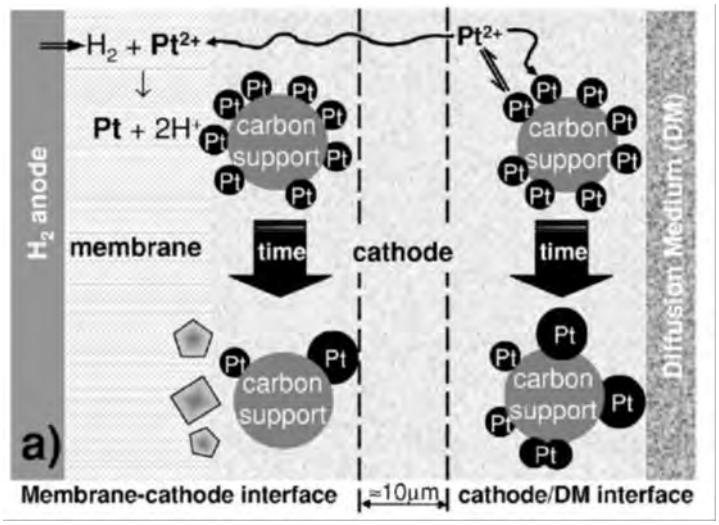

Figure 2.1 Platinuum surface area loss by (i) platinum particle growth on the carbon support and (ii) diffusion of dissolved Pt species towards the membrane and subsequent precipitation of Pt by cross-over hydrogen from the anode (Ferreira *et al.*, 2005)

Catalyst particle coarsening occurs via Ostwald particle agglomeration and particle growth. It is the principal mechanism of catalyst degradation in PEM fuel cells (Zhang *et al.*, 2009). Nanoparticles have a tendency to coalesce in order to reduce high surface energies. Ostwald ripening of nanoparticles is a mechanism by which small platinum particles dissolve in the ionomer phase and redeposit on larger platinum particles, resulting in particle growth and a reduced platinum surface area (Borup *et al.*, 2007). Ostwald ripening accounts for particle growth from 3 to 6 nm on the carbon support (Ferreira *et al.*, 2005). The second mechanism of particle growth is particle agglomeration, which occurs when platinum particles in close proximity sinter together and form a larger particle, this coalescence can be triggered by carbon support corrosion which causes catalyst particles to detach from the support itself and coalesce with other platinum particles (Borup *et al.*, 2007). Both these particle coarsening processes result in a reduced active platinum surface area and hence a reduced metal utilisation.

The third active area loss mechanism is crystallite migration. Ferreira *et al.* (2005) proposed that platinum species dissolve and travel as Pt^{2+} in the ionomer phase through the catalyst layer. Species close to the membrane/cathode interface migrate into the membrane and are chemically reduced to Pt metal by crossover hydrogen at the cathode side of the fuel cell. The reduced platinum species precipitate out in the cathode ionomer phase. These precipitated species are remote from the catalyst support and are effectively inactive.

Several groups have reported the presence of Pt metal in the polymer electrolyte membrane, providing evidence of Pt dissolution (Zhang *et al.*, 2009). Meier *et al.* (2012) investigated the degradation of Pt/Vulcan catalysts in a fuel cell under start-stop conditions. Identical location

University of Cape Town

transmission electron microscopy (IL-TEM) was used to analyse the catalyst layer before and after 3600 degradation cycles. The structural changes are apparent in the IL-TEM images and are a clear indication of the severity of the catalyst degradation that has occurred. Several different degradation mechanisms can be identified by the IL-TEM images taken and are illustrated in Figure 2.2 below.

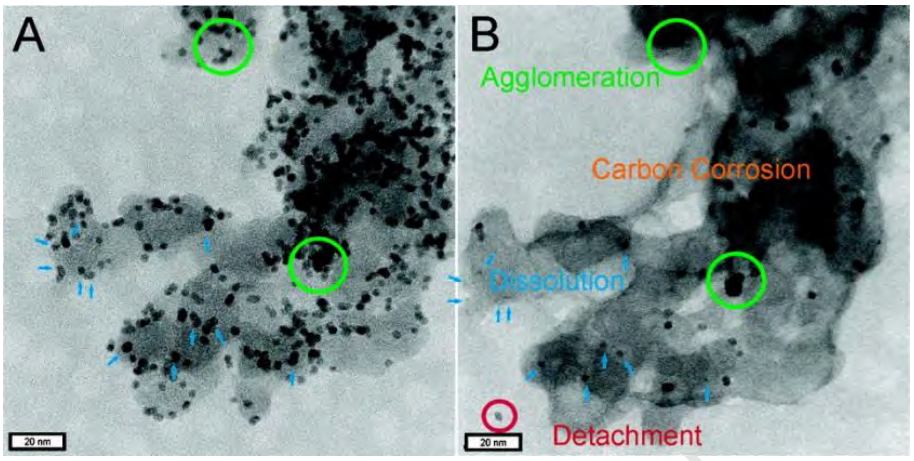

Figure 2.2 : IL-TEM images after 0 (A) and 3600 (B) degradation cycles. Green circles indicate agglomeration, red circles show detached Pt particles and blue arrows indicate dissolution of Pt particles (Meier *et al*., 2012)

The green circles indicate "particle agglomeration", as the particles increase in size before and after potential cycling. The blue arrows highlight the particles that have reduced in size due to "particle dissolution". The red circle indicates Pt particle detachment from the support and finally the orange circles illustrate the significant change in the carbon support material due to carbon support corrosion at high electrode potentials (Meier *et al.*, 2012)..

2.2.2.2 Support corrosion

Carbon support materials suffer from carbon corrosion at high potentials over time (Sharma *et al.*, 2012). This is because the oxygen reduction reaction occurs at potentials close to that of the carbon oxidation reaction (Wang *et al.*, 2009). Carbon corrodes under three conditions: (1) normal operating potentials (0.6 – 1.2 V), (2) significant fuel starvation at the anode, and (3) partial hydrogen coverage at the anode (Zhang *et al.*, 2009). As the support corrodes, platinum particles detach from the support. On the one hand the detached particles coalesce with other particles to form larger crystallites and on the other hand the Pt-support interaction is weakened. Carbon support corrosion therefore results in a reduced active catalytic surface area and reduced overall performance. Figure 2.3 below illustrates the effect of carbon corrosion on the catalyst nanoparticles and overall support morphology after 3600 degradation cycles. The catalyst used in this study was 20 wt.% loading of platinum supported on Vulcan XC72 support.

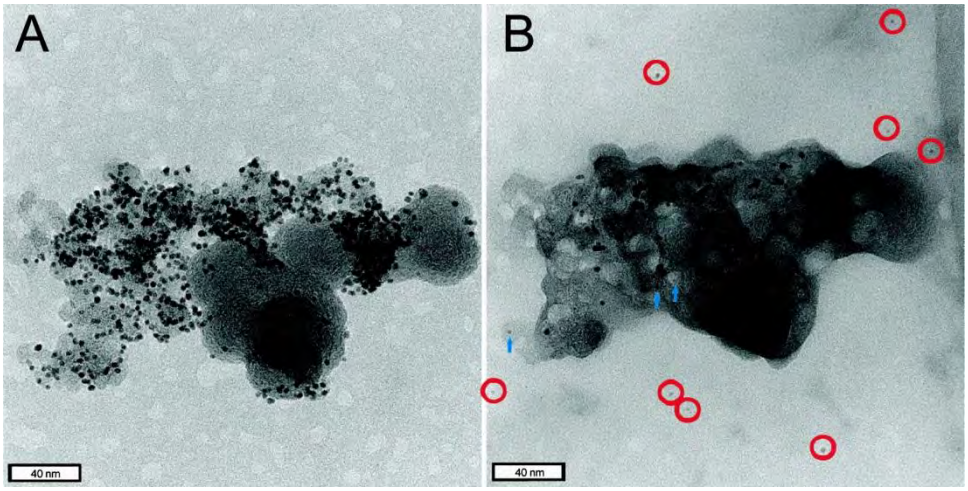

Figure 2.3 : TEM images of catalyst particle location after 0 (A) and 3600 (B) degradation cycles. The red circles indicate catalyst particle detachment form the support. The blue arrows indicate platinum particles that have decreased in size due to dissolution (Meier *et al.*, 2012)

Severe carbon corrosion was observed after 3600 degradation cycles, which lead to significant changes in the support morphology and to catalyst particles detaching from the support (red circles) Catalyst particle agglomeration was also observed as the average size of the Pt particles increase after 3600 cycles. The support material contributes significantly to the overall catalyst degradation, and as such the importance of studying the properties and effects of the support material used in the catalyst synthesis is paramount (Meier *et al.*, 2012).

2.2.2.3 Need for ionomer in the catalyst layer

Platinum supported on carbon catalysts require an ionomer phase within the catalyst layer to facilitate proton transfer from the active sites to the polymer electrolyte membrane. An ionomer phase is required to conduct protons, as carbon is a non-proton conducting material. The most commonly used proton conducting ionomer is a perflourocarbon copolymer called Nafion® (barber, 2005).

Three different species take part in the electrochemical reaction, namely gases, protons and electrons. All three species must have access to the catalyst surface. Electrons are able to travel over electrically conductive solids such as the carbon support and the platinum catalyst itself. Protons are only conducted by the ionomer phase, and the reactant gases travel through the voids in the porous gas diffusion electrodes. The electrodes must be porous to allow reactant gas access to the catalyst layer and to allow product water to be effectively removed to avoid flooding which would prevent oxygen access (Barbir, 2005). In order for an electrochemical reaction to occur at a catalytic active site, there must be simultaneous contact between the solid catalyst site, the ionomer phase and the reactant gas, this is known as the three-phase boundary. The diagram below illustrates the

University of Cape Town

three-phase boundary condition necessary for an electrochemical reaction to occur at a metal active site, Figure 2.4.

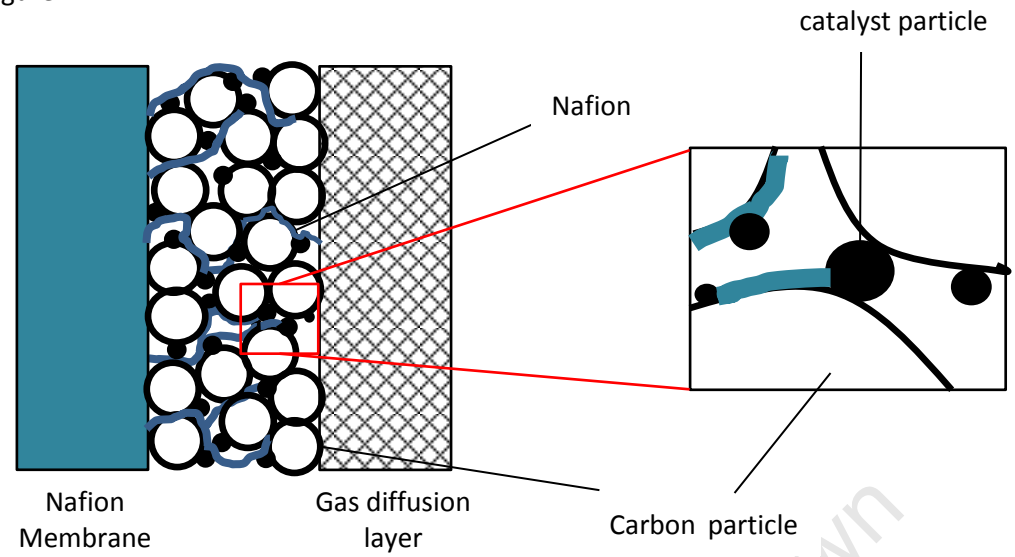

Figure 2.4 : Figure 2.4 : The three phase boundary formed by the catalyst particles, the ionomer and the gas phase ensuring electronic and ionic contact as well as gas transport through the porous structure (Zainoodin *et al.*, 2010).

On Pt/C supported catalysts, the three-phase boundary condition must be met in order for an electrochemical reaction to occur. Realistically however, it is not feasible for every catalytic active site to meet this condition and as such a metal utilisation of 100% is very unlikely.

2.3 The active surface for the Oxygen Reduction Reaction (ORR)

2.3.1 The oxygen reduction reaction (ORR) mechanism

The oxygen reduction reaction (ORR) occurring on the cathode side of a fuel cell (equation 2.1) is one of the most extensively researched electrochemical reactions owing to its significance in fuel cell operation.

$$\tfrac{1}{2}\, O_2 + 2\, H^+ + 2\, e^- \rightarrow H_2O \qquad (2.1)$$

Platinum is the most common and active electrocatalyst used for the ORR as Pt has a high activity towards the ORR and a high stability under cathode operating conditions. Much attention has been paid to this reaction, as the sluggish kinetics of the ORR due to high reaction over potentials (0.3-0.4V), lead to the need for high catalysts loadings of 0.1 - 0.5 mg/cm^2 on the cathode side of the fuel cell in order to attain reasonable performance (0.2 g/kW) (Rabis *et al.*, 2012). This inherently increases the cost of production of PEFCs and is the main deterrent preventing fuel cells from bulk commercialisation (Sheng *et al.*, 2012).

University of Cape Town

The oxygen reduction reaction in both acidic and alkaline electrolytes is ideally a four electron process, whereby O_2 is directly reduced to H_2O. The actual mechanism is still poorly understood, however, initial studies using the rotating ring disk electrode (RRDE) technique have suggested that the ORR proceeds via a hydrogen peroxide intermediate, although sound experimental evidence is lacking in this area to date (Rabis *et al*., 2012). Several multi-reaction pathways have been suggested in the literature; however the simplified ORR mechanism presented by Wroblowa *et al.* (1976) is the most commonly used. According to this reaction pathway, oxygen species adsorbed on the Pt surface may be reduced via two alternative pathways:

(i) The "direct" or "4 electron" pathway, where water is formed as the main product of the reaction with no detectable intermediate species formed.

$$O_2 + 4e^- + 4H^+ \Leftrightarrow 2H_2O \tag{2.2}$$

(i) The "series" or "2 electron" pathway, where a hydrogen peroxide intermediate is formed.

$$O_2 + 2e^- + 2H^+ \Leftrightarrow H_2O_2 \tag{2.3}$$

(ii) The hydrogen peroxide can be further reduced to water.

$$H_2O_2 + 2e^- + 2H^+ \Leftrightarrow 2H_2O \tag{2.4}$$

The "direct" and "series" pathways can be distinguished by determining whether or not the hydrogen peroxide intermediate species is formed, this is done by rotating ring disk electrode (RRDE) measurements. It was found in a recent study by Katsounaros *et al*. (2012), that the "direct" ORR pathway dominated at potentials above 0.3 V vs. RHE. And the "series" pathway dominated below 0.3 V vs. RHE (Katsounaros *et al.*, 2012). This is a significant finding as it is important to understand the ORR reaction mechanism under all conditions in order to maximise the efficiency of the ORR.

2.3.2 **The platinum surface: from bulk polycrystalline to nanoparticles**

The difference between a bulk, crystalline platinum surface and platinum nanoparticle must be established in order to better understand the effects of particle size on the ORR activity. A polycrystalline platinum surface is characterised by a face-centred cubic structural packing of atoms.

University of Cape Town

A continuous metal surface is observed for the bulk metal. Platinum nanoparticles however, are characterised by discrete particles in the nano-size range, theoretically the ideal geometric structure representative of a small Pt nanoparticle is assumed to be that of a cubo-octahedron consisting of Pt atoms arranged on eight (111) and six (100) crystal faces connected by edge and corner atoms (Kinoshita, 1990). As the particle size changes the concentration of various crystal faces changes. This is the theory behind the relationship between particle size and ORR activity and has been used to create model simulations of the particle size effect based on single crystal data. A model Pt nanoparticle based on a cubo-octahedral structure is shown below in Figure 2.5.

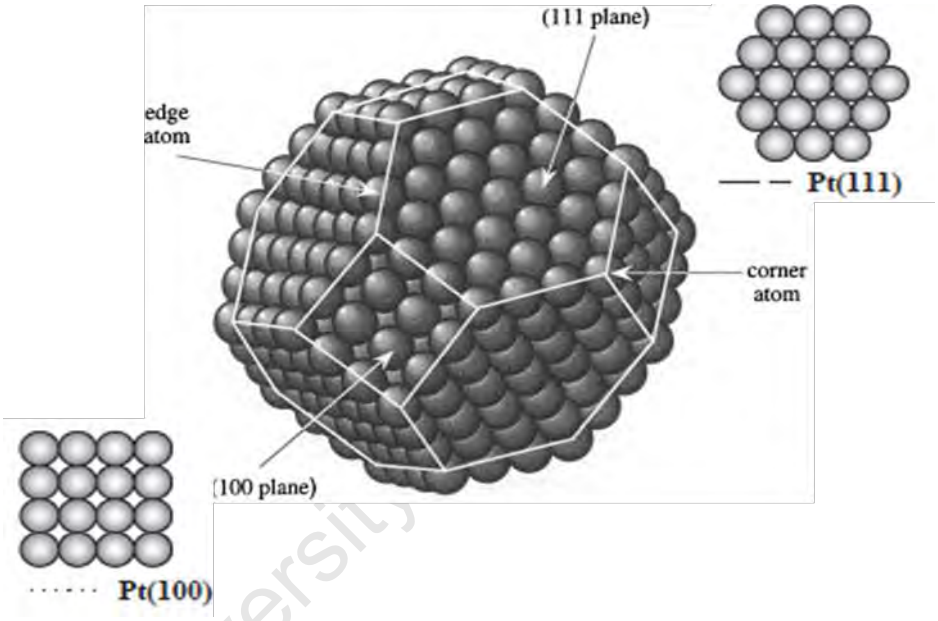

Figure 2.5 : model cubo-octahedral structure of a platinum particle illustrating (111) and (100) crystal faces and edge and corner atoms (Kinoshita, 1990).

2.3.3 The platinum active surface: insights through single crystal studies

Many studies have investigated single Pt crystal properties and the contribution of different crystal planes to the overall activity of Pt, in particular the activity of Pt in the oxygen reduction reaction (ORR) (Climent and Feliu, 2011). Another large research focus is the change in surface area and activity when comparing bulk polycrystalline Pt surfaces, Pt black type surfaces (up to 10 nm) and Pt nanoparticles (10 nm and smaller) (Sheng *et al.*, 2011). In reality however, supported catalysts contain a wide distribution of particle sizes, thus making it difficult to experimentally determine the particle size effect on the ORR activity (Kinoshita, 1990). Nesselberger *et al*. (2011), found that the specific activity of the ORR decreased rapidly from polycrystalline Pt > unsupported Pt-black particles (~30nm) > high surface area (HSA) supported platinum nanoparticles (1 -5 nm). He found that

simple models based on single crystal data were insufficient to capture the behaviour of high surface area carbon catalysts. A more comprehensive model is required that incorporates the carbon support effect and the fact that the effective reaction pathway of the ORR changes with particle size (Nesselberger *et al.*, 2011).

It is difficult to predict the structure of a small supported catalyst particle based on geometry and number of surface atoms because in reality perfect crystal faces do not form. A study conducted by Mukerjee (1989) (Mukerjee, 1989) (Mukerjee, 1989) (Mukerjee, 1989) (Mukerjee, 1989) (Mukerjee, 1989) (Mukerjee, 1989) (Mukerjee, 1989) (Mukerjee, 1989) (Mukerjee, 1989) (Mukerjee, 1989) (Mukerjee, 1989) (Mukerjee, 1989) (Mukerjee, 1989) (Mukerjee, 1989) (Mukerjee, 1989) (Mukerjee, 1989) confirmed the existence of three of these crystal faces in dispersed Pt supported catalysts. Findings by Stonehart *et al*. (1976) contradict the theory that crystal face type influences the ORR kinetics. Contradicting results between single crystal studies and supported platinum nanoparticles indicates that single crystal models do not accurately describe dispersed nanoparticle behaviour and further investigations are necessary.

Potential sweep methods were used in single crystal studies on Pt to examine the adsorption peaks which appeared for the main crystal planes (111), (100) and (110). Three peaks were observed and assigned to the respective crystal faces (Mukerjee, 1989). Following this study, Kinoshita and Stonehart (1976), investigated the hydrogen adsorption and desorption peaks associated with supported Pt catalysts in 1M H_2SO_4 and found an interesting correlation between particle size and the peaks observed in the anodic, hydrogen desorption region. The two peaks observed in the cathodic, hydrogen adsorption region remained unchanged with particle size. However, in the anodic region, a third anodic peak was observed and became more distinct as particle size decreased. Stonehart *et al.* (1976) concluded that the more weakly bonded hydrogen species corresponded to the (111) crystal face while the more strongly bonded hydrogen species, which occurs at a higer overpotential corresponds to the (100) crystal face. The third anodic peak observed at small particle sizes was attributed to adsorbed hydrogen on the edge and corner atoms of the particle. This observation was explained using the cubo-octahedral geometric model, where a decrease in particle size results in an increase in the relative amount of edge and corner atoms as they become more significant relative to the total number of atoms as particle size decreases. Therefore the third anodic peak which occurs at a potential between the (111) and (100) crystal faces is seen predominantly at small particle sizes and accounts for 14% of the adsorbed hydrogen species (Mukerjee, 1989). These findings were ground breaking as they definitively determined the existence of the three crystal faces in dispersed Pt catalysts.

University of Cape Town

2.3.4 **The platinum particle size effect on ORR activity**

Over the past few decades different research groups have tried to gain a better insight and understanding of the electrochemical behaviour of platinum catalysts with respect to the oxygen reduction reaction. In order to use platinum economically, platinum is supported on carbon blacks and other supports. This raises the question of the effect of platinum crystallite size on the kinetics of the oxygen reduction reaction, the widely researched "particle size effect" (Yang, 2013). It has been widely reported by many authors that there still currently exists a discrepancy between the effect of particle size on the specific activity of the platinum catalyst (Mayrhofer *et al*., (2007);Xu et al., (2012)) Furthermore with decreasing particle size the stability of Pt nanoparticles declines and results in a shorter lifespan (Sheng *et al*., 2012). Therefore the importance of determining the particle size effects of Pt nanoparticles on activity and stability is necessary in order to attain a Pt-based catalyst with an appropriate particle size for use in PEM fuel cell applications.

2.3.4.1 Early studies

A landmark paper regarding the particle size effect was published by Kinoshita in the 1990's where he summarised the main findings on the topic for the time. The paper lists the major contradictory trends observed in the literature, and attempts to rationalise the findings based on the assumptions that a Pt particle can be modelled as a cubo-octahedron and the surface structure plays a significant role in the oxygen reduction kinetics (Kinoshita, 1990). In reality it is difficult to model a small catalyst particle by a well-defined geometric structure, as it is unlikely that the particle will contain the exact number of atoms necessary to form the respective crystal faces (Mukerjee, 1989). Hence to simplify matters, a more realistic model of a platinum particle is based on the assumptions that (i) the shape of the platinum particle is such that surface energy is at a minimum and (ii) atoms in excess of that required for the model are located on existing crystal faces (Mukerjee, 1989).

The main contradictory trends observed in the literature at this time were as follows; (i) a maximum in mass activity is observed at particle sizes between 3-5 nm; (ii) mass activity increases with particle size; (iii) specific activity decreases as particle size decreases; (iv) specific activity is independent of Pt particle size (Kinoshita, 1990). These different observations of the particle size effect will be discussed in detail below, it must be taken in to account that a wide range of experimental preparative procedures and conditions have been used for catalyst synthesis in the literature throughout, and hence comparisons of different findings could be influenced by this fact (Mukerjee, 1989).

University of Cape Town

(i) Maximum mass activity observed

At the time of this paper there was no evidence that the oxygen reduction reaction occurred preferentially on any particular crystal-face site on a supported platinum catalyst (Kinoshita, 1990). Ross and Sattler (1986) concluded that there was no difference in the rate of the oxygen reduction reaction on (111) and (100) sites on well oriented platinum surfaces. However, from a study on Pt supported catalysts, Ross *et al*. (1986) concluded that the (100) crystal face is the most active site for oxygen reduction. The discrepancy between the rate of the oxygen reduction reaction on single crystal Pt surfaces versus the corresponding crystal faces in supported platinum particles, indicates that single crystal studies do not accurately predict the oxygen reduction behaviour on small supported Pt nanoparticles.

Van Hardeveld and Hartog (1972)predicted the relationship between platinum particle size and the number of atoms associated with the (111), (100) and edge and corner (e + c) sites in a model cubo-octahedral platinum particle, and plotted the relationship of the mass averaged distribution (MAD) of atoms associated with the (111), (100) and (e + c) sites versus particle size see Figure 2.6 below (Kinoshita, 1990).

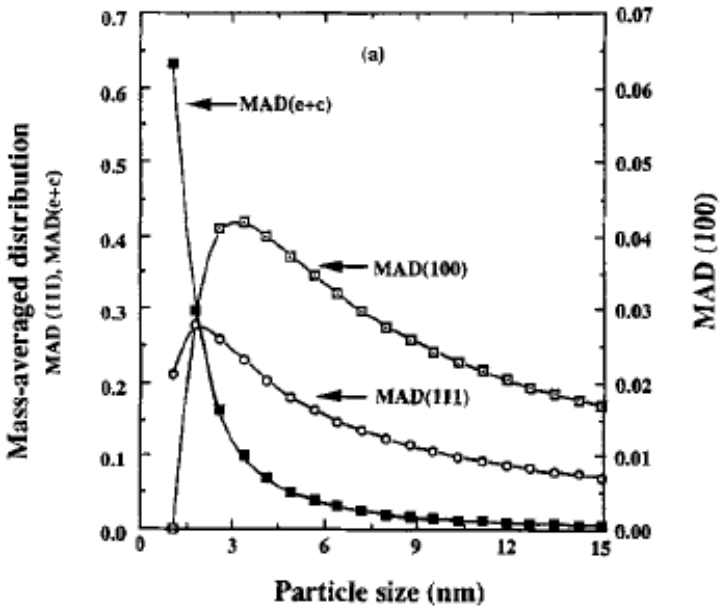

Figure 2.6 MAD of (111), (100) and edge and corner sites of a model cubo-octahedral particle versus particle size (Kinoshita, 1990)

Using this relationship a maximum in the mass average distribution (MAD) of the (111) and (100) crystal faces was observed at diameters of 2 nm and 3.5 nm respectively. Ross *et al*. (1986) postulated that the (100) crystal face is the active site for the oxygen reduction reaction (Ross and Sattle., 1986). Following this model observation, it could be expected that the mass activity would

show a maximum at the same particle sizes assuming that the (100) face is the active site for the oxygen reduction reaction. Peuckert *et al*. (1986) observed a maximum in mass activity (MA) at an average particle size between 3.5 and 5.5 nm, however some debate still remains to the reliability of the prediction of the (100) face being the sole active site for ORR, as the (111) face showed a maximum in MAD at 2 nm, and taking into account the fact that highly dispersed supported Pt catalysts generally have a distribution of particle sizes, and hence the (111) face should also be considered as an active site for ORR (Kinoshita, 1990). Ross *and Sattler* (1986) also observed a maximum in mass activity at 3.5 nm and concluded that the (100) crystal face was more active than the (111) and (110) crystal faces (Ross *et al.*, 1986).

In a study by Peuckert *et al.* (1986)*,* catalyst samples with a range of particle sizes from 1 to 4 nm and a 12 nm Pt black sample were prepared. The crystallite sizes were determined by chemisorption of H_2 and the catalyst samples were characterised by dihydrogen adsorption and dihydrogen titration of adsorbed oxygen in 0.5M H_2SO_4 at 298K (Peuckert *et al.,* 1986). The activity measurements showed a decrease in activity for particles less than 1 nm in size, this observed decrease in activity was attributed to the increase in metal dispersion and the corresponding increase in the number of surface Pt atoms able to participate in the ORR reaction as particle size decreases. However the overall activity per surface Pt atom decreases with decreasing particle size, and these two counteracting effects result in a maximum in mass activity at particle sizes between 3–5 nm (Peuckert *et al.*, 1986).

(ii) No particle size effect observed below 5 nm sized particles

Watanabe *et al*. (1988) studied the effects of platinum crystallite dispersion on the methanol oxidation reaction in sulphuric acid, it was concluded that mass activity increased proportionally as particle size decreased, a maximum mass activity was not observed at particle sizes between 3-5 nm ((Watanabe *et al.*, 1986).and Bett *et al*. (1973), drew a similar conclusion and did not observe a maximum mass activity at any particle size, however this could be owed to the fact that the particle size range investigated did not span the range where maxima in MAD (100) and MAD (111) could be observed (Kinoshita, 1990).

Recent studies on the particle size effect

The introduction of thin film RDE in 1998 allowed for a high level of reproducibility and hence accurate comparison between the performance of different supported Pt catalysts. This novel characterisation technique changed the way the particle size effect was viewed compared to the dated characterisation techniques used in the eighties.

University of Cape Town

It has been found that variations in catalytic activity can be attributed to changes in surface electronic structure and geometric structure which are directly related to particle size (Mayrhofer *et al.*, 2005). In a recent study by Shao *et al*. (2011) , the particle size effect was invesitgated in $HClO_4$ solution on Pt particles in the range of 1-5 nm in size. Pt particle size was controlled by layer by layer growth with Pt seed particles 1.3 nm in size supported on Ketjen black (specially synthesized by Tanaka Kikinzoku Kogyo, 10 Wt%) (Shao *et al.*, 2011). As in the model study by Kinoshita (1990), a maximum in mass activity was observed by Shao *et al.*(2011) in this case for particles of 2.2 nm in size. The particle size dependent ORR activity was shown in this study to be related to the oxygen binding energies on the different Pt sites on a cubo-octahedral Pt nanoparticle. Surface reactivity of the catalyst surface correlates with its catalytic activity. However, for the ORR, a high surface activity enhances adsorption of reaction intermediate molecules, which effectively block the active sites for the oxygen reduction reaction. Hence by calculating the oxygen binding energies, assuming a cubo-octahedral shaped particle, the surface reactivity of the different sites can be evaluated and the dependence of reactivity on particle size can be determined in this way. The reactivity of a surface atom is directly related to the particle size and co-ordination number. Oxygen binding energies for particles of the size 0.8- 3 nm, were averaged for all surface sites and plotted as a function of particle size, see Figure 2.7.

University of Cape Town

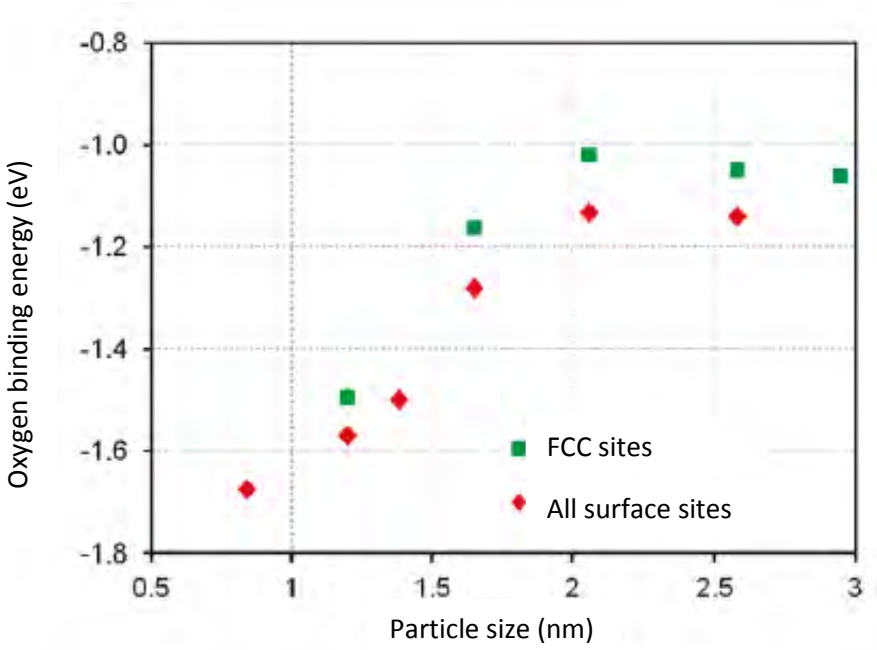

Figure 2.7 : Averaged oxygen binding energies for all surface sites and fcc sites as a function of particle size (Shao *et al.*, 2011)

The oxygen binding energy of Pt-O, for all surface sites is seen to decrease with particle size to a minimum particle size of approximately 2.2 nm. Due to the high oxygen binding energy contributions of the edge and corner sites, the oxygen binding energies for all averaged surface sites is higher than for the fcc sites. The strong Pt-O bond for small particles is related to the electronic structure of the atoms and is also reflected in the shift to lower overpotentials of the Pt-O reduction peak in the cyclic voltammograms plotted for each particle size. This shift in Pt-O reduction to more negative potentials, supports the evidence presented by the oxygen binding energy data, that smaller nanoparticles are more oxophilic and hence spectator species bind more strongly to the active sites blocking them for the ORR.

A maximum in mass activity was observed at a particle size of 2.2 nm, see Figure 2.8 which corresponds to the particle size with the lowest oxygen binding energy.

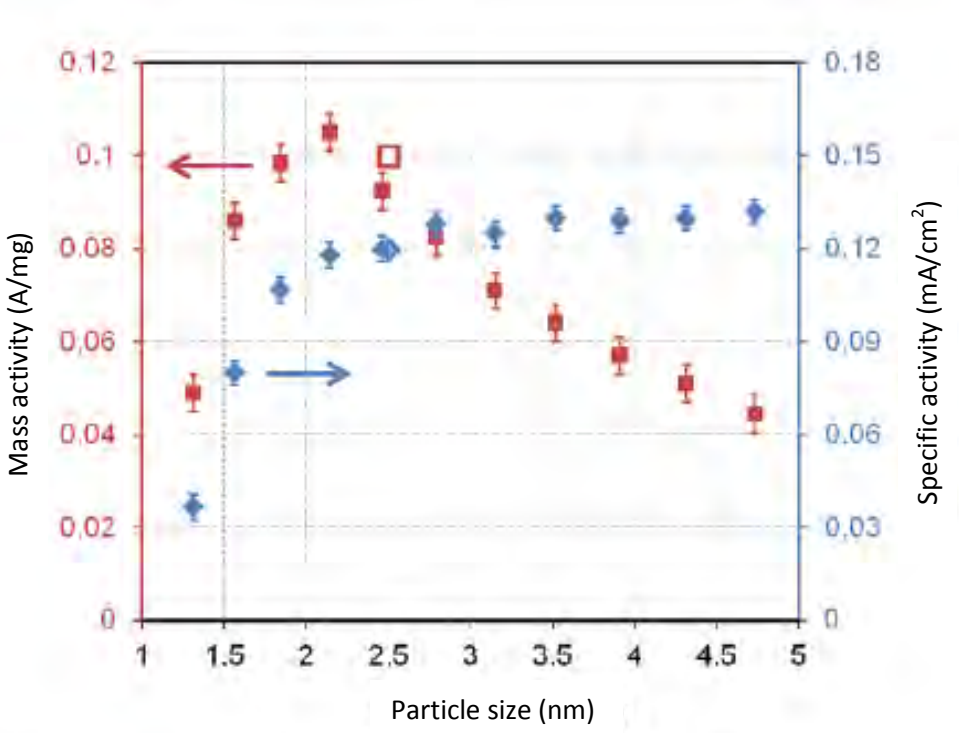

Figure 2.8 : Size dependence of specific activity and mass activity measured at 0.93 V for the oxygen reduction reaction on Pt/C. The mass and specific activities were calculated by normalising the kinetic current to the mass of Pt on the electrode surface and the electrochemically active surface area, respectively (Shao *et al*, 2011).

From the graph above its is apparent that the specific activity increases sharply from 1.3 to 2.2 nm and then more slowly from 2.2 nm onwards. The low specific activity was attributed to the edge sites which were found to have high associated oxygen binding energies, thus inhibiting ORR by adsorption of oxygen spectator species. This study placed an emphasis on the importance of the different types of surface sites and edge and corner sites on the mass and specific activities of the oxygen reduction reaction. Specific emphasis was placed on small particles in the range of 1 to 5 nm, where a clear maximum in mass activity was observed at a particle size of 2.2 nm (Shao *et al.*, 2011).

In the work by Schwanitz *et al.* (2012), the morphological effects of sputtered model electrodes with various Pt loadings of 5 to 500 µg/cm^2 were studied and compared to commercial ink based catalysts and the state of the art NSTF catalyst by 3M. The increase in platinum loading sputtererd on the electrode surface incurred an increase in the average Pt particle size, from isolated Pt nanoparticles (2-3 nm) for loadings <20 µg/cm^2, to Pt agglomerates at intermediate loadings, and extended surfaces observed at loadings above 20 µg/cm^2.

Schwanitz *et al*. (2012) observed a change in specific activity as the Pt loading increased, and attributed this observation to the well-known particle size effect. It was concluded that the differing

platinum particle sizes associated with the different loadings sputtered on the electrodes accounted for the varying kinetics of the oxygen reduction reaction. Where low loadings correspond to isolated nanoparticles and high loadings to agglomerates and extended surfaces, as previously mentioned. The change in specific activity was explained by the changing OH adsorption properties of the catalyst surface with changing Pt loading, hence particle size. The adsorption potential of OH spectator species for the low loading sputtered electrodes (2-3 nm particles), occurred at more negative values relative to the high loading, extended surface type surface electrodes. This effect is attributed to the strong adsorption of OH spectator species to small Pt nanoparticles, thus inhibiting the ORR and reducing the specific activity. An increase in specific activity was observed as Pt loading and hence particle size increased, see Figure 2.9 (a) below. The mass activity was found to decrease as Pt loading increased, see Figure 2.9 (b) below.

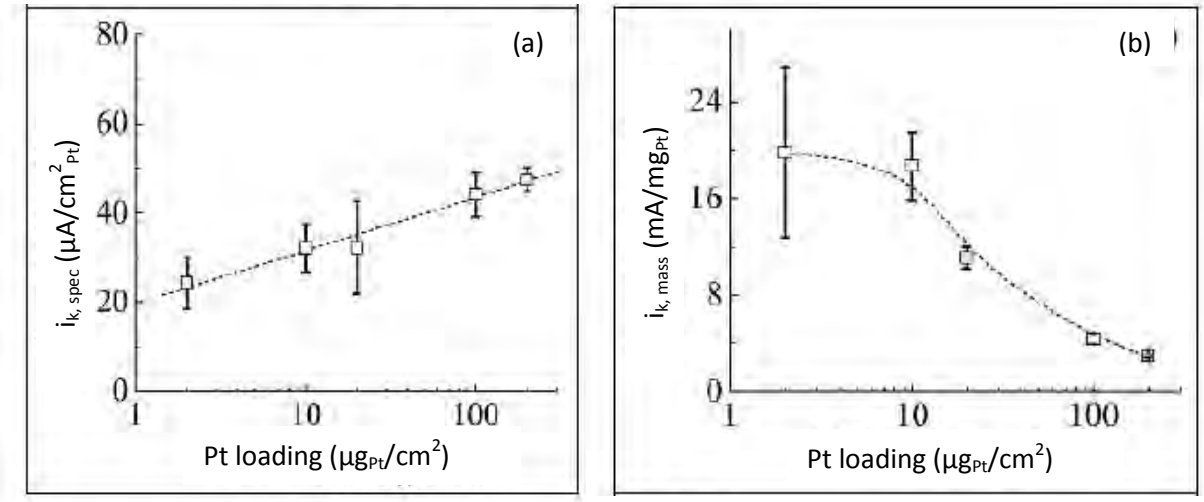

Figure 2.9 : Comparison of oxygen reduction reaction (a) specific activity and (b) mass activity of sputtered Pt on vulcan modelelectrodes with different Pt loadings at ambient temperature and pressure, current densities are at constant electrode potential of 0.90 V (RHE) (Schwanitz *et al.,* 2012).

Normalising the specific and mass activities of this study by the activities at an arbitrary specific surface area, in this case 20 m^2/g, the results from this study were plotted on a master curve illustrated below in Figure 2.10.

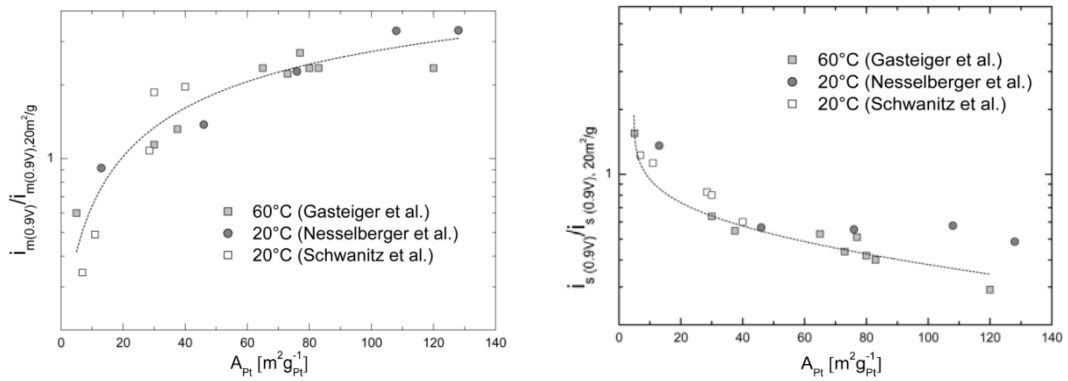

Figure 2.10 : Normalised specific ($i_{s(0.9\ V)}$) and mass ($i_{m(0.9\ V)}$) activity toward the ORR on different Pt catalysts. Data extracted from RDE measurements by Gasteiger et al. (60 °C, 0.9 V, 5 mV/s, data taken from anodic sweeps, 1600 rpm, 0.1 M HClO4, Pt/C, Pt-black, and Pt-poly), Schwanitz et al. (20 °C, 0.9 V, 5 mV/s, 1600 rpm, data taken from cathodic sweeps, 0.1 M HClO4, sputtered Pt particles and layers), and Nesselberger et al. (20 °C, 0.9 V, 1600 rpm, anodic sweeps, base CV- corrected, Pt/C catalysts, Pt-black) (Rabist *et al*., 2012).

The study by Schwanitz *et al*. (2012) concluded that specific activity increases as particle size increases and mass activity decreases with particle size. This is in contradiction to the study by Shao *et al*. (2011), which reports a maximum in mass activity at 2.2 nm. The opposing findings still reported to date in recent studies, highlight the fact that the Pt particle size effect on the ORR is an elusive topic which still requires further investigation and understanding before any solid conclusions can be drawn.

2.3.5 The influence of -OH surface coverage and hydrogen peroxide formation on the ORR activity

In the late 1980's, Mukerjee (1989) suggested that possible changes in surface electronic conductivity with Pt particle size should be investigated as these changes could affect charge transfer to the catalyst surface. The development of new technology over the years has allowed us to investigate the particle size effect with techniques such as electrochemical impedance spectroscopy (EIS) and observe the particle size effect from a different angle.

It was proposed by Mayrhofer *et al.* (2008) that the oxophilicity of Pt nanoparticles increases as particle size decreases. This means that for the same potential, the surface coverage of OH groups is greater for smaller particles. These OH groups effectively block the active sites required for oxygen adsorption and hence lead to a decrease in specific activity. This effect was also observed by Peuckert *et al*. (1986) and more recently by Yang *et al*. (2013), where a shift in the oxygen reduction peak to more negative potentials occurs as particle size decreases. This finding was explained by the higher affinity of smaller particles towards oxygen species i.e. oxygen species form a stronger bond to the platinum surface of small Pt particles. The adsorption of OH itself is particle size dependent

University of Cape Town

and directly affects the ORR activity and it is therefore important to determine at what particle sizes adsorption of OH groups is significant (Yang *et al.*, 2013) Kinoshita's (1990) cubo-octahedral model particle can also be used to explain the increased affinity of OH groups for smaller Pt nanoparticles. At smaller particle sizes edge and corner atoms become more significant with reference to the overall number of surface atoms, and OH bonds more strongly to these sites and as such smaller particle sizes incur a stronger OH adsorption. In a study by Peuckert *et al*. (1986) a series of catalysts were prepared by wet chemical methods by impregnation with H_2PtCl_6 and various Pt loadings and particle sizes as follows, 5, 10, 20 and 30 weight % Pt on carbon and average crystallite sizes of: 1, 1.1, 1.4 and 4.1 nm. A Pt-black electrocatalyst with a particle size of 12 nm was also prepared. The oxygen reduction peaks associated with each Pt loading are plotted in the Figure 2.11 below.

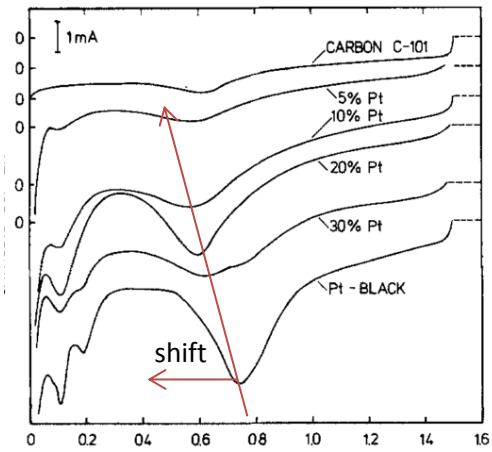

Figure 2.11 : Cathodic branches of cyclic voltammograms of nitrogen-purged carbon support material and Pt/C catalysts (scan rate: 100 mV/s in 0.5 M H_2SO_4) (Peukert *et al.*, 1986).

This figure clearly shows the shifting oxygen reduction peak to more negative potentials from Pt-black to the 10 weight % Pt catalyst with small particles having the lowest oxygen reduction peak potential. As the platinum content further decrease to 5 weight %, the peak potential shifts more positively. This is an indication of a maximum particle size for which the oxygen reduction peak potential is the lowest. As in previous studies, Peuckert *et al.* (1986) indicate a maximum in mass activity at particle size between 3 and 5 nm, and this corresponds to the particle size associated with the lowest oxygen reduction potential in the cathodic scan of the CV in Figure 2.11. The effect of shifting oxygen reduction peak potentials with decreasing particle size is still seen today and therefore supports the findings of Peuckert *et al.* (1986) even today.

Another factor that supposedly has an effect on the ORR activity is the inter-particle distance. Inter particle distance is thought to play an important role on the mass transport rate of reactant and product species and the effects of interparticle distance on the ORR have been observed by Watanabe *et al*. (1986) and more recently confirmed by Yang *et al.* (2013). Yang *et al.* (2013)

investigated the extent of peroxide formation and the ORR activity in relation to particle size and inter-particle distance using the rotating ring disk electrode (RRDE). Yang *et al.* (2013) highlighted the significance of the second reaction pathway available for the ORR which produces H_2O_2, this reaction has often been neglected and assumed negligible, it is a 2 electron process and as such the overall efficiency of the ORR reaction is reduced if H_2O_2 forms as the final product of reaction. Hydrogen peroxide formation is accelerated at higher mass transfer rates therefore if interparticle distance does in fact affect the mass transport of reactant and product species, it could also play a role in the rate of H_2O_2 formation (Yang *et al*., 2013).

Chen and Kucernak (2004) concluded that the amount of hydrogen peroxide formation is higher on smaller particles than on larger particles, owing to the higher mass transport rate on smaller particles. The H_2O_2 molecules formed diffuse away from the active site so rapidly that they are not further reduced to H_2O. Yang *et al.* (2013) studied this effect using RRDE, whereby the disk was scanned from 0.18 V to positive potentials, while the ring was held at a constant potential of 1.28 V vs. RHE i.e. the potential at which H_2O_2 is reduced to H_2O. The onset of H_2O_2 formation was observed at potentials below 0.8 V where it became more significant at lower potentials. It was found that peroxide formation increased as particle size decreased from 7.3 nm to 2.2 nm (Yang *et al.*, 2013). Studies on bulk platinum showed that the presence of OH and adsorbed anions promotes the formation of H_2O_2 (Kinoshita, 1990). This relates directly to this study's findings, whereby at smaller particle sizes OH adsorption is stronger and hence H_2O_2 formation increases.

It was concluded that both particle size and inter-particle distance play a crucial role in the ORR kinetics and H_2O_2 formation which directly affects ORR activity. The indirect reaction pathway for the formation of H_2O via H_2O_2 should not be ignored (Yang *et al.*, 2013).

In a recent study by Xu *et al*. (2012), platinum supported on carbon catalysts were prepared by electrochemical aging processes, with a range of mean particle sizes from 2.9 to 6.5 nm. Xu *et al*. (2012) observed a maximum in mass activity between particle sizes of 3.5-4.5 nm. Specific activity was found to increase with particle size increase, and this was attributed to the fact that larger particles have a lower affinity for surface blocking OH groups and hence more active sites are available on the surface of larger catalyst particles for ORR to occur. The findings by Xu *et al.* (2012) corresponded to early findings by Kinoshita in 1989. Xu *et al*. (2012) adopted the same cubo-octahedral model introduced by Kinoshita (1990), to explain the particle size trends observed, and attributed the changes in ORR activity to the changes in particle surface properties related to the changing particle size. It was proposed that surface "defects" or edge and corner atoms are

University of Cape Town

responsible for the strong OH adsorption, these defects are more pronounced at smaller particle sizes as seen in the Figure 2.12 below.

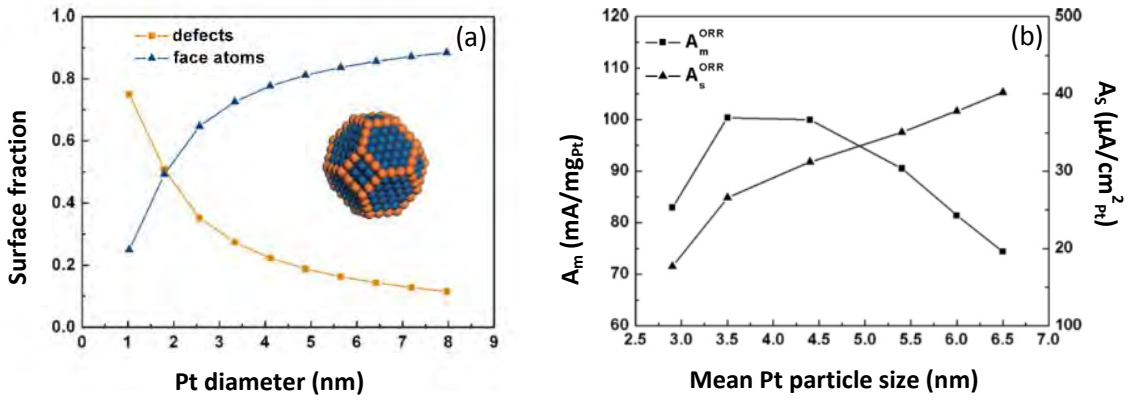

Figure 2.12 : (a) Surface simulation for cubo-octahedral platinum nanoparticles with different particle diameters. (b) Mass specific and surface area specific activities for Pt/C electrocatalysts with various mean particle sizes (Xu *et al.*, 2012)

Figure 2.12 illustrates the relationship between the relative amount of surface and defect atoms with particle size. Based on the theory of stronger OH adsorption on defect atoms, this model accounts for the proposed decrease in ORR activity for small particle sizes, as surface defect atoms are more abundant at smaller particle sizes, below 3 nm (Xu *et al.*, 2012)

Nesselberger *et al*. (2011) examined the effect of particle size on the ORR in three different electrolytes, two acidic electrolytes ($HClO_4$ and H_2SO_4) and an alkaline electrolyte (KOH). It was found that the supporting electrolyte affected the ORR rate but the actual ORR activity and particle size was unaffected by the type of electrolyte used. The absolute reaction rate decreased in the order $HClO_4$ > KOH > H_2SO_4. Using single crystal surfaces in the respective electrolyte solutions, it was found that in $HClO_4$ the Pt (111) crystal face was more active than the Pt (100) face, however in H_2SO_4 Pt (111) was found to be the least active crystal face, this was attributed to the strong adsorption of SO_4 spectator species to the Pt (111) crystal face, thus inhibiting the ORR reaction.

A similar study investigating the particle size effect on platinum nanoparticles between 1 and 5 nm was carried out by Watanabe *et al*., (2006). However, in contradiction to the findings by Xu *et al*. (2012), Watanabe (2006) proposed that due to comparable surface electronic structures of platinum nanoparticles less than 5 nm in size, the oxygen reduction reaction in 0.1 M $HClO_4$ solution is rendered size-independent (Watanabe *et al.*, 2012). A recent study by Sheng *et al.* (2012) came to the same conclusion with regards to a size-independent ORR for particles less than 5 nm in diameter.

2.4 Models evaluating continuous Pt surfaces vs. Pt nanoparticles

Using different approaches, studies by McBreen (1985)and Paulus *et al.* (2003) developed model electrodes to gain a better understanding of the difference between continuous platinum surfaces (i.e. platinum black type catalysts) and discontinuous platinum surfaces (i.e. carbon supported platinum type materials).

McBreen (1985) reinforced the idea of the three-dimensional reaction zone and the non-protonic conduction of carbon surfaces. McBreen (1985) performed experiments involving combinations of multiple platinum screens one on top of the other and the interposition of graphite felt or gold screen between the platinum and the membrane. It is known that hydrogen neither adsorbs nor is mobile on either of these materials. It was found that when two platinum screens were used one on top of the other with only one screen in contact with the membrane, adsorption charges on the platinum doubled. This indicated that parts of the catalyst layer, remote from the membrane are electrochemically active. This suggested that hydrogen can dissociate anywhere on the catalyst layer and protons can migrate to the membrane. When a graphite layer was placed between the membrane and the platinum catalyst layer, a considerable decrease in surface activity occurred. The migration process of the dissociated hydrogen ions (protons) is of particular interest. Possible mechanisms of current generation at sites remote from the membrane were explored by McBreen (1985). The first possible mechanism occurring at platinum surfaces in direct contact with the membrane is that in the presence of water, oxygen can interact with platinum to form adsorbed hydroxyl species with fast mobility. Adsorbed hydrogen and hydroxyl groups with fast mobility could be responsible for the transfer of protons from the active sites to the membrane. Considering the graphite/platinum experiment, the small amount of activity could be attributed to a 'resistive surface conductance pathway', Nafion® immersed in water produces surface protons which provide a conductive pathway along the surface of the gold/graphite and transmit current to the platinum (McBreen, 1985).

McBreen's (1985) main finding was that platinum particles remote from the polymeric membrane are electrochemically active. He also found that protons are able to migrate from the metal surface to the membrane in the presence of a continuous platinum surface. However, when the continuous platinum surface is disrupted by a non-conductive carbon layer, proton conduction does not occur or occurs at a minimal level.

University of Cape Town

Paulus *et al.* (2003) furthered the studies by McBreen (1985) by developing model gas diffusion electrodes that mirrored actual gas diffusion electrodes with either Pt-black (continuous) or Pt/C (discontinuous) catalyst layers.

The model electrodes developed had defined surface geometries and catalyst distribution patterns (Paulus *et al.,* 2003). Figure 2.13 below illustrates the actual gas diffusion electrodes and the corresponding model systems.

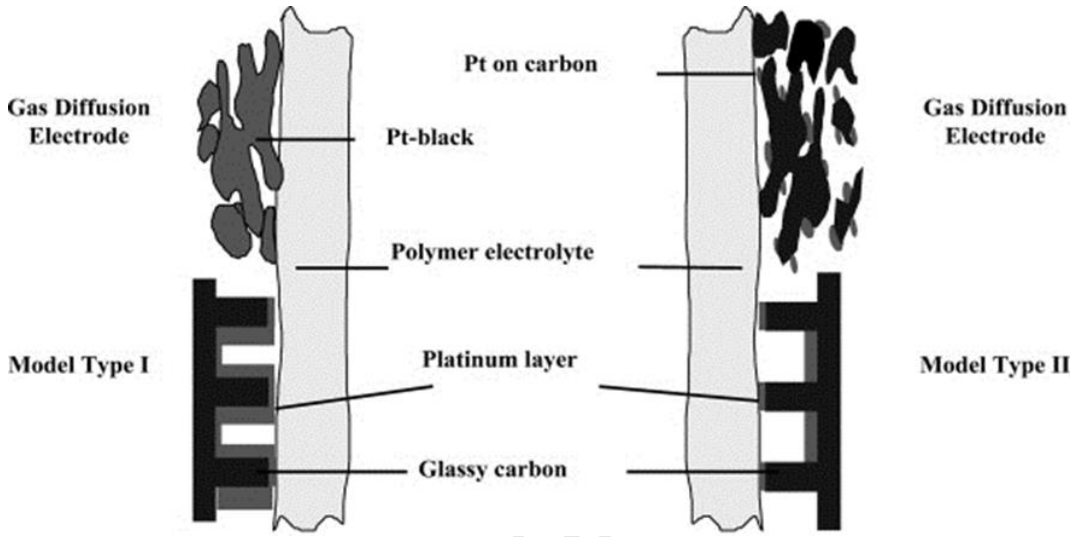

Figure 2.13 : Pt-black (right) and Pt/C (left) gas diffusion electrodes and their corresponding model electrodes made of glassy carbon sputtered with platinum (Paulus *et al.*, 2003)

The Pt-black model electrode is characterised by a continuous platinum layer see in Figure 2.13 (right), whereas the Pt/C model electrode has a discontinuous Pt layer on the surface of the glassy carbon. This models the real system where Pt occurs as isolated Pt nanoparticles that are not in contact in most cases.

Cyclic voltammetry was used to measure the electrochemically active surface area (ECSA) in both of the commercial gas diffusion electrodes in the absence of an ionomer phase in the catalyst layer, but with both catalyst layers in contact with a Nafion® membrane. For the Pt/C catalyst, a surface utilisation of 0.5% was found, whereas for the Pt-black, a surface utilisation of 80% was observed. This is a significant difference between the two catalyst surface utilisations and indicates that in the case of Pt/C only a small amount of the overall platinum surface is electrochemically active. The platinum in direct contact with the membrane is electrochemically active however platinum sites located away from the membrane have no proton conductive pathway to the membrane and are electrochemically inactive. In the case of the platinum-black however, platinum particles without

direct contact with the membrane electrolyte are still electrochemically active. This is an attribute of a continuous platinum surface, protons are able to travel from catalytically active platinum sites remote from the electrolyte membrane to the membrane itself over the metal surface. However, knowledge of the proton transport mechanism remains limited.

The model electrodes have proven that a continuous platinum surface provides a successful means of proton transfer from catalyst active sites to the electrolyte membrane in the absence of an ionomer phase in the catalyst layer. The exact hydrogen adsorption and transport mechanism is not known, however Paulus *et al.* (2003) proposed two potential scenarios for the proton transfer process over the platinum metal surface, illustrated in Figure 2.14.

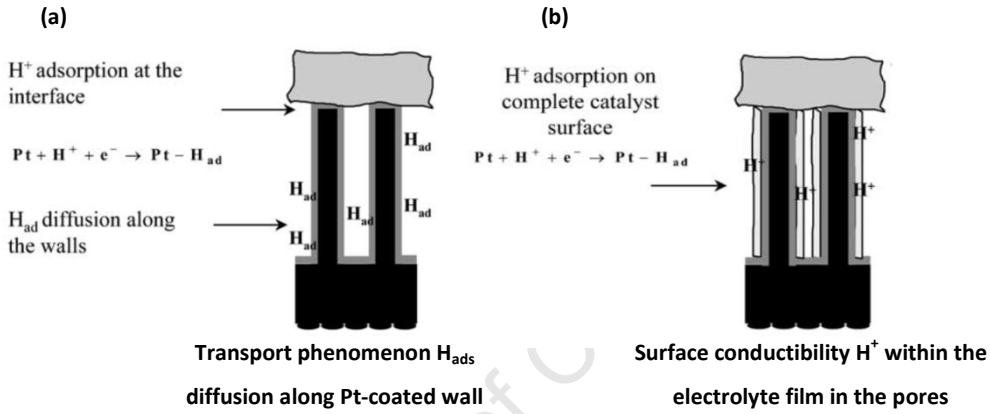

Figure 2.14 : Two possible H^+ transport mechanisms on a continuous platinum surface. (a) diffusion of adsorbed hydrogen species along the Pt-coated pore and channel walls and (b) surface conductivity caused by a liquid film formed on the metal surface possibly due to purging with humidified argon gas into the electrolyte solution (Paulus *et al.*, 2003)

Figure 2.14 (a) represents a time dependent mechanism, it is proposed that the H^+ ions adsorb at the platinum/Nafion® interface and the H_{ads} atoms diffuse along the pore and channel walls. This proposed mechanism is supported by evidence of decreasing platinum surface utilisation observed in the cyclic voltammograms as the sweep rate is increased, thus indicating the time dependence of the proposed proton transport mechanism occurring. An alternative mechanism of proton transport illustrated in Figure 2.14 (b) is based on surface conductivity by the formation of a conductive liquid film on the metal surface. The presence of this liquid film allows the diffusion of H^+ within the film and could explain the differing metal utilisations observed between the two model electrode systems. The wettability of platinum with water is greater than that on glassy carbon and as such a continuous platinum film with a liquid proton conducting film present allows more efficient proton transfer than on the glassy carbon surface (Paulus *et al.*, 2003).

The findings by McBreen (1985) and Paulus *et al.* (2003) open up an avenue of new research geared towards eliminating the necessity of the ionomer phase in the catalyst layer by the use of continuous platinum surfaces with proton conducting properties.

2.5 Extended surface area Pt catalysts vs supported Pt nanoparticles

Extended surface area (ESA) catalysts consist of large, thin-film-like surfaces with the area extended in two dimensions (Debe, 2012). ESA catalysts have various advantages over supported Pt catalysts, including 1) larger radii of curvature, making them less susceptible to surface area loss via Pt dissolution and re-deposition, 2) reduced mass transfer losses due to the thinner catalyst layer and 3) easier manufacturing (Debe, 2012). There have been many recent developments in ESA catalyst synthesis methods, however the nanostructured thin film catalyst (NSTF) by 3M is the most mature technology and the only ESA catalyst included in practical applications to date (Debe, 2012).

2.5.1 Nano Structured Thin Film (NSTF) catalysts

3M Inc. has developed a Nano Structured Thin Film (NSTF) catalyst as a novel means to enhance fuel cell performance and lower the amount of platinum used in PEM fuel cells. The NSTF catalyst has achieved the goal of reduced platinum loading with improved catalyst activity and stability without forfeiting fuel cell performance and durability (Sinha *et al.*, 2011). There are four main differentiating characteristics between NSTF catalysts and the conventional Pt/C catalyst, highlighted in the nature of 1) the catalyst support system, 2) the catalyst layer structure, 3) the synthesis process and 4) the NSTF electrodes (Debe, 2012).

2.5.1.1 Support system and catalyst structure

The NSTF catalyst support layer consists of highly-oriented, organic crystalline whiskers. Unlike conventional carbon black supports, the organic whisker-like support can withstand potentials above 2 V, and as such presents a corrosion resistant support system for fuel cell applications. The platinum catalyst itself is coated directly onto these whiskers in a thin film via chemical methods or vacuum sputtering deposition (Zhang *et al.*, 2009). This thin film structure results in a specific activity for the oxygen reduction reaction, 5 to 10 times greater than that achieved by 2-3 nm nanoparticles and is similar to that of bulk polycrystalline platinum (Debe, 2012). In NSTF electrodes approximately 20% of the whisker length penetrates the membrane and the rest of the whiskers are ionomer free. The organic whiskers themselves are highly inert and hence corrosion resistant. The scanning electron microscopy (SEM) images below in Figure 2.15 illustrates the highly oriented nature of the organic crystalline whiskers of the NSTF catalyst.

University of Cape Town

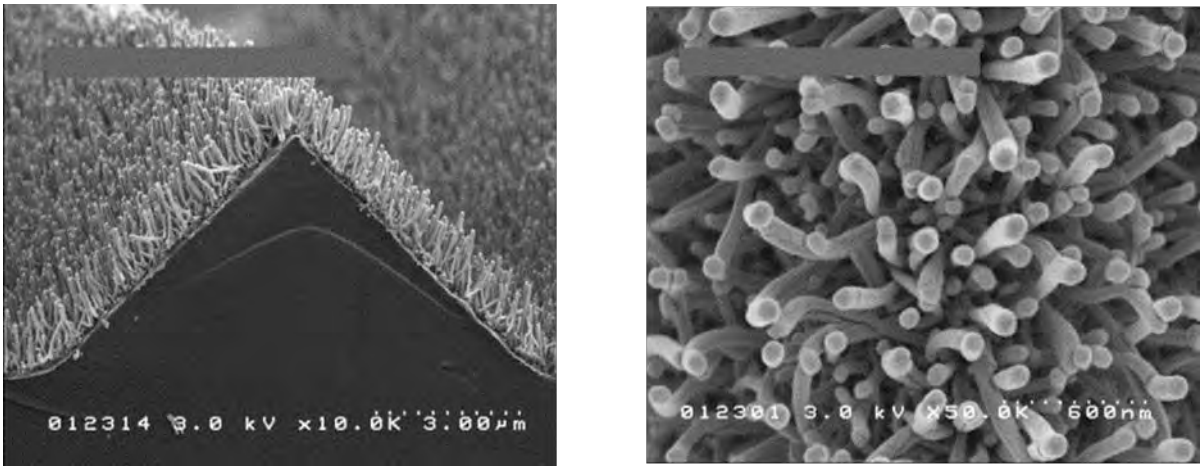

Figure 2.15 : Scanning electron micrographs (SEM) of typical NSTF catalysts as synthesised on microstructured catalyst transfer substrate, seen (left) in cross-section with magnification of x 10^5, and (right) in plan view with magnification of x 50^5 (Zhang *et al.*, 2009)

University of Cape Town

2.5.1.2 NSTF based catalyst layers

Proton transfer can occur along the continuous platinum surface of the NSTF catalyst. The three phase boundary condition is therefore met without the need for ionomer in the catalyst layer. This leads to an increase in metal utilisation. Furthermore, it is evident from Figure 2.16 below that the catalyst layer of an NSTF electrode is much thinner than that of a Pt/C electrode, 0.5 µm and 10 µm respectively. The NSTF electrode has a more compact, rigid structure, and thus produces a thinner catalyst layer. A thinner catalyst layer has the advantage of reducing mass transport limitations from the gas diffusion layer to the polymer electrolyte membrane, as gas and proton species have a shorter distance to travel compared to the catalyst layer in the Pt/C electrode. Figure 2.16 also displays the reason for lower metal utilisation in an electrode with a Pt/C catalyst layer. The three phase boundary condition must be met in order for an electrochemical reaction to occur, therefore every Pt particle must be in simultaneous contact with the ionomer, the reactant gas and the carbon particle. In reality it is improbable that this condition will be met for every single Pt particle, and as such the metal utilisation will be lowered.

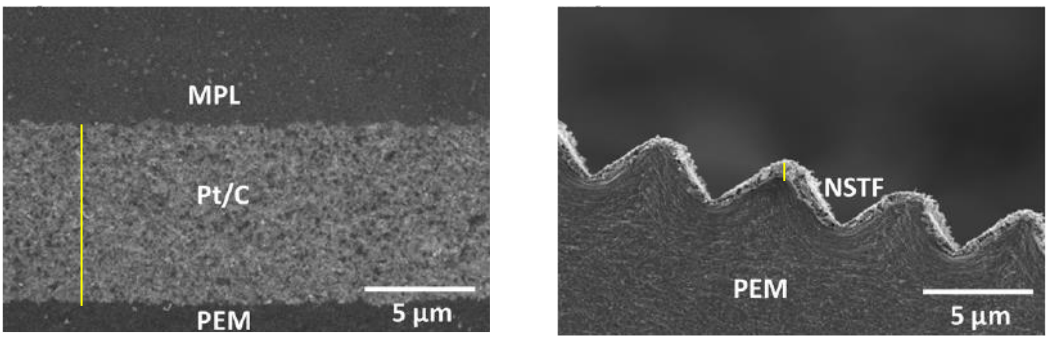

Figure 2.16 : Cross-sectional SEM images of (a) Pt/C electrode (b) NSTF electrodewhere the yellow line highlights the difference in catalyst layer thickness between the two electrodes (Sinha *et al.*, 2011).

The ability to decrease the overall platinum loading in the catalyst layer using NSTF catalysts while reaching comparable performances to commercial Pt/C catalyst is a very attractive attribute of this particular structure. The main issue, as discussed below, with NSTF catalysts is the incurred water management issue that arises from the dependence of the proton conduction mechanism on relative humidity.

2.5.1.3 Limitations of NSTF catalyst structure and performance

Despite the advances in specific activity and durability of the NSTF catalysts produced by 3M, there still remain some important operational issues that need to be addressed before establishing an operational membrane-electrode assembly (MEA) with an NSTF catalyst, for the use in a functioning fuel cell. A recent study by Kongkanand *et al.* (2012) highlighted some of the important operational shortcomings associated with the structure and performance of NSTF catalysts. One of the main issues associated with the operation of NSTF catalysts in PEM fuel cells is the poor proton conduction under relatively dry conditions. The membrane-electrode assemblies have also been found to require an additional pre-conditioning phase before operation which takes significantly longer than the pre-conditioning required for conventional catalysts systems (Kongkanand *et al.,* 2012). The importance of water management in NSTF catalyst fuel cell systems was also highlighted by a study performed by Sinha *et al.* (2011). The authors investigated the steady-state fuel cell performance of NSTF electrodes under partially humidified conditions at 80 °C. When compared to a conventional Pt/C electrode under partially humidified conditions at 80 °C it was found that in relatively wet conditions (60% inlet humidity), an NSTF electrode with a platinum loading of 0.15 mg_{Pt}/cm^2 shows a comparable performance to a Pt/C electrode with a platinum loading of 0.4 mg_{Pt}/cm^2. However at lower humidities i.e. drier conditions, the NSTF electrode had a poorer performance. It was hence concluded that the proton conductivity of the NSTF whiskers is strongly dependent on the relative humidity.

University of Cape Town

The understanding of the mechanism of proton transfer along a continuous platinum surface remains limited, however Paulus *et al.* (2003) have proposed several possible mechanisms by which proton transfer could occur. All proposed proton transfer methods require the presence of water, which would explain the high dependence of the NSTF electrode on relative humidity.

2.5.2 **Other extended surface area catalyst developments**

Another promising thin film technology that has attained an enhanced performance and stability relative to commercial Pt/C catalysts, is the meso-structured Pt thin film, developed by Kibsgaard *et al.* (2012). A mesoporous thin film is essentially a continuous high surface area structure, synthesised by the electro deposition of Pt into a mesoporous silica film template, see Figure 2.17. The inherent high surface area of a mesoporous structure eliminates the need for a carbon support material, thus making the effects of support corrosion on catalytic durability non-existent. Figure 2.17 below illustrates the enhanced stability of the mesoporous structure under accelerated stability tests.

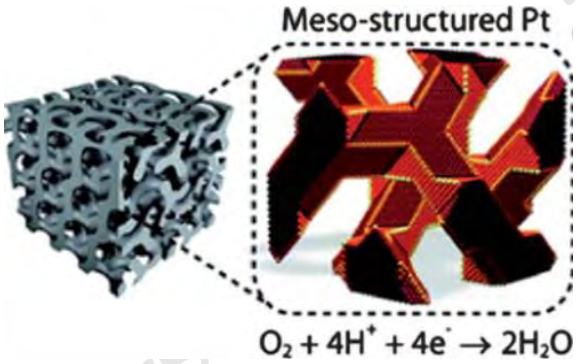

Figure 2.17 : (a) Structural model of thin film mesoporous double gryoid (DG) (Kibsgaard *et al*., 2012)

The morphology of the structure itself yields fewer undercoordinated Pt sites, commonly thought to reduce ORR activity, than Pt/C supported catalysts and hence accounts for the enhanced specific activity of the oxygen reduction reaction (Kibsgaard *et al*., 2012). This structure is superior to supported nanoparticle systems as the effects of particle sintering and other catalytic degradation mechanisms are eliminated (Zhang, 2013). This recent catalyst development is a promising alternative to the conventional supported catalysts used today, and emphasises the advantages of extended Pt surfaces with respect to enhanced stability and durability as well as improved specific activity (Kibsgaard *et al*., 2012).

Another developing catalyst technology is a new class of electrocatalysts based on Pt or Pt alloy nanotubes (PtNTs). Pt nanotubes provide similar structural ad durability advantages as the mesoporous thin films over commercial supported Pt/C catalysts. Porous Pt nanotubes have been

synthesised by Alia *et al.* (2010) via a galvanic displacement reaction using silver nano wires as the sacrificial template. The development of these porous PtNTs has indicated improved performance and durability relative to commercial Pt/C catalysts. The elimination of the carbon support and its associated durability issues, would allow for a thinner, more stable catalyst layer which would inherently improve mass transport and metal utilisation within the catalyst layer (Alia *et al.*, 2010).

2.6 Catalyst synthesis methods

Typical fuel cell catalysts consist of Pt nanoparticles deposited on a high surface area support (Zhang *et al.*, 2009). Multiple experimental approaches to synthesise platinum supported on carbon catalysts have been documented in literature and the most relevant methods to this study are summarised below. Each method has its own advantages depending on the end application of the catalyst required. The discussion underneath is focused on platinum deposition techniques that are relevant to and/or used in this work.

2.6.1 Metal-organic chemical vapour deposition (MOCVD)

MOCVD utilises metal-organic precursors for the deposition of metallic films on a substrate surface. The principle behind MOCVD involves the vaporisation of a metal-containing precursor, commonly an organometallic complex, which thermally decomposes and deposits a metal film onto a substrate material (Thurier and Doppelt, 2008). MOCVD has many advantages over wet chemistry methods as it avoids the time consuming stages of washing, drying and calcination. MOCVD is a gas phase method which inherently allows easy access to the pores of the support material (Aksoylu *et al.*, 2003). The ease of process control of the MOCVD method allows for the formation of highly dispersed, reproducible thin films (Aksoylu *et al.*, 2003). A typical MOCVD reaction comprises of the following series of steps and is illustrated in Figure 2.18 below:

1. Evaporation of metal containing precursor and convection of gases
2. Diffusion of gaseous precursor to the substrate surface or reaction of precursor to form intermediates
3. Adsorption of reactant species or intermediates to substrate surface
4. Surface migration to growth sites and surface chemical reaction resulting in film formation
5. Desorption of by-product species of surface reaction
6. Diffusion of by-products away from substrate surface
7. Evacuation of system gases

University of Cape Town

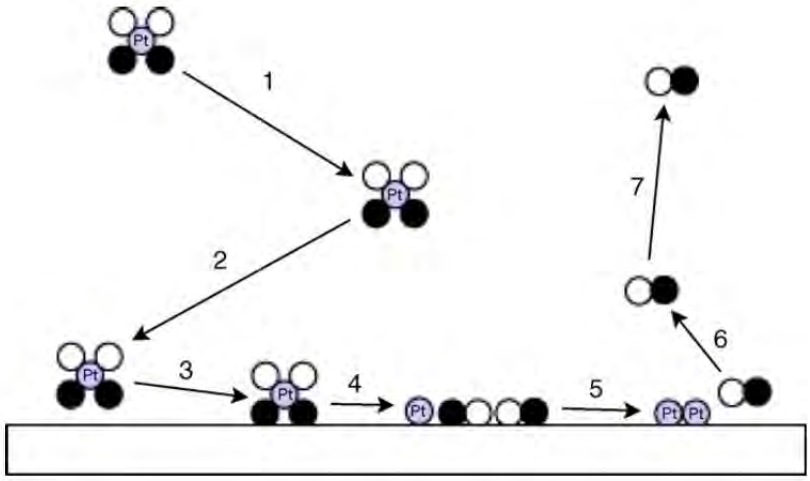

Figure 2.18 : Stages of a conventional MOCVD process (Thurier & Doppelt, 2007)

2.6.1.1 Deposition process and conditions

There are several strategies used to contact the substrate and precursor during an MOCVD reaction. Some of the most common include injection of the vaporised precursor with an inert gas into a reactor or a liquid delivery system in which the precursor is mixed with a solvent and contacted with the substrate by spraying (Thurier & Doppelt., 2008). Other methods of precursor substrate contact include plasma enhanced CVD, electron beam CVD and fluidised bed CVD each method with its own advantages for a specific reaction (Thurier & Doppelt., 2008). A vacuum is commonly used to increase the precursor volatility (Chu *et al.*, 1998).

Early MOCVD experiments observed autocatalysis in the absence of a carrier gas, however this was only possible if a crystalline Pt film was initially deposited, as a non-crystalline platinum layer may not be able to further catalyse the reaction. It was found that with the introduction of an inert carrier gas with small amounts of hydrogen, the platinum acted as a hydrogenation catalyst, thus eliminating the hydrocarbon part of the precursor into the gas phase (Thurier & Doppelt., 2008). The presence of hydrogen in the carrier gas was found to reduce the amount of carbon impurity in the film by approximately 5% (Xue *et al.*, 1992) and atomic hydrogen easily forms hydrides which aid in removing impurities from the growing film (Bahlawane *et al.*, 2012). Furthermore the inclusion of oxygen in the carrier gas produced the highest film purity. A recent study of iridium CVD at temperatures between 240-350°C showed that the addition of 2% oxygen to the carrier gas enhanced the film growth rate while decreasing the deposition temperature and activation energy (Bahlawane *et al.*, 2012).

University of Cape Town

2.6.1.2 Precursors requirements

Organometallic precursors contain a metal-carbon bond which breaks at relatively low temperatures depositing a metallic film (Niinisto, 2000). The requirements of a good precursor for MOCVD include (1) high volatility, (2) a good thermal stability range, (3) fast nucleation, and (4) low handling risk and stability towards moisture and oxygen (Thurier & Doppelt., 2008). Metal carbonyl compounds are commonly used as metal precursors for this purpose, owing to their high volatility and the stability of the CO ligand after dissociation (Bahlawane *et al.*, 2012). In the case of platinum however, $Pt(CO_4)$ is not thermally stable, but can be stabilised by the incorporation of another ligand such as phosphene. Some commonly used platinum precursors include platinum acetylene acetetonate $Pt(acac)_2$ and its derivatives ($Pt(hfa)_2$) they are relatively cheap and are vaporised at a temperature of 180 °C and decomposes on a hot substrate between 350 – 450 °C to produce uniform, crystalline films with minimum carbon impurities (Thurier & Doppelt., 2008).

2.6.1.3 Platinum acetylacetonate as a precursor for MOCVD

Platinum acetylacetonate, $Pt(acac)_2$ is an attractive precursor for the use in MOCVD as it is commercially available, stable in air and it has a relatively low decomposition temperature, between 210-240 °C (Battiston *et al.*, 2005). $Pt(acac)_2$ is from a class of compounds known as Beta-diketonates, which are of the form $M(CH_3COCHCOCH_3)_2$ where M is a metal. The structure of $Pt(acac)_2$ is given in Figure 2.19 below.

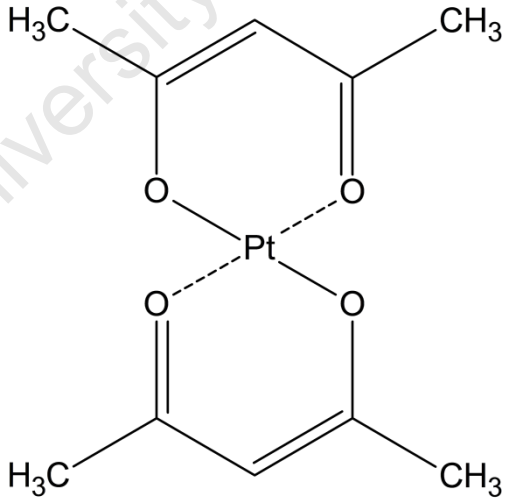

Figure 2.19 : Structure of platinum acetylacetonate molecule.

The Pt-O bond is strong, comparable to C-C bonds ($Pt\text{-}O_{acac}$: 180 kJ/mol and C-C : 140 kJ/mol) metal de-coordination does not take place, and it is therefore the ligand that decomposes. This means that high purity films are generally formed (Thurier & Doppelt., 2008).

University of Cape Town

Niinisto *et al*. (2000) studied the thin film growth of Ni, Cu and Pt by atomic layer epitaxy (ALE) using $M(acac)_2$ type precursors on different substrate materials (glass, Si, Al and Ti). The thermal behaviour of the three $M(acac)_2$ precursors was investigated using thermoGravimetric analysis (TGA) with N_2 as carrier gas and under reduced pressure. The curves below in Figure 2.20 were obtained.

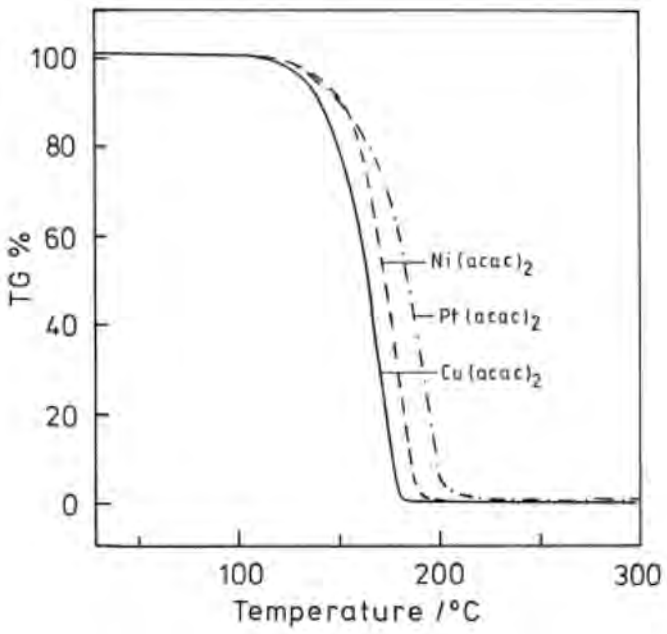

Figure 2.20 : TGA curves of $Ni(acac)_2$, $Pt(acac)_2$ and $Cu(acac)_2$ measured in a vacuum at a heating rate of 10 °C/min (Niinisto *et al*., 2000)

The graph shows that $Pt(acac)_2$ decomposes at approximately 200°C at these conditions, and as such this provides a basis for determination of the decomposition conditions of the $M(acac)_2$ precursors used for catalyst preparation.

2.6.2 Vapour deposition methods

The two major categories within vapour deposition methods are chemical vapour deposition (CVD) and physical vapour deposition (PVD).

2.6.2.1 Chemical vapour deposition

Chemical vapour deposition (CVD) is a powerful technique used for the deposition of thin films onto a substrate by the chemical reaction of a vaporised precursor and has been used extensively over the past few decades in the microelectronics and ceramics industry (Jones and Hitchman, 2009).

There have been significant advances in chemical vapour deposition (CVD) techniques since the 1980's, with investigations into different types of metal containing precursors, substrate pre-treatment methods and operating conditions, all of which have significant effects on the metal

particle dispersion or film formation (Thurier & Doppelt., 2008). There are several variations of the CVD technique ranging from metal-organic CVD (MOCVD), plasma enhanced CVD (PCVD) and atomic layer deposition (ALD), each with its associated advantages for the required deposition.

2.6.2.2 Physical vapour deposition

Physical vapour deposition is a film deposition technique carried out under vacuum by the vaporisation and deposition of the desired film material onto a substrate. Cathodic sputtering and thermal deposition methods such as vaporisation, are collectively known as physical vapour deposition (PVD). PVD techniques consist of four essential components: (1) they occur under vacuum, (2) they require a target to supply the source material, (3) they require a substrate material on which the film is to be deposited and (4) an energy supply to transport the target material to the substrate is needed (Zhang, 2008). PVD can be distinguished from CVD by the nature in which the film is formed, PVD involves the adsorption of atomic or molecular species on the substrate whereas CVD involves a chemical reaction of a vapour phase precursor (Jones & Hitchman, 2009). The diagram below in Figure 2.21, depicts the difference in how the metal film is deposited, PVD process involve a highly directional film deposition whereas CVD processes involve multidirectional film deposition using gas phase reactants.

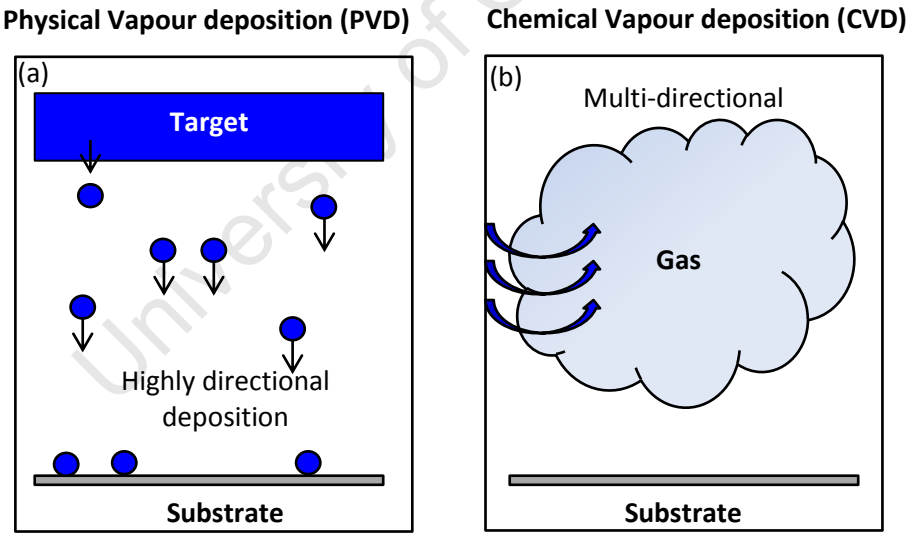

Figure 2.21 : Illustration of the main differences in directional deposition associated with (a) physical vapour deposition (PVD) and (b) chemical vapour deposition (CVD) of thin films (adapted from Jones and Hitchman, (2009))

The main advantage associated with vapour deposition methods is the uniform film distribution over the substrate and hence the absence of compositional gradients over the substrate. The vapour deposition techniques employed in this study are magnetron sputtering (PVD) and metal-organic chemical vapour deposition (CVD) and are detailed below.

University of Cape Town

2.6.3 **Magnetron sputter deposition**

As mentioned above sputtering is a physical vapour deposition (PVD) technique. All physical vapour deposition techniques follow the same series of steps: (1) they occur in a vacuum, (2) they require a source to supply the material, known as a target, (3) they require a substrate on which the material is deposited, (4) they require an energy source to transport the material from the source to the substrate (Zhang *et al.,* 2009). In recent years, this method of film deposition has gained increasing interest in the electrocatalysis field (Slavcheva *et al.*, 2009).

Cathodic DC sputtering involves the bombardment of a target (cathode) with high energy ions generally argon ions, generated from a glow-discharge plasma. Neutral argon atoms are introduced into a vacuum chamber, a DC voltage is applied between the target (cathode) and substrate (anode) which causes the argon atoms to ionise (Ar^+) creating a plasma. The charged Ar^+ ions are accelerated towards the target surface, which is essentially the metal to be deposited. The bombardment of the target with these ions causes target atoms to be knocked off the target surface and travel towards the substrate, where they condense into a film. The atoms coalesce on the substrate surface and bind to one another forming an atomic layer. The electrons released during the ionisation of Ar are accelerated towards the substrate, subsequently colliding with more Ar atoms and forming Ar^+ ions, thus continuing the process. A simple depiction of DC sputtering is illustrated in Figure 2.22 below.

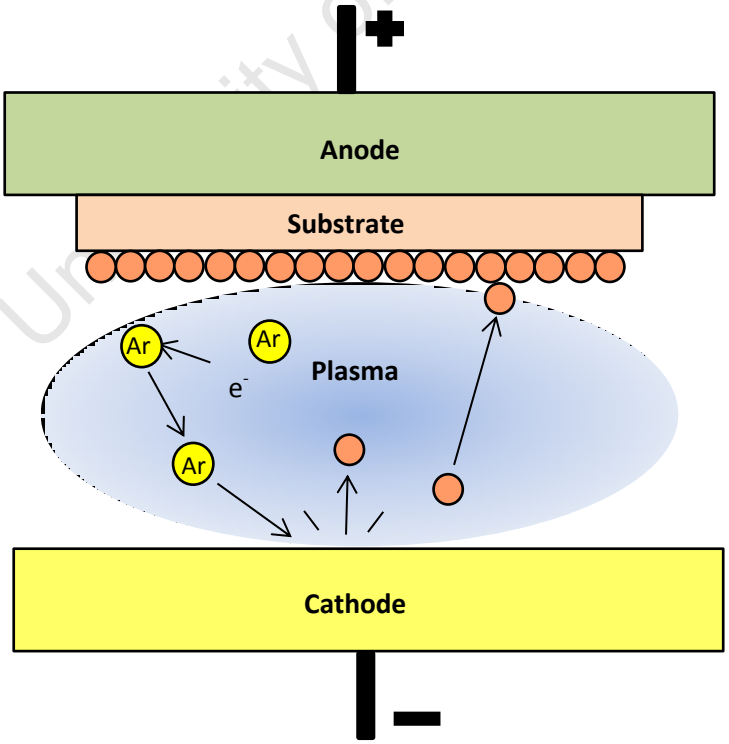

Figure 2.22 : DC sputtering system, Ar atoms ionised by a potential difference applied between the anode and cathode forming a glow discharge plasma. Ar^+ ions bombard target and knock of target atoms which are directed to the substrate surface where they deposit a metal film (Micro magnetics inc., 2013)

University of Cape Town

collisions and hence the sputtering efficiency. The magnetic field limits the movement of the electrons to the magnetic flux lines as opposed to electrons being attracted to the substrate surface and possibly damaging the developing film. This process is known as magnetron sputtering and is illustrated in Figure2.23 below.

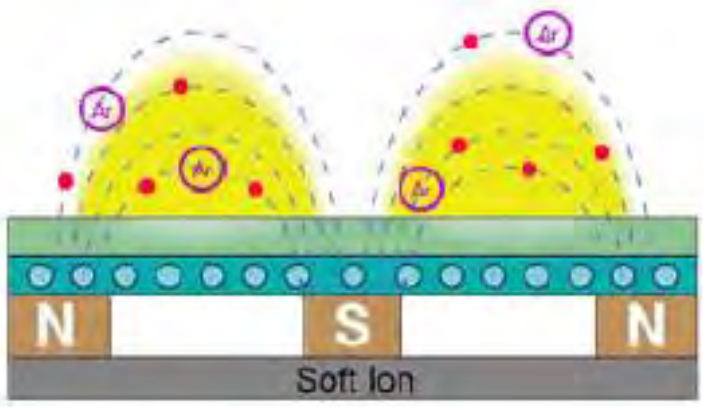

Figure 2.23 ; Magnetron sputtering system, plasma is confined to the area near the target surface by a strong magnetic field (Micro magnetics inc., 2013)

The magnetron sputtering method is reproducible and allows homogenous distribution of the metal particles on the substrate with very accurate catalyst loadings (Slavcheva *et al*., 2009). The quality of the film depends on the sputtering conditions, and Slavcheva *et al*. (2009) found that at low sputtering power and high sputtering pressure a mechanically stable crystalline Pt film with an extended surface can be obtained. The optimum conditions determined were 68mTorr argon pressure and 100 W DC power.

2.7 Electrochemical characterisation techniques

All electrochemical characterisation methods involve the use of an electrical signal as either an input or output to the system. Electrochemical instruments generate an input signal and the corresponding output signal can be measured. The signals are typically voltage, current and charge (Zhang, 2008). In an electrochemical system the region of greatest interest is the interface between an electronic conductor (the electrode) and an ionic conductor (the electrolyte) and the factors that influence the charge transfer across this interface when an electrical potential is applied and a current is generated. Charge is transferred by ions in the electrolyte phase and is transported through the electrode by the movement of electrons. In general, an electrochemical cell is defined by at least two electrodes separated by an electrolyte phase (Bard and Faulkner, 2001).

2.7.1 **Cyclic voltammetry (CV)**

Cyclic voltammetry has become an important electroanalytical technique in many areas of chemistry for the investigation of redox reactions (Kounaves, 1997). Cyclic voltammetry (CV) is a commonly used characterisation method for determining catalyst activity and the electrochemically active surface area (ECSA) of a catalyst.

The technique is based on varying the applied potential at the working electrode by sweeping the voltage linearly back and forth between two set voltages, and recording the resultant current(Wu *et al.*, 2008). Oxidation occurs on the forward sweep towards positive potentials and produces a positive anodic current, while reduction occurs on the reverse sweep and produces a negative, cathodic current. A plot of current versus voltage is known as a cyclic voltammogram. The peak potentials are important distinguishing features in a CV, as they indicate the potentials at which an electrochemical reaction occurs. Figure 2.24 below illustrates a typical cyclic voltammogram for polycrystalline platinum.

ape Town

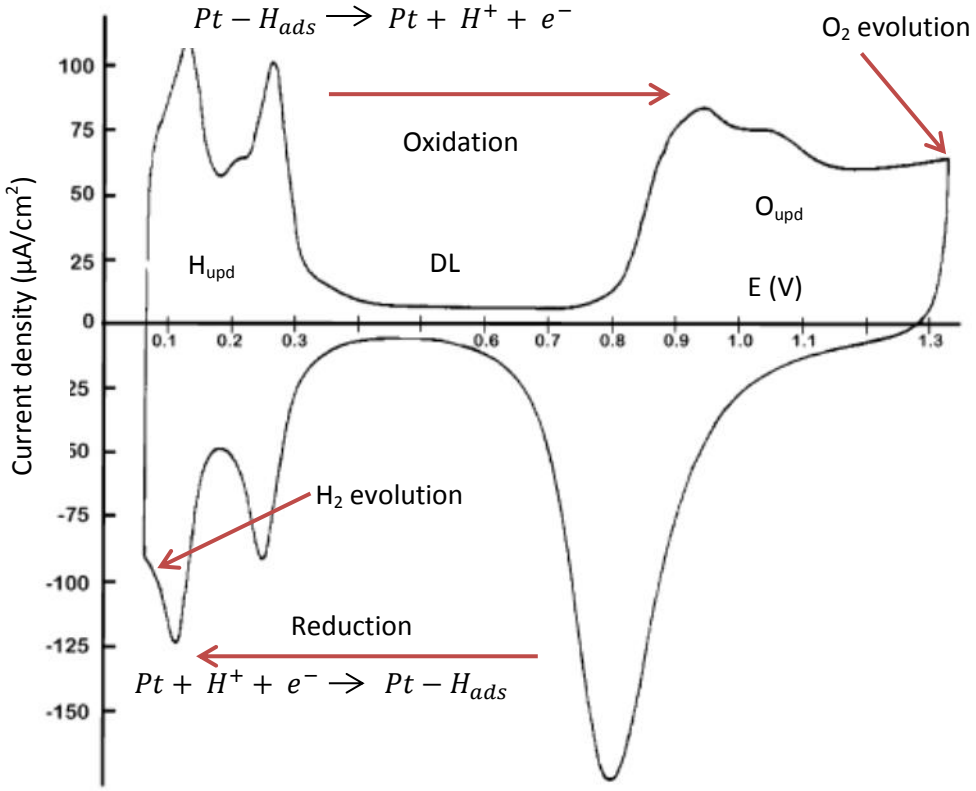

Figure 2.24 : Typical cyclic voltammogram for a polycrystalline Pt electrode in 0.5 M H_2SO_4 , sweep rate 50 mV/s (Climent &Feliu, 2011)

The region between 0 V and 0.4 V vs RHE is known as the hydrogen adsorption/desorption region, and is assigned as hydrogen underpotential deposition (H_{upd}) of a full monolayer of hydrogen in the negative sweep and the release of hydrogen ions (H^+) in the positive going sweep The adsorption and desorption of hydrogen ions on the platinum surface is a reversible process. Hydrogen adsorption to the platinum surface is illustrated in Figure 2.24 by the negative peaks occurring on the reverse sweep between 0.05 to 0.4 V *vs* RHE (Schmidt *et al.*, 1998). Hydrogen adsorbs to the platinum surface by the reduction reaction depicted in Figure 2.24. As the potential is swept in the positive direction, a positive anodic current is generated, and the reverse oxidation reaction occurs, seen in Figure 2.24, leaving a bare platinum surface.

The featureless region between 0.4 and 0.9 V vs. RHE, with a small observed current is attributed to the double layer charging (DL). It is essentially the movement of charge to and from the electrode surface, but does not correspond to an electrochemical reaction. Any peaks observed in this region could be due to impurities in the system (Climent & Feliu, 2011). The peaks occurring after 0.9 V vs. RHE denote oxygen adsorption and desorption (O_{upd}).

The presence of two or more hydrogen adsorption and desorption peaks in the low potential range has been found to be directly related to the type of platinum surface present (Mukerjee, 1989). Referring back to the cubooctahedral platinum particle model proposed by Kinoshita (1990) (see section 3.2.2) the three dominant crystal faces present on polycrystalline platinum surface are the (111), (100) and edge and corner sites (e+c). For an average particle size of 3.7 nm, the surface averaged-distribution of crystal faces is approximately 65% (111), 22% (e+c) and 13% (100) (Schmidt, 1998). Based on single crystal studies(Mukerjee, 1989), it was found that the first hydrogen desorption peak, occurring at a lower overpotential (0.12 V vs. RHE) corresponds to the more weakly bonded hydrogen species on the Pt (111) crystal face. The more positive hydrogen adsorption peak, occurring at a higher overpotential (0.27 V vs. RHE), corresponds to the more strongly bonded hydrogen species that occur on the Pt (100) crystal face (Mukerjee, 1989). The individual contributions of each Pt crystal face to the overall cyclic voltammogram is illustrated in Figure 2.25 below.

University of Cape Town

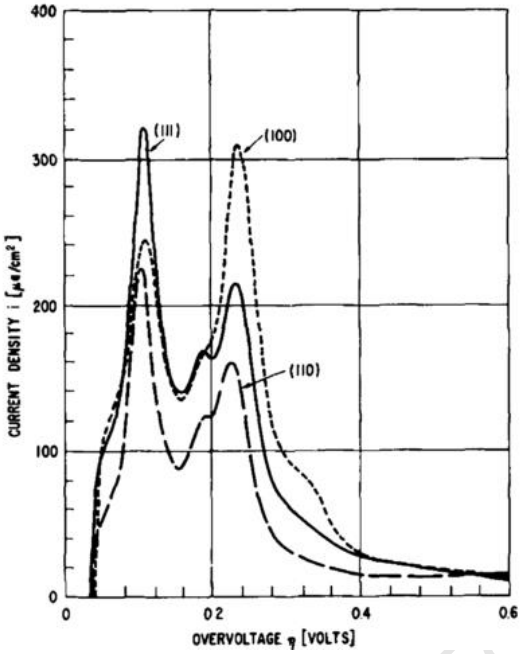

Figure 2.25 : Cyclic voltammograms for platinum single crystal faces (100), (111) and (110) at 25°C, sweep rate 0.1 V/s (Climent & Feliu, 2011)

A third peak was also observed at 022 V vs RHE in the positive sweep direction, and was attributed to the Pt (110) surface, only observed in the presence of a clean surface (Climent & Feliu, 2011).

Integration under the adsorption or desorption regions of the cyclic voltammogram and subtraction of the current due to double layer (DL) charging, yields the total adsorbed or desorbed hydrogen charge associated with the respective regions. By statistically adding hydrogen adsorption charges for different Pt crystal faces, the hydrogen adsorption charge associated with a smooth polycrystalline platinum surface has been found to be 210 μC/cm$^2_{Pt}$ (Wu *et al.*, 2008). Hence, the electrochemically active surface area or the number of active platinum surface atoms can be calculated using either the hydrogen adsorption or desorption charge.

2.7.2 **CO stripping voltammetry - to distinguish between Pt agglomerates and isolated nanoparticles**

CO stripping voltammetry is another common method used to determine the electrochemically active surface area (ECSA) of platinum catalyst systems. The principle behind this technique is similar to that of cyclic voltammetry, however an adsorbed monolayer of carbon monoxide (CO) on the platinum surface is oxidised with the resulting oxidation peak occurring between 0.76 and 0.95 V *vs* RHE (Maillard *et al.,* 2005). Assuming a charge of an adsorbed monolayer of CO on a smooth platinum surface to be 420 μC/cm^2, the ECSA can be determined.

Typically, the surface area determined by CO stripping is 1.4 times greater than that obtained by the H_{upd} method for high surface area supported platinum catalysts, and the difference was thought to be due to the significant contribution of the capacity of the carbon support material for high surface area catalysts. The support material contribution in this case, lead to an underestimation of the surface area for the H_{upd} method. Thus, subtraction of the carbon support contribution to the double layer charge was found to yield similar results to the surface area calculated by H_{upd}.(Mayrhofer *et al.*, 2008).

CO monolayer oxidation is a strongly size dependent reaction, and this is a major advantage of the technique, as it is possible to identify the presence of isolated and agglomerated Pt particles depending on the peak potentials. The CO oxidation peak for pure crystalline platinum is known to occur at a potential of 0.72 V *vs* RHE (Schmidt *et al.*, 1998). In general the CO stripping peaks observed in most high surface area supported catalyst systems with a range of particle sizes and hence differing distributions of active crystal faces, will be a superposition of the waves due to the CO oxidation on the respective crystal faces (Schmidt *et al.*, 1998). The CO oxidation reaction occurs at higher overpotentials for smaller Pt nanoparticles than for platinum agglomerates (Maillard, 2005). Maillard *et al.* (2005) reported a double voltammeric peak for CO oxidation for catalysts with a high Pt loading, see Figure 2.26 below.

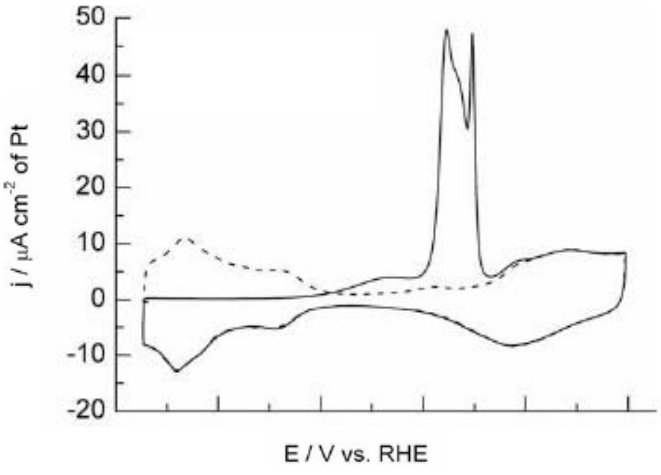

Figure 2.26 : A typical CO stripping voltammetry sweep (solid line) followed by the subsequent CO free cyclic voltammogram (dashed line) carried out in a 0.1 M $HClO_4$ solution at 10 mV/s, for an unsupported Pt nanoparticle system (Ciapina *et al.*, 2010).

It was ascertained that the double voltammeric peak was due to the CO oxidation reaction occurring on Pt agglomeratres and on isolated particles. The more negative peak corresponds to CO oxidation on Pt agglomerates and the more positive peak corresponds to Pt oxidation on isolated particles. The intensity of the peaks is indicative of the amount of Pt agglomerates or isolated particles present

on the catalyst surface. The Pt agglomerates were concluded to have a more enhanced catalytic activity compared to isolated particles as the CO oxidation overpotential occurs at a 90 mV lower potential than that for isolated particles. This enhanced activity is attributed to a high concentration of defects on the catalyst surface. The presence of the double voltammeric peak is significant as it provides an idea of the particle size distribution and the extent of particle agglomeration in a platinum supported catalyst sample (Maillard *et al.*, 2005).

2.7.3 **Rotating (Ring) disk electrode (R(R)DE) method – ORR activity**

Reactant species in a stagnant electrolyte solution are transported to and from the electrode surface by mass transport processes, mainly diffusion and convection, with diffusion being the dominant transport method (Qi, 2008). The mass transport rate can be increased and controlled by introducing a forced convection system. This is typically done by the use of a rotating disk electrode (RDE) or rotating ring disc electrode (RRDE). The rotation of the electrode causes reactant species to be dragged to the electrode surface where they react, and the subsequent product species are spun off at right angles to the surface due to the centrifugal force, see Figure 2.27.

University of Cape Town

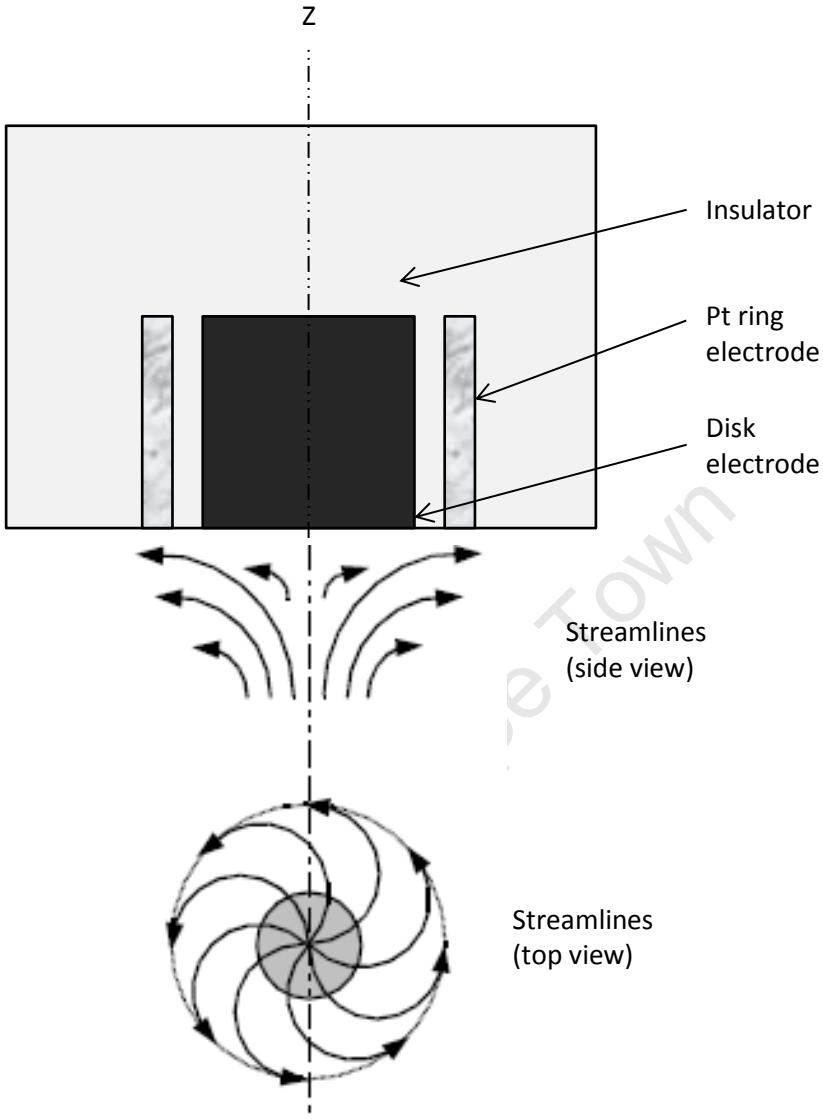

Figure 2.27 : Hydrodynamics of a rotating disk electrode indicating streamlines of a fluid (Bard & Faulkner, 2001)

There is a thin, stagnant reaction layer at the electrode surface through which the reactant is transported by diffusion. The thickness of this reaction layer is dependent on the rotation speed of the electrode. The greater the rotation speed of the electrode, the thinner the reaction layer (Qi, 2008). RDE experiments are employed to study the kinetics of electrochemical systems, specifically, in this study the activity of the oxygen reduction reaction (ORR). The kinetic current is the current under negligible mass transfer limitations and is expressed theoretically as follows

$$i_k = nFA_E K_f C \tag{2.5}$$

Where K_f is the rate constant dependent on overpotential, n is the number of electrons, A_E is the electrode surface area, C is the reactant species concentration and F is faradays constant.

At higher overpotentials, mass diffusion becomes significant and the reaction rate is dictated by the mass diffusion rate of the reactants to the electrode surface. The surface concentration of reactants is equal to zero at this point, as they are instantaneously consumed at the electrode surface. At this point a limiting current is reached which is directly proportional to the electrode rotation speed. The hydrodynamics of such systems have been rigorously examined and the resulting Levich equation accurately describes the effect of angular velocity (ω) on the limiting diffusion current of the system. The Levich equation is based on a smooth surface diffusion model and is illustrated below (Ke *et al.*, 2012).

$$i_d = 0.620nFA_E D^{2/3}\omega^{1/2}\nu^{-1/6}C \tag{2.6}$$

Where n is the number of electrons, F is the faraday constant, A_E is the electrode area, D is the diffusion co-efficient, ω is the angular rotation speed of the electrode, ν is the kinematic viscosity of the solution and C is the concentration of reactant.

The Levich equation applies to the mass transfer limited condition at the electrode surface and predicts the limiting diffusion current to be proportional to $\omega^{1/2}$ and the surface oxygen concentration (C) (Bard & Faulkner, 2001). The current starts to decrease after approximately 0.3 V *vs* RHE, and this phenomenon has been attributed to the adsorption of Hydrogen ions which hinders the ORR formation of H_2O and promotes H_2O_2 formation, which is a two electron process and inherently reduces the current produced by the reaction (Yang *et al.*, 2013).

The overall current produced in the system is related to both id and i_k by the Koutecky-Levich equation below

$$\frac{1}{i} = \frac{1}{i_k} + \frac{1}{i_d} \tag{2.7}$$

A plot of *1/i* versus $1/\omega^{1/2}$ yields a straight line, the slope of which can be used to determine the diffusion coe-efficient (D). Extrapolation of the line to infinite rotation speed, that is the intercept at ω=0, is essentially the point of zero mass diffusion and hence the pure kinetic region in the system (Garsany *et al.*, 2011). This point can therefore be used to determine the kinetic current of the system (i_K.), and the catalytic activity can be determined.

University of Cape Town

RRDE experiments are used to investigate the peroxide formation at the catalyst surface, by allowing the disk and ring to be held at different potentials, independent of one another. This allows the ORR to occur at the surface of the disk, and any undesirable peroxide species formed during the reaction will be reduced at the ring. The peroxide reduction reaction will result in a current signal which can be used to quantify the amount of H_2O_2 formed during the ORR. Figure 2.28 below illustrates the RRDE reactions occurring.

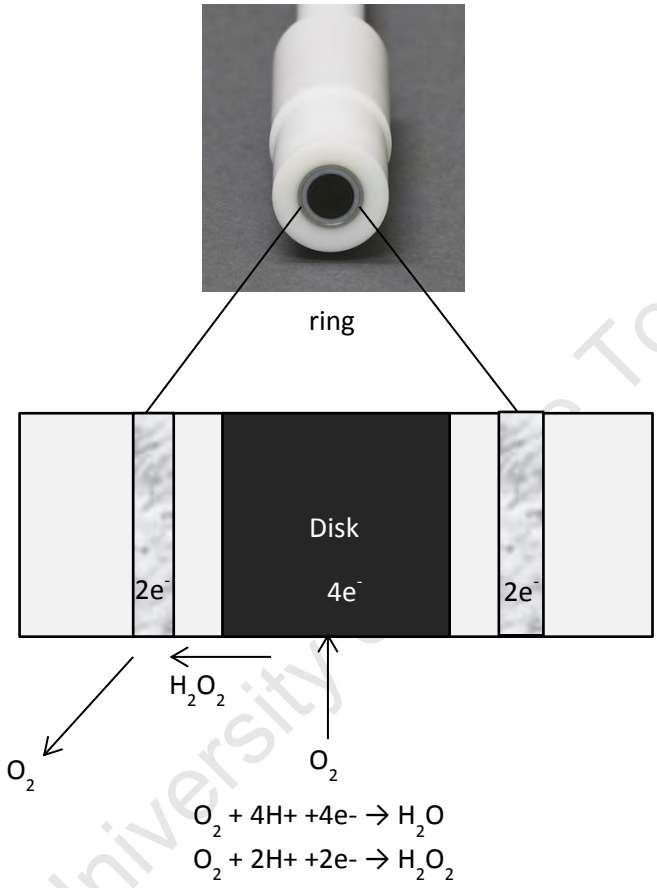

Figure 2.28 : RRDE mechanism of oxygen reduction at the disk and subsequent reduction of peroxide species at the ring

University of Cape Town

3. OBJECTIVES AND HYPOTHESES

To date the oxygen reduction reaction occurring at the cathode side of a PEM fuel cell is still a topic of avid research owing to its importance in PEFCs. The extensive research into this reaction has led to many new developments in understanding catalyst kinetics through density functional theory (DFT) studies as well as investigating novel catalysts support systems and alloys (Schmidt *et al.,* 2012). Reducing the overall platinum loading required in a PEFC is the ultimate goal of this area of research as it would enable PEFCs to become a cost-competitive electrochemical energy converter for the use in stationary and automotive applications (Schmidt *et al*., 2012). However there still remains an extensive amount of knowledge to be gained with respect to the ORR reaction which could further improve catalyst performance.

The particle size effect mentioned in the literature is a well-known phenomenon in this field of electrochemistry and serves as a compass for developing ORR catalysts with high activities. This study talks to the importance of investigating further the particle size effects of platinum nanoparticles supported on carbon on the ORR activity. A model electrode and a conventional platinum on carbon system will be compared in this study. The extensive research on this particular topic, namely platinum supported on carbon catalysts and the particle size effect, will allow a rigorous comparison of data as well as the opportunity for new insights to be developed. The current study aims to do the following:

- Develop a model catalyst electrode system by magnetron sputter deposition of platinum onto a model substrate surface, with controlled platinum loadings.
- Increase platinum loading in the model system such that the system exhibits isolated platinum nanoparticles at low platinum loadings and an extended surface or platinum agglomerates at high platinum loadings.
- Develop a corresponding “real” catalyst system by MOCVD with platinum weight percentages varying from low to high (20 to 80 wt.%).
- Observe the transition between isolated platinum nanoparticles and extended platinum surfaces by physical and electrochemical characterisation.
- Study the effects of surface morphology and particle size on the activity of the ORR and the formation of hydrogen peroxide species
- Observe the particle size effect as platinum loading increases and the surface changes from isolated platinum nanoparticles to an extended platinum surface

University of Cape Town

Following the above objectives for this study the following hypotheses have been derived and will be answered in this study.

- Increasing the platinum loading on the substrate in the model electrode system will lead to the formation of platinum agglomerates and an extended platinum surface at high platinum loadings
- Increasing the weight percentage of platinum deposited on a carbon support by MOCVD will lead to particle agglomeration and an extended platinum surface at high platinum loadings.
- The electrochemically active surface area (ECSA) will increase as platinum loading increases, in both the model and real catalysts systems.
- Area specific activity ($i_{k,spec}$) will increase and mass specific activity ($i_{k,mass}$) will decrease, as platinum loading increases for both model and real catalyst systems.
- Extended platinum surfaces increase catalyst utilisation per mass of catalyst

University of Cape Town

4. EXPERIMENTAL PROGRAMME

The experimental programme below details the preparation and characterisation of platinum supported on carbon catalysts prepared by two different methods, namely magnetron sputter deposition and metal-organic chemical vapour deposition (MOCVD) a rudimentary design based on literature. Sputtering was used to develop model electrodes with a range of Pt loadings, the sputtered model electrode system was developed during a three month internship at the Paul Scherrer Institute (PSI) in Switzerland, where the unique sputtering technology was available for this specific study. The MOCVD Pt/C catalysts were prepared at the Department of Chemical Engineering at the University of Cape Town (UCT).

The table below summarises the chemicals and gases used for the electrochemical measurements and catalysts preparation techniques in this study.

Table 4.1 : List of chemicals and gases used for electrochemical measurements and catalyst preparation techniques

Chemical	Chemical formula	Supplier	Purity grade
Conc. Perchloric acid	$HClO_4$	Sigma Aldrich	70%
Conc. Sulphuric acid	H_2SO_4	Kimix Chemicals	98%
Hydrogen Peroxide	H_2O_2	Kimix Chemicals	99.9%
Iso-propanol	C_3H_7OH	Kimix Chemicals	99.9%
2-propanol	C_3H_8O	VWR Prolabo	99.8%
Nafion solution	-	Dupont™	5%, 15%
Platinum acetylacetonate	$Pt(acac)_2$	Sigma Aldrich	-
Vulcan XC72R	carbon	Electrochem	-
Argon	Ar	Air Liquide	99.999%
Oxygen	O_2	Afrox	99.998%
Carbon monoxide	CO	Air Liquide	95%

University of Cape Town

4.1 Catalyst synthesis techniques

The catalyst synthesis techniques detailed below describe the preparation of the sputtered model electrodes prepared and characterised at the Paul Scherrer Institute (PSI) and the MOCVD catalysts prepared and characterised at the Department of Chemical Engineering at University of Cape Town.

4.1.1 Sputtered model electrodes (Paul Scherrer Institute, Switzerland)

Model electrodes were prepared by magnetron sputter deposition onto a Vulcan surface which was deposited onto the surface of a glassy carbon rotating disk electrode (Pine Instruments), with various Pt loadings ranging from 2 to 100 µg/cm^2. The model electrodes were prepared in two stages. A Vulcan suspension was made by mixing 75 mg of Vulcan XC72R with 100 µL Nafion®

solution (5 %, Fluka) and 25 mL 2-propanol (Normapur®, VWR Prolabo). The solution was ultrasonicated at 60 °C for 10 minutes and then stirred at 40 °C for 10 minutes (Rabis *et al.*, 2012). A 20 µL sample of the Vulcan suspension was pipetted onto the surface of a polished glassy carbon rotating disk electrode (RDE) and dried overnight in an argon purged desicator at room temperature.

The second stage of electrode preparation involved magnetron sputter deposition of platinum metal onto the electrode surface with different platinum loadings, 2, 10, 20, 50 and 100µg/cm^2. In order to avoid platinum metal being deposited on the Teflon part of the electrode, Kapton® tape was used to cover the teflon part of the electrode by punching a 5 mm size hole in the tape and placing it over the teflon part of the electrode. This allowed exposure of only the disk part of the electrode during magnetron sputter deposition of platinum; Figure 4.1 below illustrates this process.

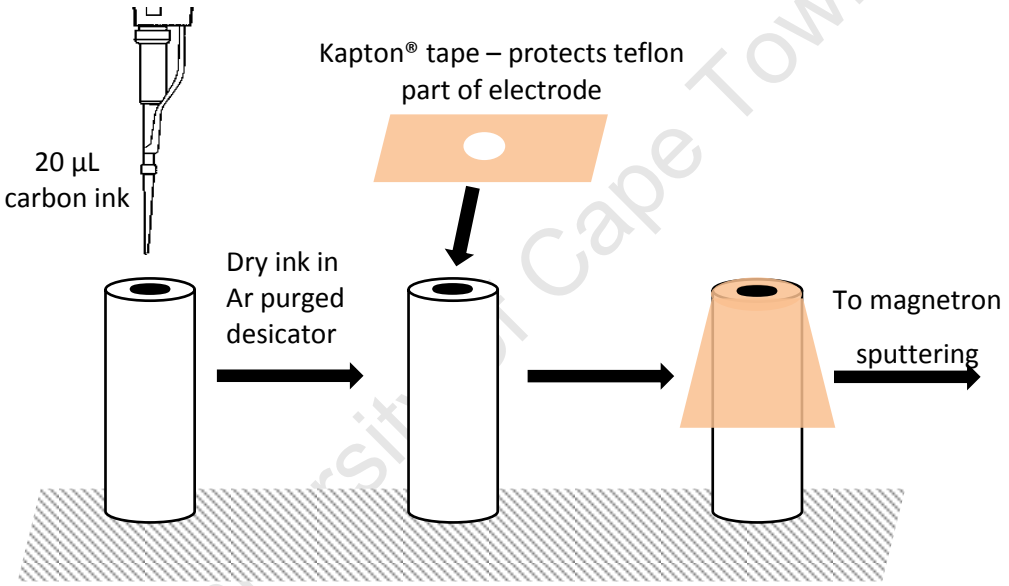

Figure 4.1 : Kapton® tape application to protect Teflon during magnetron sputtering

A magnetron sputtering set-up ('TIPSI' at the PSI Laboratry of Developments and Methods) was used to deposit the various Pt loadings onto the Vulcan surface on the prepared electrodes. argon was used as the sputter gas at a pressure 10^{-3} mbar with a sputtering power of 500 W. Rutherford Back Scattering (RBS) spectroscopy was used to determine the Pt loading, as described elsewhere (Schwanitz *et al.*, 2012). The sputtering setup is illustrated in Figure 4.2 below.

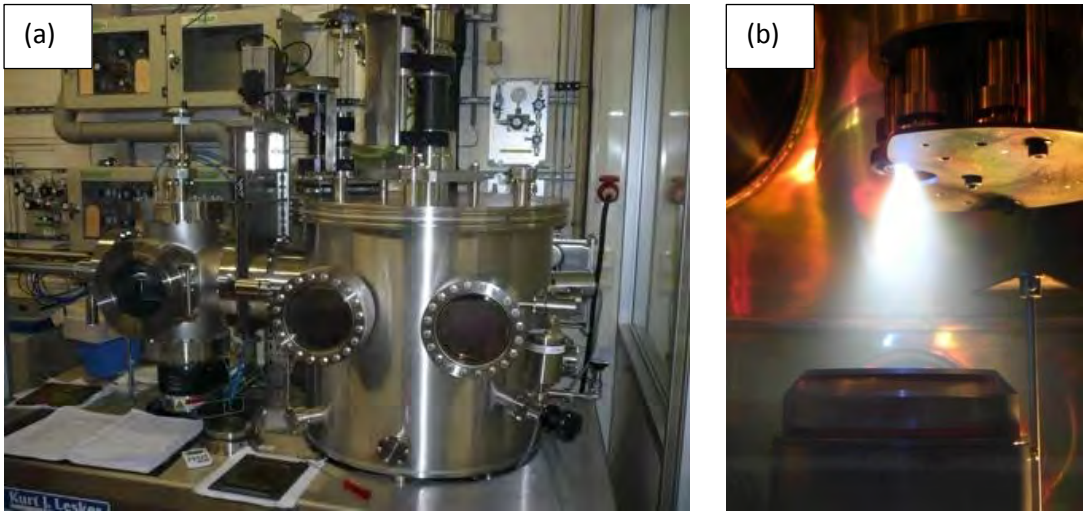

Figure 4.2 : (a) Illustration of a magnetron sputtering setup. (b) Ar plasma generated between the target and the substrate material (Kurt J. Lesker , 2013)

The sputtered model electrodes were then characterised using the electrochemical methods described in Section 4.2 below.

4.1.2 MOCVD Pt/C catalysts preparation (HySA, Cape Town)

The reactor illustrated in Figure 4.3 below was used to prepare the supported Pt/C catalysts by a rudimentary design based on literature of the MOCVD method. The amount of $Pt(acac)_2$ required to make a specific weight % Pt/C was calculated using a 125 mg Vulcan XC72 basis for the low Pt loadings and a 50 mg Vulcan XC72 basis for the higher Pt loadings .The table below summarises the masses of $Pt(acac)_2$ required for each Pt loading.

Table 4.2 : Summary of mass of Vulcan XC72 and $Pt(acac)_2$ required for each MOCVD catalyst

wt.% Pt	Mass Vulcan XC72 (mg)	Mass $Pt(acac)_2$ (mg)
20	125	63
40	125	168
60	125	378
80	50	403

University of Cape Town

Figure 4.3 : Reactor used for the preparation of MOCVD catalysts (Haynes alloy) the main body sits within the furnace, whilst some of the evacuation line remains outside the furnace.

The conditions and technique used to prepare the MOCVD catalysts of different wt.% Pt were of a rudimentary design, based on literature and a thermoGravimetric analysis (TGA) of the decomposition rate and temperature of the $Pt(acac)_2$ precursor.

The pre-weighed Vulcan and $Pt(acac)_2$ powder was mixed using a mortar and pestal, and loaded into the reactor. The reactor was closed and tightened and inserted into the furnace (Labofurn, Kiln Contractors). An argon line was connected to the one end of the reactor, and argon gas was flowed through the reactor at 50 mL/min. A filter at the reactor exit prevented the catalyst particles from leaving with the gas flow. The furnace temperature was ramped to 100 °C over a 20 minute interval, and held at 100 °C for 30 minutes to remove any water vapour from the vessel. The reactor was then closed off to the argon flow by two on/off valves on either end of the reactor, thus trapping the argon gas inside the reactor volume for the duration of the reaction. The temperature was then ramped to 150 °C over a 1 hour period and held at 150 °C for 30 minutes. Finally the temperature was ramped to 240 °C over a 30 minute period and held at this temperature for 1.5 hours. The reactor was then cooled to room temperature over-night, while maintaining the argon atmosphere within the reactor volume. The catalyst was removed the following day and stored in a labelled glass vial.

Electrochemical characterisation was carried out on the MOCVD catalyst samples by first preparing the catalyst ink as in Section 4.2.2 and then following the characterisation techniques detailed in Sections 4.2.3 to 4.2.5.

University of Cape Town

4.2 Rotating (Ring) disk electrode (R(R)DE) measurements

The catalyst synthesis techniques detailed below were employed during the experimental part of this project. They entail the preparation of the sputtered model electrodes prepared and characterised at the Paul Scherrer Institute (PSI) and the MOCVD catalysts prepared and characterised at the Department of Chemical Engineering at University of Cape Town.

4.2.1 Cell setup and preparation

Rotating ring disk electrode (RRDE) experiments were conducted in a typical three-compartment electrochemical cell (Gamry Instruments) see Figure 4.4 below, using a SP-300 bipotentiostat (Biologic Science Instruments) and rotation control (Gamry instruments). A platinum mesh counter-electrode (Figure 4.4 B) and a $Hg/HgSO_4$ reference electrode (Figure 4.4 C) were used for measurements, with all potentials being reported in terms of the reversible hydrogen electrode scale (RHE) for the sputtered model electrodes and in terms of the standard hydrogen electrode (SHE) for the MOCVD catalysts. A 0.1 M $HClO_4$ electrolyte solution was used in all experiments and was prepared using 18.2 MΩ.cm deionised water (nanopure) and concentrated $HClO_4$ (Sigma Aldrich).

Glassware was thoroughly cleaned before each experiment. All glassware was submerged in a 1:1 solution of hydrogen peroxide and concentrated sulphuric acid, and left to soak overnight prior to measurements. The clean glassware was then removed from the cleaning solution and transferred to a beaker and rinsed several times using 18.2 MΩ.cm deionised water (nanopure). Caution was taken when dealing with the H_2O_2/H_2SO_4 solution, and heavy duty rubber gloves and a face shield were employed when handling the cleaning solution and glassware.

The 5.61 mm diameter glassy carbon working electrode (Pine instruments, E7R9 Series) (Figure 4.4 A) used for RRDE measurements, was thoroughly polished to a mirror finish using a 1 µm followed by a 0.05 µm alumina solution (Buehler). Surface impurities were removed from the platinum mesh counter electrode by holding it in the flame of a blow torch for 15 seconds and immediately rinsing with distilled water to cool the platinum mesh before inserting it into the electrochemical cell.

The typical electrochemical characterisation sequence was carried out in the following order:

Cyclic voltammetry ⟶ CO stripping voltammetry ⟶ RDE ⟶ RRDE

University of Cape Town

All electrochemical measurements were performed consecutively. A fresh batch of electrolyte was prepared before a set of electrochemical measurements was carried out. The electrochemical characterisation of a particular platinum loading could be carried out within a 9 hour period.

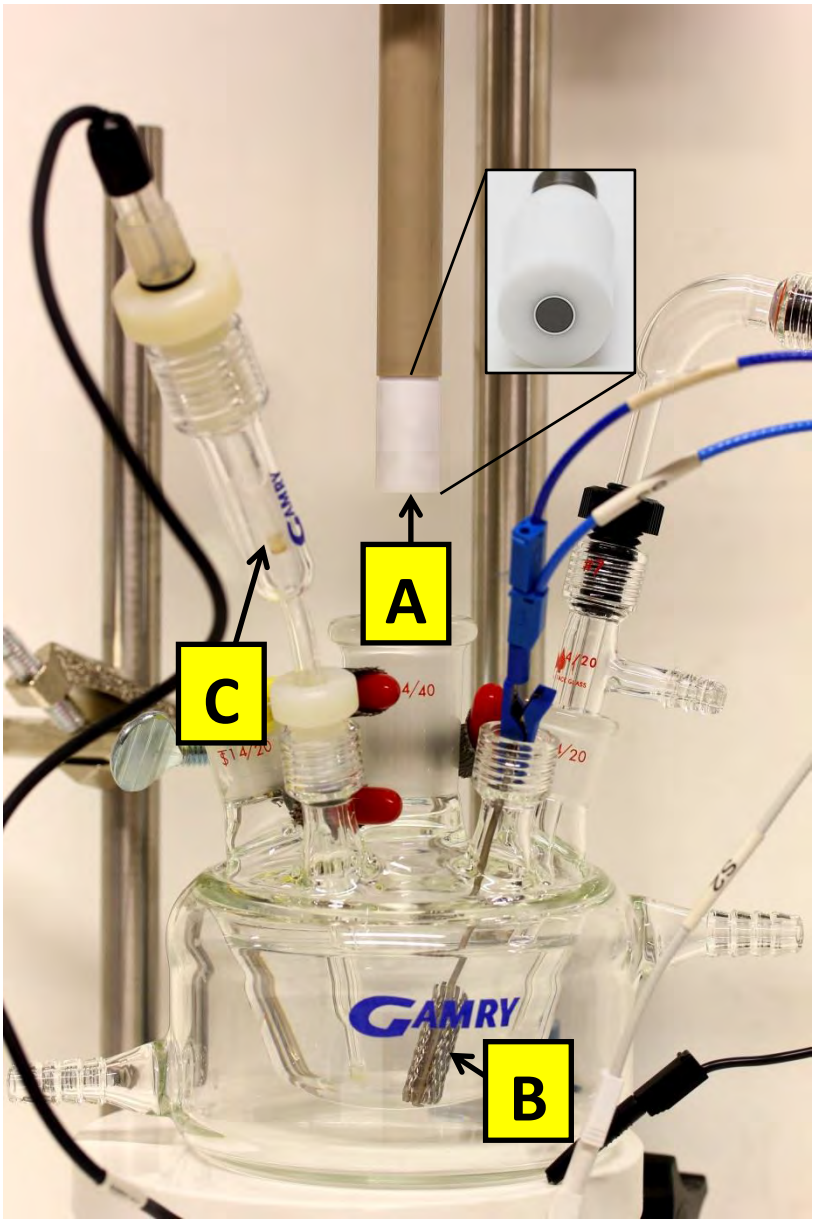

Figure 4.4 : Experimental setup where A: glassy carbon rotating ring disk working electrode (Pine instruments), B: Platinum mesh counter electrode, C: Hg/$HgSO_4$ reference electrode.

4.2.2 **MOCVD catalyst ink and thin film RDE preparation**

The catalyst ink deposited on the glassy carbon electrode disk surface was prepared in a glass vial using 10 mg of catalyst, 10 mL of 18.2 MΩ.cm deionised water (nanopure), 3 mL of isopropanol (Kimix) and 50 µL of 15 wt. % Nafion® solution (Dupont™). The catalyst ink solution was placed in a beaker of ice and ultrasonicated for 20 minutes. A 15 µL volume of catalyst ink was pipetted, using a micropipette, onto a stationary 5.61 mm glassy carbon rotating ring disk electrode (Pine Instruments, E7R9 Series). The electrode was dried in air while being rotated at 700 rpm on a rotator shaft (Gamry Instruments) in order to obtain a uniform film, see Figure 4.5 (Garsany *et al.*, 2010). Once the thin film RDE was dry, the surface of the electrode was wetted using 18.2 MΩ.cm deionised water (nanopure) and submerged in the electrolyte solution under potential control (0.5 V vs. SHE). The mass of catalyst in the ink solution and the respective catalyst loadings on the glassy carbon disk electrode are listed in the table below for the different weight % of each MOCVD catalysts sample.

Table 4.3 : Summary of predicted platinum loadings for each platinum weight % MOCVD catalyst

Wt% Pt	Mass Catalyst in 13050 µL ink (mg)	Predicted Pt loading (µg/cm^2)
20	10	9.30
40	10	18.6
60	10	27.9
80	10	37.2

The experimental catalyst loadings can be seen in Table 5.12 (Section 5.4.4).

University of Cape Town

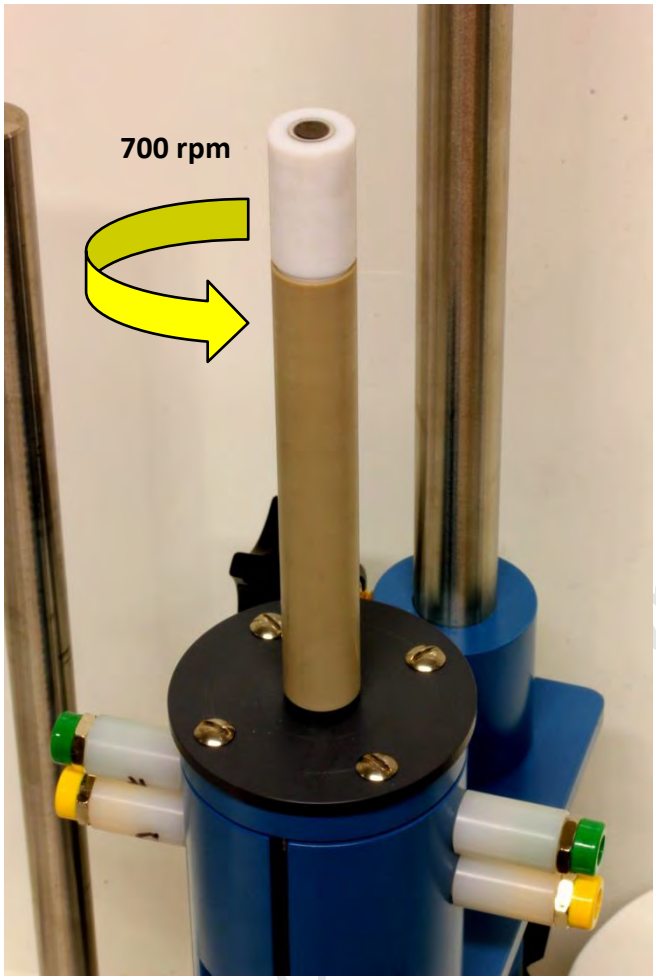

Figure 4.5 : Rotation drying method for thin film preparation. Rotation speed 700 rpm

4.2.3 Cyclic voltammetry

Cyclic voltammetry was used to determine the electrochemically active platinum surface area (ECSA) of the catalyst samples at room temperature in an argon saturated, 0.1 M $HClO_4$ electrolyte solution. The electrolyte solution was deoxygenated by purging with argon gas for 40 minutes, until saturated, before the insertion of the electrode under potential control (0.5 V vs. SHE/RHE). The gas flow was reduced during measurements to ensure no gas bubbles stuck to the electrode surface. The potential of the working electrode was cycled between 0 and 1.0 V vs. SHE/RHE at 100 mV/s for 50 cycles to electrochemically clean the catalyst surface of any surface impurities, until a stable CV was observed. The sweep rate was then reduced to 50 mV/s and a stable CV was recorded after 3 cycles. Current densities were reported in terms of the geometric surface area of the glassy carbon disk electrode (mA/cm^2) or the mass of platinum on the glassy carbon surface (mA/mg_{Pt}).

The resulting cyclic voltammogram was analysed by integrating and averaging the charge (µC) associated with the hydrogen adsorption and desorption regions and correcting for the double layer

charge. The hydrogen adsorption charge associated with a smooth polycrystalline platinum surface was taken to be 210 μC/cm^2_{Pt} and was used to calculate the ECSA in (cm^2_{Pt}/g_{Pt}) and (cm^2_{Pt}/cm^2) according to the equations below

$$ECSA\left(\frac{cm^2_{Pt}}{g_{Pt}}\right) = \frac{charge\ (\mu C)}{210\left(\frac{\mu c}{cm^2_{Pt}}\right).catalyst\ loading(g_{Pt})} \tag{4.1}$$

$$ECSA\left(\frac{cm^2_{Pt}}{cm^2}\right) = \frac{ECSA\left(\frac{cm^2_{Pt}}{g_{Pt}}\right)\ x\ mass\ Pt\ (g_{Pt})}{geometric\ surface\ area\ (cm^2)} \tag{4.2}$$

4.2.4 **CO stripping voltammetry**

CO stripping voltammetry was an alternative method used to determine the ECSA of the Pt/C catalysts. A CO saturated electrolyte was achieved by bubbling CO gas into the electrolyte solution for 20 minutes, the potential of the working electrode was held constant at 0.1 V vs. SHE/RHE during saturation, the potential at which CO adsorbs to the platinum surface (Maillard *et al.*, 2005). The electrolyte was then purged with argon gas for 20 minutes to remove the dissolved CO gas. Two cyclic voltammograms were recorded with a sweep rate of 20 mV/s between 0 and 1.0 V vs. SHE/RHE. Sweep 1 corresponded to the oxidation of CO from the platinum surface and sweep 2 was a CO free CV. The platinum ECSA was determined assuming a 420 μC/cm^2_{Pt} per CO monolayer adsorbed on the platinum surface, according to the equation below.

$$ECSA\left(\frac{cm^2_{Pt}}{g_{Pt}}\right) = \frac{charge\ (\mu C)}{420\left(\frac{\mu c}{cm^2_{Pt}}\right).catalyst\ loading(g_{Pt})} \tag{4.3}$$

4.2.5 **Oxygen reduction reaction**

Oxygen reduction reaction measurements were carried out in an oxygen saturated $HClO_4$ electrolyte solution. The electrolyte was purged with oxygen gas for 40 minutes prior to measurements. The working electrode was immersed in the electrolyte under potential control. ORR curves were measured at rotation speeds of 400, 900, 1600 and 2500 rpm. The potential of the working electrode was swept from 1.0 V vs. SHE/RHE to 0 V vs. SHE/RHE (cathodic sweep) at 20 mV/s. The reverse sweep (anodic sweep) was also measured, from 0 V to 1.0 V vs. SHE/RHE at 20 mV/s.

University of Cape Town

The cathodic sweep was used to analyse the mass and specific activities of the Pt/C catalysts. The ORR curves obtained in an oxygen saturated electrolyte were corrected for the capacitive current associated with Pt/C catalysts, by subtracting a CV measured in an argon saturated electrolyte with a sweep rate of 20 mV/s, between 0 V and 1.0 V vs. SHE/RHE. The diffusion limiting current (i_d) for each rotation speed was seen as the flat part of the ORR curve, and the value of i_d was recorded at approximately 0.4 V vs. SHE/RHE for each curve. The measured diffusion limiting current (i_d) was compared to the theoretical diffusion limiting current ($i_{d,\ theoretical}$) calculated according to the Levich equation 4.4 below as a comparison.

$$i_{d,theoretical} = 0.620nFA_E D^{2/3}\omega^{1/2}\nu^{-1/6}C \tag{4.4}$$

Where n is the number of electrons, F is the faraday constant, A_E is the electrode area, D is the diffusion co-efficient, ω is the angular rotation speed of the electrode, ν is the kinematic viscosity of the solution and C is the concentration of reactant.

The theoretical values of the diffusion limiting current at different rotation speeds are listed in the table below for a RRDE (Pine Instruments, E7R9 Series) with an outer disk diameter of 5.61 mm and a RDE (Pine Instruments) with a disk outer diameter of 5 mm.

Table 4.4 : Summary of diffusion limiting currents (mA) and current densities (mA/cm^2) for a 5 mm diameter glassy carbon (GC) disk electrode and a 5.61 mm glassy carbon (GC) RRDE with a platinum ring.

		$i_{d,\ theoretical}$			
Rotation speed (ω) (rpm)	**Rotation speed (rad/s)**	**(mA)**	**(mA/cm^2)**	**(mA)**	**(mA/cm^2)**
		5.61 mm GC disk		**5 mm GC disk**	
400	41.9	0.747	3.02	0.593	3.02
900	94.2	1.12	4.53	0.890	4.53
1600	168	1.49	6.04	1.19	6.04
2500	262	1.87	7.55	1.48	7.55

The kinetic current was calculated based on the Koutecky-Levich equation below using the cathodic sweep of the 1600 rpm ORR curve.

$$\frac{1}{i} = \frac{1}{i_k} + \frac{1}{i_d} \tag{4.5}$$

University of Cape Town

Where i is the measured current and i_d is the measured diffusion limiting current. The specific activity ($i_{k,\ spec}$) was then obtained by normalisation of the kinetic current ($i_{k\ (0.9\ V)}$) measured at 0.9 V vs. SHE/RHE, by the ECSA of platinum. The mass specific activity ($i_{k,\ mass\ (0.9\ V)}$) was obtained by the normalisation of the kinetic current measured at 0.9 V vs. SHE/RHE with the mass of platinum on the electrode surface.

Rotating ring disk electrode (RRDE) experiments were carried out in an oxygen saturated electrolyte solution. The disk and ring potentials were controlled by a bipotentiostat (Bio-logic Science Instruments). The ring was held at a potential of 1.2 V vs. SHE/RHE throughout the measurements, while the disk potential was swept from 1.2 to 0 V vs. SHE/RHE at 5 mV/s. The disk and ring currents were recorded as a function of the disk potential vs. SHE/RHE. The collection efficiency (N) of the ring was taken as 0.37 (Pine Instruments). Rotation speed was found to have a negligible effect on the collection efficiency (N) of the ring, therefore all RRDE experiments were carried out at one rotation speed, 1600 rpm(Antoine and Durand, 2000). The average number of electrons exchanged during the reduction of one O_2 molecule (equation 4.9.) was calculated by the charge (equations 4.6 and 4.7) and mass balances equations below (equation 4.8). The 2 electron and 4 electron disk currents are from the formation of H_2O_2 and H_2O on the disk respectively (Antoine and Durand, 2000).

$$i_{2e^-} = \frac{i_{Ring}}{N} \tag{4.6}$$

$$i_{Disk} = i_{2e^-} + i_{4e^-} \tag{4.7}$$

$$\frac{i_{Disk}}{n} = \frac{i_{2e^-}}{2} + \frac{i_{4e^-}}{4} \tag{4.8}$$

Thus

$$n = \left(\frac{4.\, i_{Disk}}{i_{Disk} + \frac{i_{Ring}}{N}} \right) \tag{4.9}$$

The ratio of one H_2O_2 molecule formed per O_2 reactant molecule was calculated according to the equation below.

University of Cape Town

$$X_{H_2O_2} = \frac{\frac{2i_{Ring}}{N}}{i_{Disk} + \frac{i_{Ring}}{N}} \quad (4.10)$$

Where N is the collection efficiency of the ring, i_{Ring} is the ring current and i_{Disk} is the disk current. The ratio $X_{H_2O_2}$ was plotted against the disk potential for each Pt loading for the sputtered model electrodes and the Wt% Pt for the MOCVD prepared catalysts.

4.3 Benchmarking experiments and reproducibility study

Electrochemical characterisation of two commercial carbon supported platinum catalysts using a GC-Pt RRDE (Pine Instruments, E7R9 Series) was performed to establish a benchmark reference point for all further electrochemical measurements and to verify the reproducibility of measurements performed using the electrochemical setup in this study. The commercial catalysts, catalyst 1 and catalyst 2 were taken through the two main electrochemical characterisation techniques, cyclic voltammetry and RDE measurements detailed in Section 4.2.3 and 4.2.5. The ECSA was calculated for both catalyst 1 and catalyst 2 and compared to the manufacturer specifications for each catalyst. RDE measurements were conducted primarily to confirm that the cell setup could achieve full oxygen saturation and this was evaluated by the comparison of the theoretical and experimental diffusion limiting currents.

4.4 Physical characterisation

The sputtered model electrodes and the MOCVD catalysts described above were analysed by the following physical characterisation techniques to gain a better understanding of the effects of increased platinum loading on parameters such as surface morphology and particle size.

4.4.1 Transmission electron microscopy (TEM) and Scanning transmission electron microscopy (STEM)

Transmission electron microscopy (TEM) measurements were carried out at a Tecnai G^2 electron microscope operating at 200 kV at the Electron Microscope Unit at the University of Cape Town. TEM was used to examine the platinum nanoparticle size and particle dispersion on the carbon support of the MOCVD prepared catalyst samples. MOCVD catalyst samples were mixed with a small amount of acetone (5 mL) and ultrasonicated for approximately 15 minutes before adding a small drop of the solution to a copper grid. The copper grid was placed under a lamp for a few seconds until the acetone had evaporated. The sample was then analysed in the TEM.

University of Cape Town

A similar preparation procedure was followed to prepare samples for scanning transmission electron microscopy (STEM) analysis. STEM analysis of the MOCVD samples was carried out at the electron microscope unit at the University of the Western Cape (UWC) in Cape Town. STEM was used to observe the extent of particle agglomeration and particle size through realistic 3D images.

Energy dispersive X-rays (EDX) and scanning electron microscopy (SEM) were used at the Paul Scherrer Institute (PSI) to examine the sputtered platinum electrode surfaces. EDX mapping was used in addition to the conventional SEM images to create a picture of the elemental distribution on the electrode surfaces. In this case the two elements of interest were carbon and platinum.

4.4.2 **X-ray diffraction (XRD)**

X-ray diffraction (XRD) using a Siemens D8 Advance diffractometer with a Co K_α radiation source operating at 40 kV was used to determine the average platinum crystallite size by employing the Scherrer equation below.

$$< L >= \frac{K\lambda}{\beta cos\Theta} \tag{4.11}$$

Where:

<L> is a measure for the dimension of the particle in the direction perpendicular to the reflecting plane

K- Dimensionless shape factor approximately equal to 1

λ is the X-ray wavelength

β is the peak width

Θ is the angle between the beam and the normal on the reflecting plane

4.4.3 **Thermogravimetric analysis (TGA)**

Thermogravimetric analysis using a *METTLER TGA/sDTA851e Thermogravimetric Analyser,* was used to verify the wt% Pt present in the MOCVD prepared catalysts. A sample of catalyst was transferred to a small crucible which did not have a lid and oxidised by a 10 mL/min flow of air, as the temperature was ramped from 25 to 850 °C at 10/min. Only solid material that was not oxidised by air, remained in the crucible at the end of the TGA. The results obtained were compared to the expected platinum content listed in Table 4.2.

University of Cape Town

5. RESULTS AND DISCUSSION

Section 5 details the electrochemical and physical characterisation results of this study. Section 5.1 covers the benchmarking section, whereby two commercial 40 wt.% Pt/C catalysts were characterised using the electrochemical setup described in Section 4, to show the reader that the system is working correctly and the results presented herein are reliable and reproducible. Section 5.3 details the results collected for the electrochemical and physical characterisation of the sputtered model electrode system developed at the Paul Scherrer Institute. Section 5.4 covers the results obtained for the MOCVD prepared catalysts with varying weight percentages of platinum (20, 40, 60 and 80 wt.% Pt) prepared at the University of Cape Town. Finally a comparison and summary of the mains findings from the two catalysts systems is reported.

The results obtained from the sputtered model electrode system and the MOCVD prepared catalysts were not directly comparable in terms of ECSA. This can be explained in large part by the differences in the preparation methods for each catalyst system. As such two theoretical models based on simplified assumptions of an idealised sputtered electrode and an idealised electrode prepared by MOCVD was developed to compare the experimentally determined ECSA values (see Sections 5.3 and 5.4).

University of Cape Town

5.1 Benchmarking

Benchmarking experiments were carried out on two commercial 40 wt.% Pt/C catalysts using a RRDE (Pine Instruments, E7R9 Series). The following results are presented in Figure 5.1.

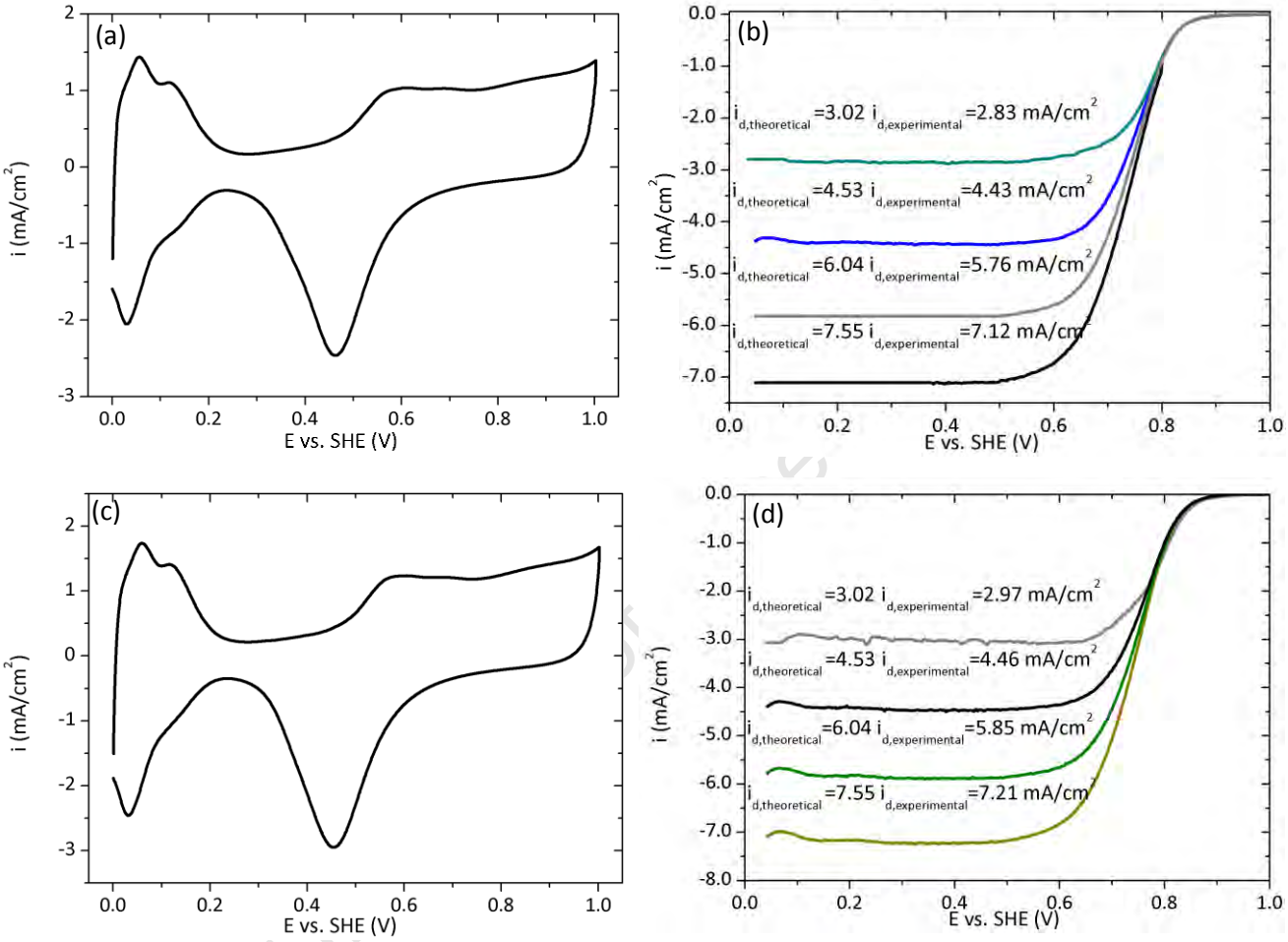

Figure 5.1 : Cyclic voltammograms carried out in an Ar saturated 0.1 M $HClO_4$ solution at room temperature, sweep rate 50 mV/s for two different commercial catalysts (a) catalyst 1 and (c) catalyst 2. Oxygen reduction current densities for cathodic sweeps (5 mV/s, 1600 rpm) in oxygen saturated 0.1 M $HClO_4$ solution at room temperature for (b) catalyst 1 and (d) catalyst 2 illustrating the experimental and theoretical diffusion limiting currents.

The oxygen reduction diffusion limiting currents lie within a reasonable range relative to the theoretical diffusion limiting currents for both catalyst 1 and catalyst 2. This indicates good oxygen saturation of the electrochemical cell setup and hence reliability of results obtained from this specific system. Table 5.1 below summarises the ECSA results from the benchmarking experiments compared to the commercial catalyst specifications.

Table 5.1 : Comparison of experimental and specification ECSA for catalyst 1 and catalyst 2

Commercial Catalyst	wt.% Pt	$ECSA_{Experimental}$ (m^2_{Pt}/g_{Pt})	$ECSA_{specification}$ (m^2_{Pt}/g_{Pt})
Catalyst 1	40	67	68
Catalyst 2	40	72	86

The ECSA values calculated experimentally are within a reasonable range of the commercial catalyst specifications and as such this is a further indication of the reliability of the electrochemical setup used in this study.

5.2 TGA analysis of platinum acetylacetonate

The thermoGravimetric analysis carried out on a $Pt(acac)_2$ sample in a nitrogen gas environment yielded the following curve in Figure 5.2 below. TGA was carried out to get an estimation of the decomposition window of $Pt(acac)_2$ to determine the operating conditions of the furnace used to produce the MOCVD catalysts.

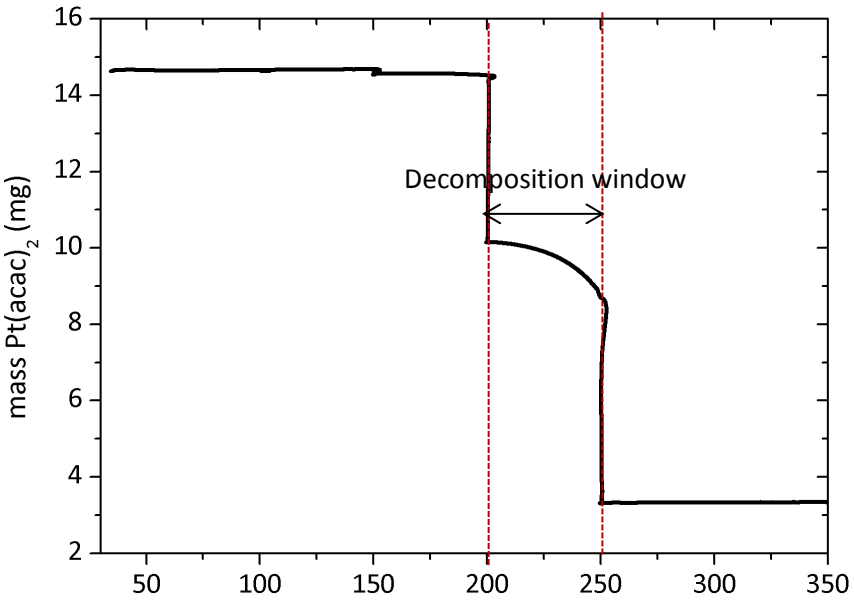

Figure 5.2 : TGA curve illustrating the decomposition temperature window for $Pt(acac)_2$

The TGA curve gives a clear indication of the decomposition window of $Pt(acac)_2$. The most significant mass loss occurs between 200 and 250 °C, after a temperature of 250 °C only platinum metal is left in the sample crucible and the organic part of the $Pt(acac)_2$ molecule has been vaporised. These findings are in line with the decomposition temperature of $Pt(acac)_2$ found in the literature (Battiston *et al.*, 2005). This gives an estimate of the temperature at which to run the furnace used for metal-organic chemical vapour deposition (MOCVD) of $Pt(acac)_2$ onto a carbon substrate under an inert gas environment (argon was used in this study).

5.3 Sputtered model electrodes

Section 5.3 details the results of the model system developed by sputtering a range of Pt loadings 2, 10, 20, 50 and 100 μg/cm^2 onto a carbon black thin film (Vulcan XC72R) deposited onto a glassy carbon disk electrode (See Section 4.1.1). The model electrodes were developed to gain a better understanding of the effects of increasing platinum loading on particle size, surface morphology and subsequently the ECSA and activity of the catalyst itself. The effects of increased platinum loading were visualised through SEM and EDX mapping images shown in Section 5.3.1 below. Electrochemical testing of the model electrodes was carried out to observe the differences in ECSA via two different methods, namely cyclic voltammetry by the H_{upd} method and CO stripping voltammetry (Section 5.3.2). The extent of Pt agglomeration with increased Pt loading could also be observed by these methods. The ORR activity of the model electrodes was determined by RRDE measurements and these results are shown in Section 5.3.4, the degree of undesired H_2O_2 formation was also measured as a function of platinum loading.

A theoretical, idealised sputtered electrode model was developed based on the actual sputtering method with various simplifying assumptions. Figure 5.3 below illustrates how the platinum particles are distributed over the surface of the carbon thin film deposited on the electrode.

Cape Town

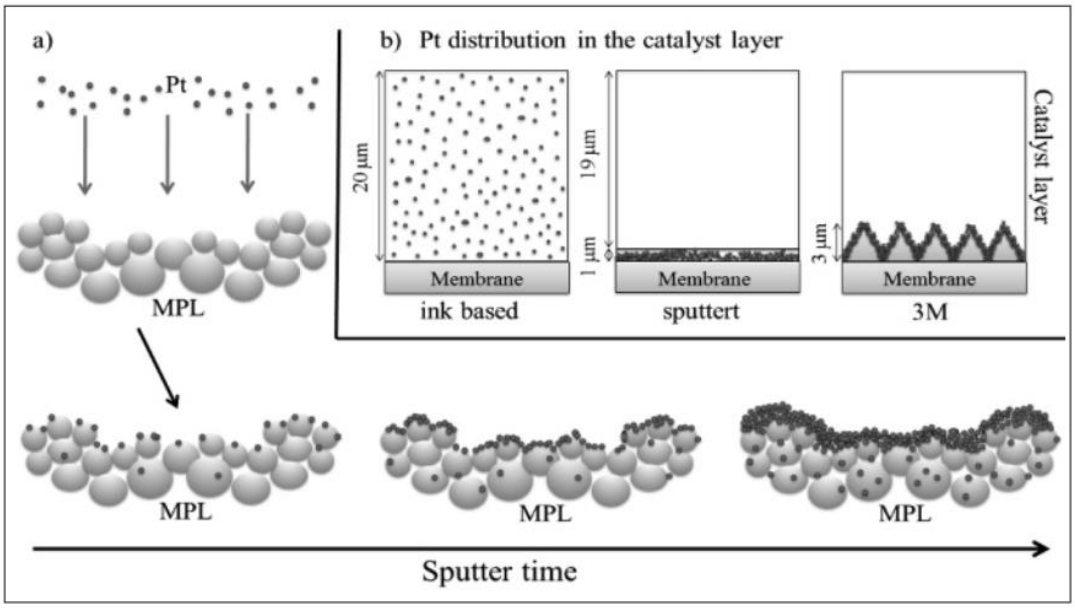

Figure 5.3 : (a) Scheme of the platinum sputtering process on a microporous carbon layer with time, (b) Pt distribution in the catalyst layer of an ink-based, a sputtered and a 3M electrode (Schwanitz *et al.*, 2012).

Figure 5.3 illustrates how the platinum is essentially deposited only on the surface carbon particles, with a small fraction of platinum particles penetrating deeper into the carbon film. An ideal theoretical model

illustrating the effects of increased platinum loading on a Vulcan XC72R substrate was developed for the sputter deposited platinum electrodes. The following assumptions were made for the ideal theoretical model system.

- Platinum and carbon particles are perfects spheres with diameters of 2 nm and 40 nm respectively.
- Platinum particle size remains constant as platinum loading increases.
- Platinum particles are only deposited on the surface layer of carbon particles.
- Platinum particles are homogenously dispersed
- Platinum utilisation is 100%
- Surface roughness factor of platinum was assumed to be 1.8 (conservative estimate)
- 50% of the carbon surface is available for platinum deposition.

Based on these assumptions the idealised sputtered model electrode was developed and subsequently used to determine the ECSA at the same platinum loadings used in the experimental system. Figure 5.4 below illustrates the simplified sputtered electrode system.

University of Cape Town

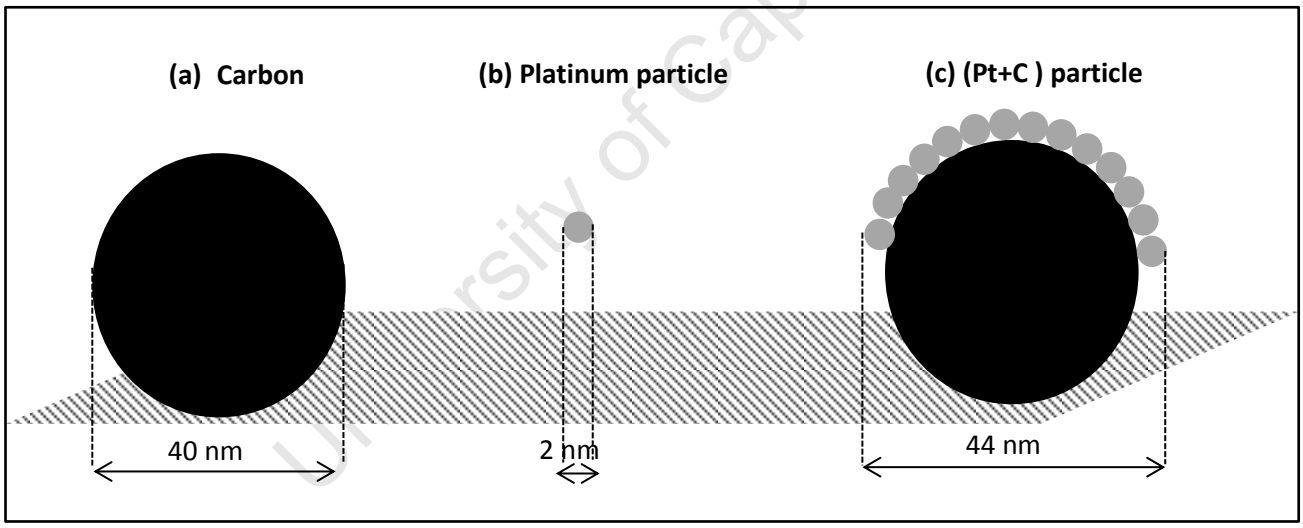

Figure 5.4 : Illustration of (a) carbon particle diameter, (b) Platinum particle diameter and (c) overall diameter of a single carbon particle with a 2 nm platinum film.

Table 5.2 below summarises the physical properties of a single carbon particle and a single platinum particle with the dimensions illustrated in Figure 5.4 above.

Table 5.2 : Physical properties of a single carbon particle and a single platinum particle

Property	units	Symbol	Formula	Value
Carbon particle				
diameter	cm	d_c	-	0.000004
radius	cm	r_c	-	0.000002
Surface area	cm^2	SA_c	$SA_c = 4.\pi.r_c^2$	5.03×10^{-11}
Cross-sectional	cm^2	XA_c	$XA_c = \pi.r_c^2$	1.26×10^{-11}
volume	cm^3	V_c	$V_c = \frac{4}{3}.\pi.r_c^3$	3.35×10^{-17}
Platinum particle				
diameter	cm	d_{Pt}	-	0.0000002
radius	cm	r_{Pt}	-	0.0000002
density	g/cm^3	P_{Pt}	-	21.46

Table 5.3 below summarises the physical properties and formulas used to calculate the required information for a single carbon particle with 50 % of its surface covered by a complete 2 nm platinum film.

Table 5.3 Summary of physical properties and formulas used for a single carbon particle covered by a 2 nm thick platinum film

Property	units	Symbol	Formula	Value
Platinum film +carbon particle				
Diameter Pt + Carbon	cm	$d_{(Pt+C)}$	$d_{(Pt+C)} = 2.d_{Pt} + d_c$	0.0000044
Radius Pt + Cabon	cm	$r_{(Pt+C)}$		0.0000022
Pt surface roughness factor	-	rf	-	1.8
Volume Pt + Carbon	cm	$V_{(Pt+C)}$	$V_{(Pt+C)} = \frac{4}{3}.\pi.r_{(Pt+C)}^3$	4.46×10^{-17}
Surface area platinum film	cm	$SA_{Pt\ film}$	$SA_{Pt} = rf.4.\pi.r_{(Pt+C)}^2$	$1.09 \times^{-10}$
Volume platinum film	cm^3	$V_{Pt\ film}$	$V_{Pt\ film} = V_{(Pt+C)} - V_c$	1.11×10^{-17}
Electrode diameter	cm	d_E	-	0.50
Electrode radius	cm	r_E	-	0.25
Electrode Surface area	cm^2	A_E	$A_E = \pi.r_E^2$	0.196
Number carbon particles	-	n_c	$n_c = \frac{SA_E}{XA_c}$	1.56×10^{10}

Figure 5.5 below illustrates the overall idealised model system used to calculate the ECSA for the sputtered electrodes. A monolayer of carbon particles with diameters of 40 nm deposited onto the surface of a glassy carbon electrode disk with a diameter of 5 mm, is covered with a 2 nm thick film of platinum on 50 % of the carbon particle surface.

University of Cape Town

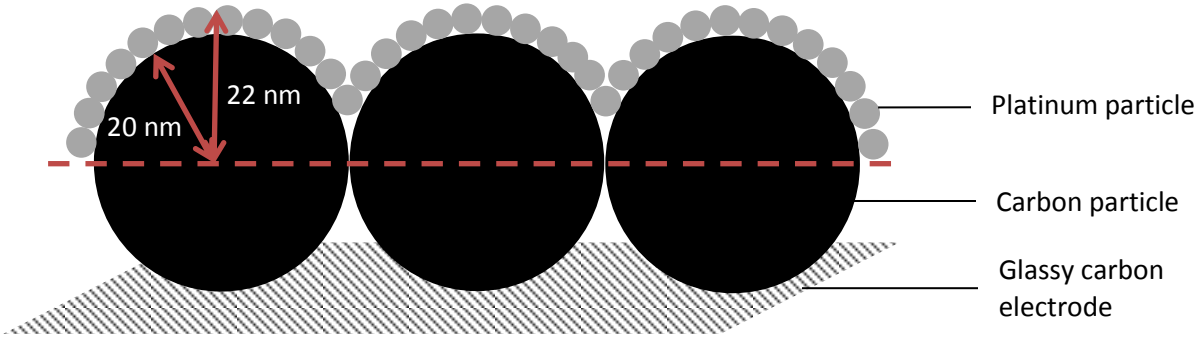

Figure 5.5 : Ideal model system for sputtered model electrodes. Illustrating a single layer of platinum nanoparticles deposited on spherical carbon particles deposited on a glassy carbon electrode surface

Table 5.4 summarises the overall calculations used to determine the ECSA of an idealised sputtered electrode.

Table 5.4 Summary of variables used to calculate the model Pt loading and ECSA

Property	units	Symbol	Formula	Value
Pt particles supported on a monolayer of carbon on glassy carbon electrode				
% carbon surface available	%	a	-	50
Total carbon surface area	cm^2	$SA_{c,total}$	$SA_{C,total} = a.n_c.SA_c$	7.85×10^{-01}
Total platinum surface area	cm^2	$SA_{Pt,\ total}$	$SA_{Pt,total} = n_c.SA_{(Pt+C)}$	8.55×10^{-01}
Total platinum volume	cm^3	$V_{Pt,\ total}$	$V_{Pt,total} = n_c(V_{(Pt+C)}$	1.73×10^{-07}
Total mass platinum on electrode	g	$m_{Pt,\ total}$	$m_{Pt,total} = V_{Pt,total} \cdot \rho_{Pt}$	3.72×10^{-06}
Mass platinum per electrode area	$\mu g/cm^2$	$m_{Pt,loading}$	$m_{Pt,loading} = \frac{m_{Pt,total}}{SA_E}$	18.9
ECSA	cm^2_{Pt}/cm^2	ECSA	$ECSA = \frac{SA_{Pt,total}}{SA_E}$	4.36

The calculations above assume a 50% availability of the carbon surface, which is completely covered by platinum. Therefore the model predicts a continuous platinum surface with a film thickness of 2 nm at a platinum loading of 18.9 $\mu g/cm^2$. This platinum loading corresponds to an ECSA of 4.36 cm^2_{Pt}/cm^2. These values were used as the basis for calculation of the idealised sputtered electrode system, Table 5.5 below summarises the results for the theoretical ECSA calculated from the idealised sputtered electrode system versus the experimentally determined ECSA determined by the H_{upd} method.

University of Cape Town

Table 5.5 Ideal CSA and experimental ECAS for each sputtered platinum loading

Pt loading (μg/cm^2)	Ideal ECSA (cm$^2_{Pt}$/cm^2)	Expt ECSA$_{Hupd}$ (cm$^2_{Pt}$/cm^2)
2	0.46	1.20
10	2.3	1.70
20	4.6	4.25
50	11.5	8.00
100	23	12.6

The theoretically calculated ECSA values correspond reasonably to the experimental values at low Pt loadings, however as Pt loading is increased beyond 20 μg/cm^2 the theoretical ECSA values are significantly higher than the experimental values. This is discussed in more detail in Section 5.3.3.

University of Cape Town

5.3.1 **Surface morphology - EDX mapping and SEM images**

The SEM and EDX mapping images presented below in Figure 5.6, illustrate the morphology of the model electrode surfaces and the carbon and Pt signals as the Pt loading is increased from 2 to 50 µg/cm^2.

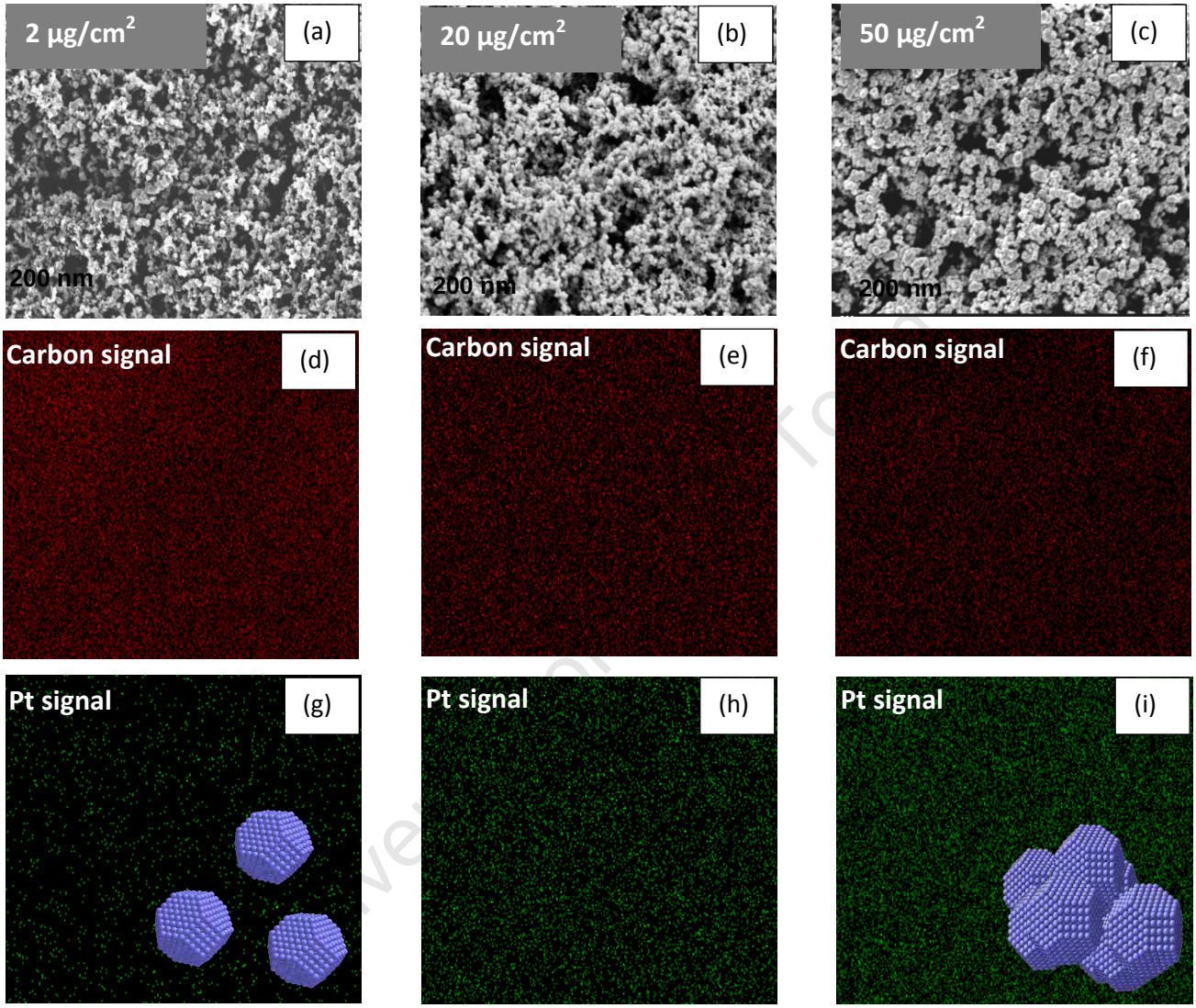

Figure 5.6 : SEM images and EDX mapping micrographs of 2, 20 and 50 µg/cm^2 sputtered model electrode surfaces. (a), (b) and (c) illustrates the SEM images of the electrode surfaces respectively. (d), (e) and (f) illustrate the carbon signal and (g), (h) and (i) illustrate the Pt signal measured for the respective Pt loadings. The blue hexagonal shapes are showing the progression from isolated particles to agglomerates as Pt loading increases.

The SEM images above show an increase in the amount of Pt on the Vulcan surface, indicated by the increase in the density of the white regions in the SEM image. The intense white colour in certain regions of the 50 g/cm^2 might indicate particle agglomeration. The EDX mapping images clearly indicate the increase in platinum (Figure 5.6 (g), (h) and (i)) by the increasing density of green dots. The subsequent decrease in carbon is illustrated by the decrease in density of red dots in Figure 5.6 (d), (e) and (f). It is clear from the

images that by varying the Pt loading between the said values, one can obtain discrete and agglomerated particles.

5.3.2 **ECSA of sputtered model electrodes**

The ECSA for the model electrodes was determined using the H_{upd} method and CO stripping (see Section 2.7.1). The cyclic voltammograms for the model electrodes are illustrated below in Figure 5.7.

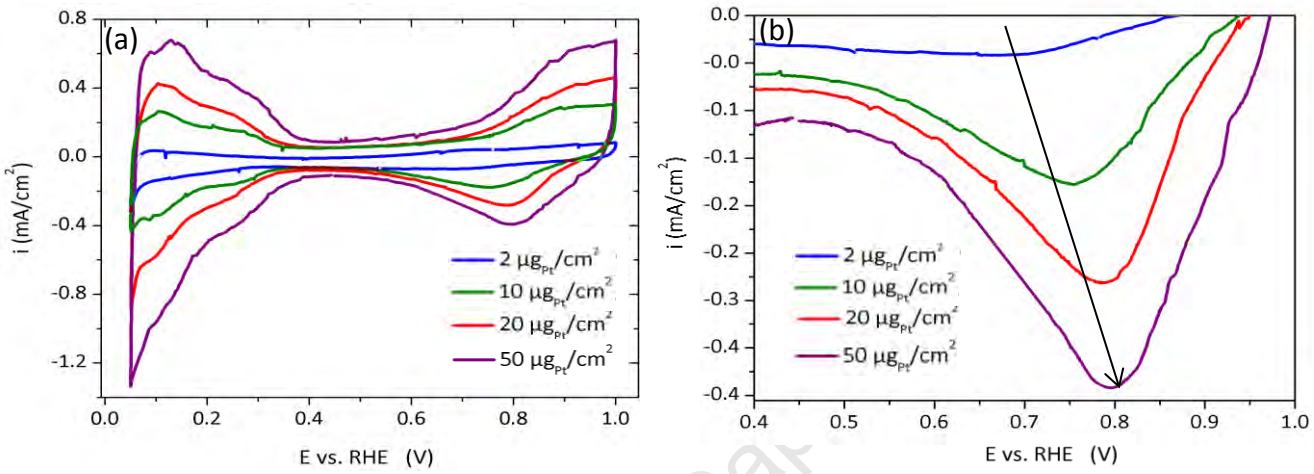

Figure 5.7 : Cyclic voltammograms carried out in an Ar saturated 0.1 M $HClO_4$ solution at room temperature, sweep rate 50 mV/s for different Pt loadings. (a) Comparison of CV's for different Pt loadings from 2 to 50 µg/cm^2. (b) Comparison of oxide reduction peaks for different Pt loadings.

The cyclic voltammograms show an increase in the H_{upd} area with increased Pt loading as expected. An interesting feature of the cyclic voltammograms is the oxide reduction peak observed on the reverse sweep from 1.0 V to 0 V vs. RHE, see Figure 5.7 (b). As the Pt loading increases from 2 to 50 µg/cm^2, the reduction peak shifts to more positive potentials, from 0.71 V to 0.79 V vs. RHE. It was proposed by Mayrhofer *et al.* (2009) that the oxophilicity of Pt nanoparticles increases as particle size decreases. It can thus be inferred from this that a more negative oxygen reduction potential indicates a stronger bond of an oxygen species to the Pt surface, which in turn indicates the presence of small Pt particles in the range of 2 – 3 nm. Thus the shifting oxide reduction peak to more positive potentials with increased Pt loading shown here, is an indication of a weaker oxide bond to the platinum surface, and subsequently indicates an increase in particle size as Pt loading increases from 2 to 50 µg/cm^2. This finding is significant as it is an indication of particle agglomeration as Pt loading increases. Pt agglomerates and isolated Pt nanoparticles have different surface properties towards the ORR(Kinoshita, 1990), this effect can be seen in the ORR results in Section 5.3.4.

The alternative method used to calculate the ECSA for the sputtered model electrodes was CO stripping. The CO stripping voltammograms of the 100 µg/cm^2 model electrode is presented below in Figure 5.8 (a). Figure 5.8 (b) illustrates the shift in the CO oxidation peak to more negative values as the Pt loading is increased from 2 to 100 µg/cm^2.

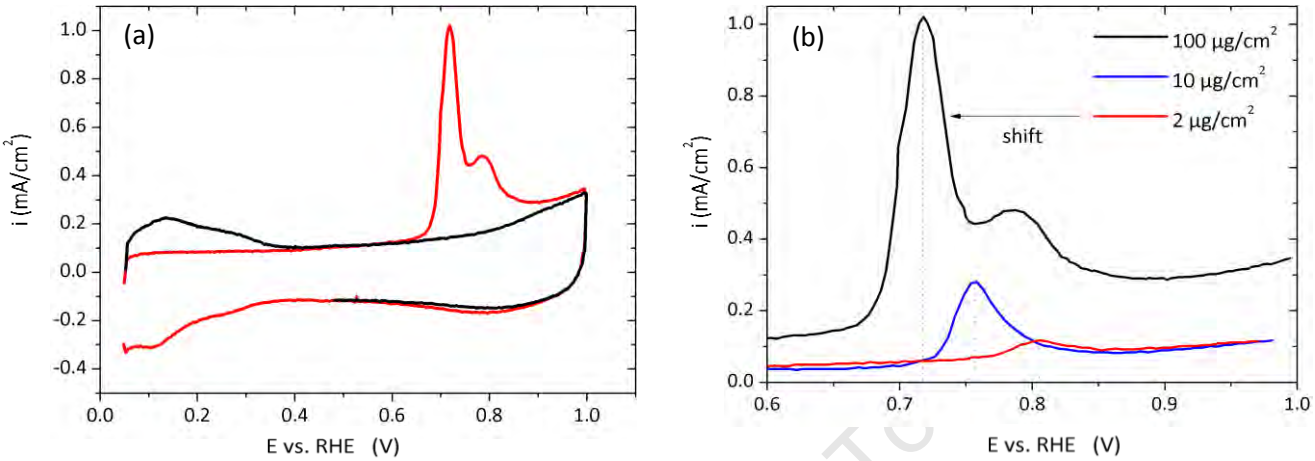

Figure 5.8 : (a) CO stripping voltammogram in an Ar saturated 0.1 M $HClO_4$ solution at a sweep rate of 20 mV/s for 100 g/cm^2 sputtered model electrode, at room temperature. Sweep 1 is indicated by the red curve and pertains to the CO oxidation sweep and sweep 2 indicates the CV after all CO has been oxidised off the Pt surface. (b) CO oxidation peaks for sputtered model electrodes with Pt loadings of 2, 10 and 100 µg/cm^2.

The red line in Figure 5.8 (a) indicates the first voltammeric sweep in a CO-free electrolyte, after CO has been adsorbed onto the Pt surface. The black line indicates the second sweep after all the CO has been oxidised off the Pt surface, and is essentially a typical cyclic voltammogram associated with a Pt supported catalyst. According to literature the CO oxidation peak occurs between 0.76 and 0.95 V vs. RHE (Maillard *et al.,* 2005) An interesting feature of the CO stripping voltammogram is the double voltammeric peak observed for the 100 µg/cm^2 sample. Maillard *et al.* (2005) attributed this double peak to the presence of Pt agglomerates as well as isolated Pt particles. The peak occurring at a lower potential, indicates the presence of Pt agglomerates an the the peak occurring at a higher potential, indicates the presence of isolated Pt nanoparticles. This result is significant as it again indicates the presence of Pt agglomerates in the higher Pt loading model electrodes.

Figure 5.8 (b) illustrates the peak potentials for CO oxidation for the 2, 10 and 100 µg/cm^2 model electrodes. The 2 µg/cm^2 electrode with the lowest Pt loading has a CO oxidation potential which occurs at a more positive potential compared to the 10 and 100 µg/cm^2 electrodes. It is noted that the peak potential of CO oxidation shifts to more negative values as the Pt loading increases from 2 to 100 µg/cm^2, i.e. from isolated Pt nanoparticles to a combination of isolated nanoparticles and Pt agglomerates (Maillard *et al.,* 2005). This result supports the findings in Section 5.2.2. , which indicates the presence of Pt agglomerates at higher Pt

loadings (50 and 100 µg/cm^2). The effect of these Pt agglomerates on the electrochemical behaviour of the catalyst will be analysed in the following sections.

5.3.3 Trends between ECSA and Pt loading

Figure 5.9 (a) below depicts the theoretical and experimental trends between Pt loading and ECSA measured by the H_{upd} method.

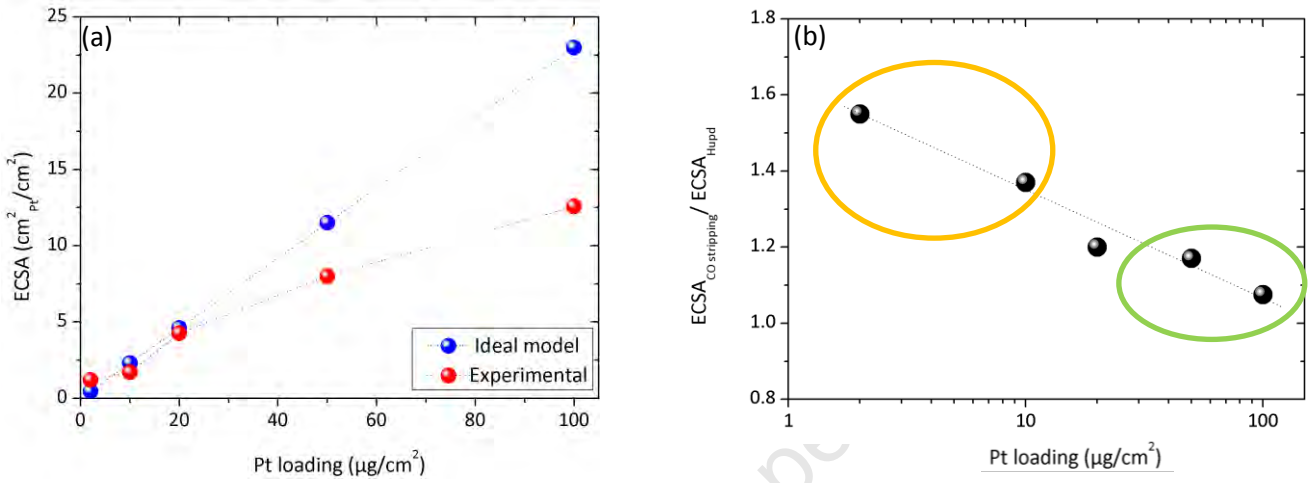

Figure 5.9 : (a) ECSA versus Pt loading, comparison of expected theoretical trend (blue) and actual experimental trend (red). (b) comparison of ECSA determined by CO stripping as a ratio of ECSA determined by the H_{upd} method, plotted as a function of Pt loading, the green circle highlights the ratio approximately equal to one for the low loading samples and the orange circle indicates a ratio approximately equal to 1.4 for the higher Pt loading samples.

In an ideal, homogenously dispersed catalyst system, containing only isolated nanoparticles, the ECSA would increase linearly with Pt loading, assuming 100 % catalyst utilisation (Schwantiz *et al*., 2012), see Figure 5.9 (a) blue curve. However, in a real supported catalyst system, particle agglomeration occurs at higher Pt loadings, which accounts for the non-linear relationship seen by the red curve in Figure 5.9 (a). The ideal model does not account for the platinum particles that have penetrated the carbon film beyond the surface layer of carbon particles. However it is assumed that this is a negligible amount of platinum. At higher platinum loadings the experimental curve begins to plateau and is below the ideal curve. This can be explained by particle agglomeration, as the platinum loading is increased the particles encroach on the sphere of influence of each other and they agglomerate (Nesselberger *et al.*, 2013). Agglomeration increases the average particle size and in turn reduces the overall active area of platinum. The experimental curve plateauing at higher loadings is in line with what one would expect, as the platinum loading is increased beyond a certain point, the platinum particles are effectively being deposited on top of each other, thus causing little difference to the available active platinum surface. The ideal model does not account for particle agglomeration and hence at high Pt loadings the ECSA is considerably higher than what is observed

in reality. It is interesting to note that at low platinum loadings the ideal model and the experimental curves overlap, because at low Pt loadings there are isolated platinum nanoparticles and negligible agglomeration, and hence the ideal model corresponds well to the experimental results.

Figure 5.9 (b) illustrates the trend between the ratio of the ECSA calculated by CO stripping and the ECSA calculated by the H_{upd} method with increasing Pt loading. This was done in order to establish a comparison between the two ECSA calculation methods. Mayrhofer *et al*. (2005) found that the surface area determined by CO stripping is typically 1.4 times greater than that obtained by the H_{upd} method for high surface area supported platinum catalysts, and the difference was thought to be due to the significant contribution of the capacity of the carbon support material. At low Pt loadings the carbon support contribution to the double layer charge is significant, as seen in the cyclic volatmmogram for the 2 µg/cm^2 electrode Figure 5.7 (a), where it is difficult to distinguish between the H_{upd} area and the double layer as the double layer is very large and as such interferes with the accuracy of calculation of the H_{upd} area. In this study a similar trend to that observed by Mayrhofer *et al.* (2005) was seen for the low loading sputtered model electrodes (2 and 10 µg/cm^2), where the carbon support exposure is greater than that of the high Pt loading sputtered electrodes. It was observed that the CO stripping ECSA was between 1.4 and 1.6 times greater than that calculated by the H_{upd} method, see Figure 5.9 (b) orange circle. This was attributed to the inaccuracies associated with the H_{upd} charge calculation as the double layer contribution was so large. However, as the Pt loading increased, the difference between the ECSA calculated by the two different methods decreased. At the high Pt loadings, (50 and 100 µg/cm^2) the two methods obtained comparable results for the ECSA of Pt, indicated on the graph by the green circle highlighting a $ECSA_{CO\ stripping}/ECSA_{Hupd}$ ratio approximately equal to 1. This can be accounted for by the reduced carbon support contribution at high loadings and hence a more accurate H_{upd} area calculation.

5.3.4 **Electrocatalytic activity of sputtered model electrodes**

The electrocatalytic activity of the sputtered model electrodes towards the ORR was determined by RDE measurements at 1600 rpm, Figure 5.10 (a). The resulting tafel plots in Figure 5.10 (b) were used to extract the kinetic current densities (i_k) for each Pt loading at 0.9 V vs. RHE, i.e. no mass transfer contributions. Figures 5.10 (c) and (d) represent the mass and specific activities respectively plotted versus potential (V).

University of Cape Town

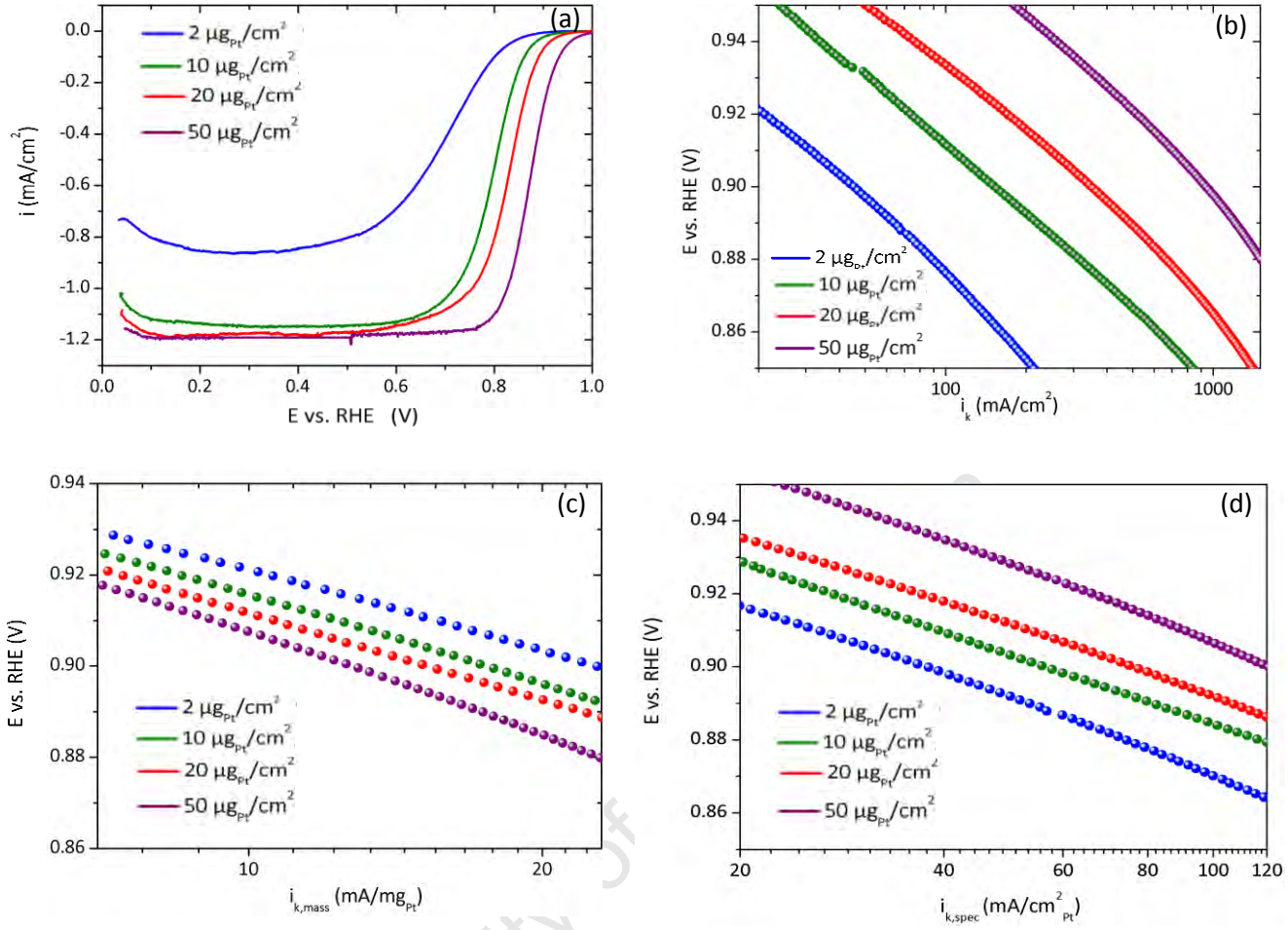

Figure 5.10 : (a) Oxygen reduction current densities for cathodic sweeps (5 mV/s, 1600 rpm) in oxygen saturated 0.1 M $HClO_4$ solution at room temperature for sputtered model electrodes with different loadings (b) oxygen reduction tafel plot showing mass transport corrected current densities (i_k) for the ORR on the different sputtered model electrodes, obtained from the cathodic sweeps (5 mV/s, 1600 rpm) in an oxygen saturated 0.1 M $HClO_4$ solution (log i_k versus potential). (c) Comparison of oxygen reduction (a) mass activity ($i_{K,\,mass}$) and (b) surface specific activity ($i_{K,\,spec}$) of sputtered model electrodes with different Pt loadings at room temperature, current densities measured at a constant potential of 0.9 V vs. RHE, indicated by the horizontal line at 0.9 V vs. RHE on (c) and (d).

The theoretical limiting current of 1.19 mA/cm^2 for the ORR at 1600 rpm is not reached for the 2 and 10 μg/cm^2 sputtered model electrodes, see Figure 5.10 (a). This could be due to the fact that the 2 μg/cm^2 sample contains the smallest Pt nanoparticles. It has been suggested that small Pt nanoparticles, with an abundance of edge and corner sites according to the cubo-octahedral model by Kinoshita (1989), promote peroxide formation, thus reducing ORR current observed(Inaba, 2004). If this is so, the reduced limiting current for the 2 μg/cm^2 sample can be explained in terms of an increased H_2O_2 formation. H_2O_2 formation is a 2 electron process, and is formed by a series pathway described in Section 2.3.1. The theoretical limiting current calculated for the direct 4 electron process for the ORR, will inevitably not be reached if H_2O_2 species are formed as a final product of reaction. These observations regarding limiting current and peroxide formation will be further discussed in Section 5.3.5, where RRDE results are presented.

Figure 5.10 (b) shows the tafel slopes plotted for each Pt loading. The kinetic current density (i_k) is seen to increase logarithmically as Pt loading increases. This can be attributed to the increase in available active surface area of platinum (ECSA) for the ORR reaction. The mass normalised current density ($i_{k,mass}$) is depicted in Figure 5.10 (c) and the specific surface area normalised current density ($i_{k,spec}$) is depicted in Figure 5.10 (d), both plotted against potential. The plots were used to extract the mass and specific activities at 0.9 V vs. RHE and are plott ed versus platinum loading in Figure 5.11.

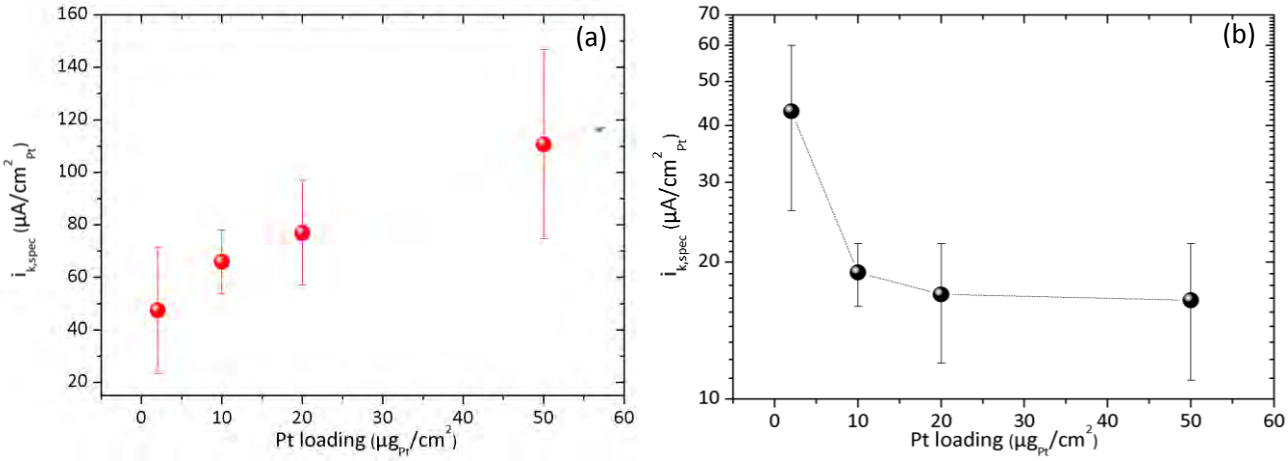

Figure 5.11 : Comparison of (a) surface specific and (b) mass activity for the oxygen reduction reaction measured at 0.9 V vs. RHE for sputtered model electrodes with different Pt loadings

Assuming identical reaction kinetics and surface properties of the different Pt loadings, one would expect the $i_{K,\ spec}$ to remain constant independent of Pt loading. However, Figure 5.11 (b) indicates an increase in $i_{k,\ spec}$ with Pt loading. In a study by Gasteiger *et al*. (2005) that $i_{k,\ spec}$ increased as Pt particle size increased from Pt nanoparticles (2-6 nm) to Pt-black type particles (10-20 nm) to extended Pt surfaces(Gasteiger *et al.*, 2005). This $i_{k,spec}$ increase was attributed to the decrease in the active platinum surface area per gram of catalyst as the Pt particle size increased, the so called particle size effect. Particle size increase with Pt loading was due to the particles agglomerating, thus decreasing the overall active Pt surface per mass of catalyst. Mayrhofer *et al.* (2008) also proposed that the surface coverage of adsorbed OH species is greater on small nanoparticles than on larger particles owing to the higher oxophilicity of small nanoparticles compared to larger particles. The adsorbed OH species effectively block the Pt active sites for the ORR, and hence reduce the overall activity of the catalyst. Thus as particle size increases, OH adsorption decreases and there are more Pt active sites available for ORR, hence $i_{k,\ spec}$ increases. Figure 5.11 (b) shows a decrease in mass specific activity $i_{k,\ mass}$, with Pt loading as expected, and also reflects the decreasing surface area per mass of catalyst with Pt loading.

5.3.5 **RRDE results – Hydrogen peroxide formation**

RRDE experiments were employed to determine the extent of hydrogen peroxide formation on the surface of each of the sputtered model electrodes during the oxygen reduction reaction Figure 5.12 below illustrates the RRDE curves obtained for the Pt loadings 2, 10, 20 and 50 µg/cm^2. The red curve indicates the ring current produced by H_2O_2 oxidation, while the blue curve indicates the disk current produced by oxygen reduction via a combination of the 4-electron and the 2-electron reduction mechanisms.

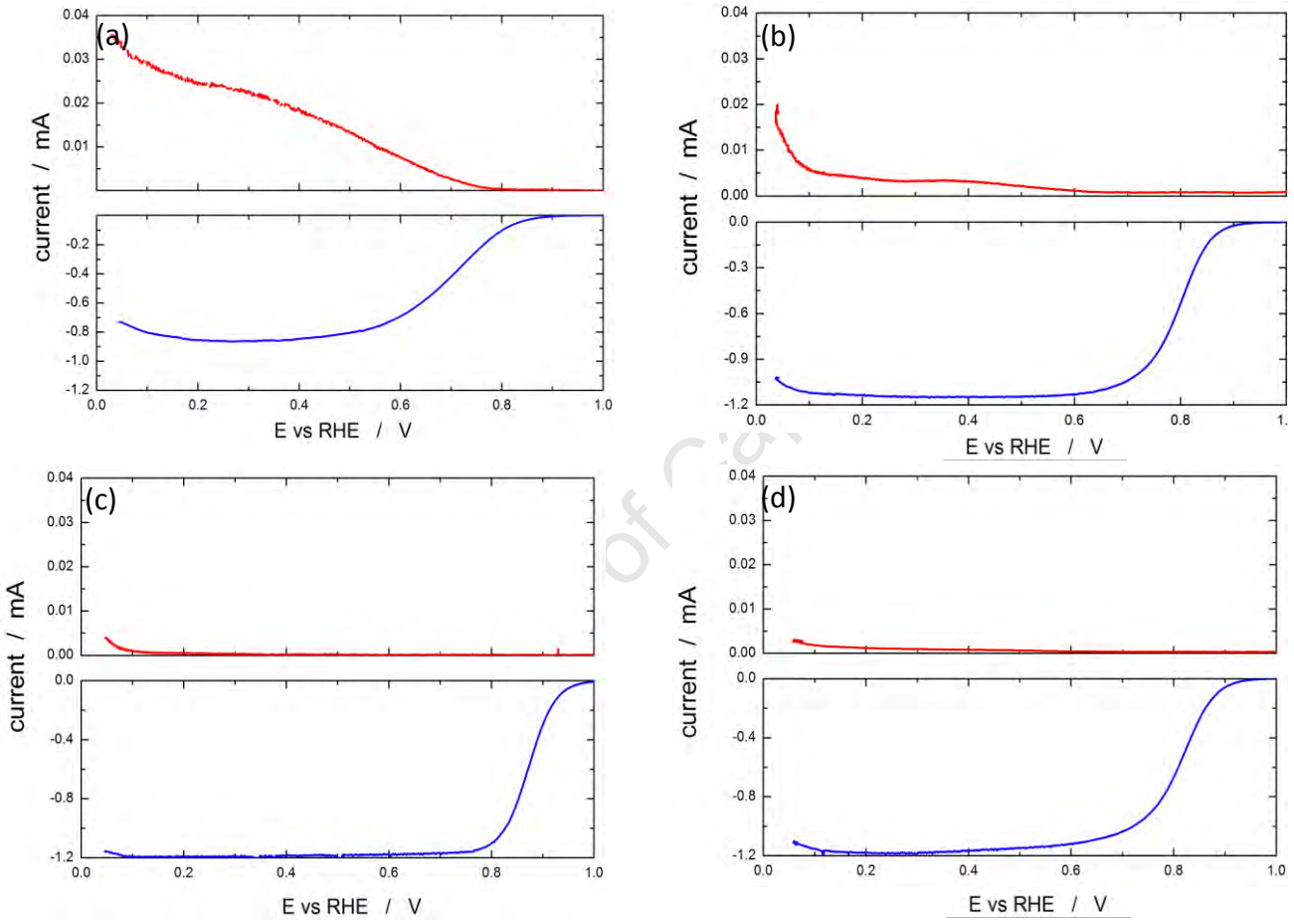

Figure 5.12 : Hydrodynamic voltammograms for oxygen reduction in an oxygen saturated, 0.1 M solution $HClO_4$ at room temperature. Disk electrode: sputtered model electrodes with different loadings deposited on a glassy carbon disk, Ring electrode: Pt. Rotation speed 1600 rpm. Red line indicates current produced as a result of H_2O_2 formation and blue line indicates ORR current for (a) 2 µg/cm^2 (b) 10 µg/cm^2 (c) 20 µg/cm^2 (d) 50 µg/cm^2 sputtered model electrodes.

It is evident from the ring curves in Figure 5.12 that a certain amount of peroxide species are produced all the different loading samples below 0.8 V vs. RHE. Furthermore it is apparent that there are large differences between the relative amounts of hydrogen peroxide produced on each sample, with the most significant amount of hydrogen peroxide being observed on the low loading samples. To further investigate these findings the graphs in Figure 5.13 below were plotted to illustrate the yield of H_2O_2 formed (%H_2O_2) at different Pt loadings (Figure 5.13 (a)) and potentials (Figure 5.13 (b)).

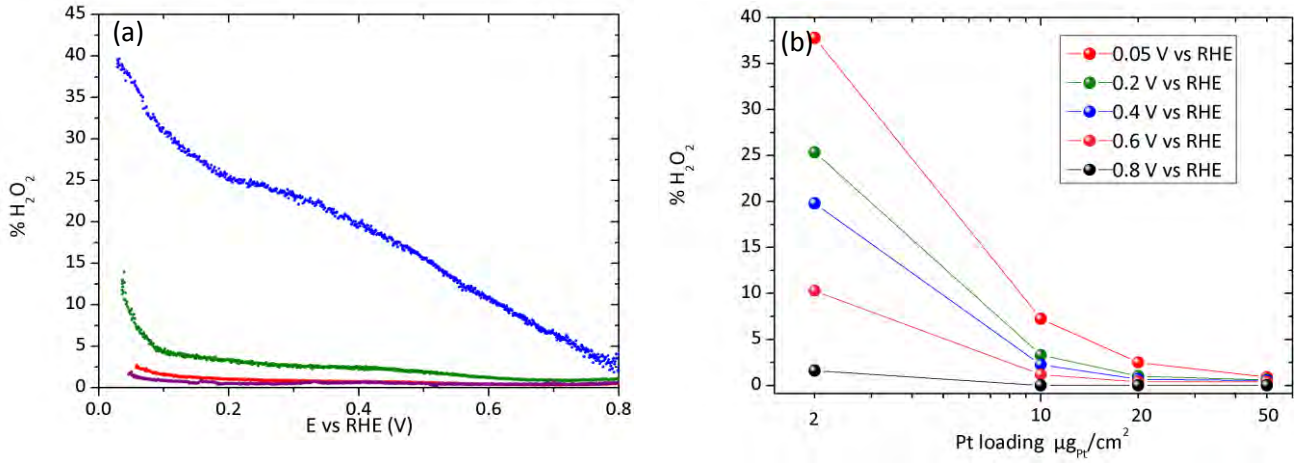

Figure 5.13 : H_2O_2 yields for oxygen reduction in an oxygen saturated, 0.1 M HClO4 solution at room temperature. Disk electrode: sputtered model electrodes with different loadings deposited on a glassy carbon disk, Ring electrode: Pt. Rotation speed 1600 rpm H_2O_2 yield plotted versus (a) Disk potential and (b) Pt loading.

Hydrogen peroxide was detected at potentials below 0.8 V vs RHE, and the yield of H_2O_2 increased with decreasing potential. This indicates that the 2 electron pathway does in fact occur on the surface of Pt/C catalysts. A significant increase in H_2O_2 formation was detected at potentials > 0.2 V vs. RHE, which is generally attributed to the blockage of surface active sites by adsorbed hydrogen atoms, preventing the dissociation adsorption of oxygen molecules (Inaba *et al*., 2004). It has been found in many studies that a reduction in the available active Pt sites for the ORR, enhances the production of H_2O_2 formation, which would explain the enhanced H_2O_2 formation observed in Figure 5.13 (a) below 0.2 V, where the surface coverage of adsorbed spectator species is greatest (Katsounaros *et al*., 2012).

The 2 µg/cm^2 loading shows the greatest H_2O_2 production at all potentials. According to Indaba *et al*. (2004), the enhanced H_2O_2 formation also indicates the presence of small Pt nanoparticles, which agrees with the findings of the SEM and shifting oxide reduction peak in the CV's. Analogously, the minimal H_2O_2 production for the higher loading electrodes (20 and 50 µg/cm^2), indicates the predominant occurrence of the 4 electron pathway forming water, with insignificant amounts of H_2O_2 formed. This reaction has been found to occur mainly on larger, agglomerated Pt nanoparticle. The reason for reduced H_2O_2 formation on large Pt particles is thought to be due to the closer proximity of active sites on Pt agglomerates compared with isolated platinum nanoparticles (Antoine &Durand, 2000). That is, if a H_2O_2 species is formed there is a greater probability of it being reduced to H_2O by a nearby active catalyst site on an agglomerated Pt particle than on an isolated particle (Inaba *et al.*, 2004).

The RRDE findings are significant as they re-enforce the importance of understanding the particle size effect on the ORR, as H_2O_2 formation reduces the overall ORR current and hence reduces the catalytic performance.

5.3.6 **Summary of findings - sputtered model electrodes**

The main findings of this study are in line with the findings by Schwanitz *et al.* (2012). Sputtered model electrodes show a change in surface morphology as Pt loading increases, starting from isolated Pt nanoparticles (2-3 nm) for loadings > 20 $\mu g_{Pt}/cm^2$ to Pt agglomerates and extended surfaces for loadings above 20 $\mu g_{Pt}/cm^2$. As the Pt loading increases from 2 to 100 $\mu g_{Pt}/cm^2$ the ECSA increases non-linearly, due to agglomeration at higher loadings. Increasing the loading leads to an increase in average particle size and a corresponding increase in specific activity, $i_{k,spec}$ and leads to a decrease in the mass activity, $i_{K,mass.}$.

This study has been useful in highlighting the different properties of isolated Pt nanoparticles and Pt agglomerates on the ORR. The oxide reduction peaks in the CV's in Figure 5.7 (b) indicate the greater oxophilicity of small Pt nanopartciles compared to larger Pt particles. This finding links to the reduced specific activity of small Pt nanoparticles observed for the low Pt loading electrodes, owing to the greater surface coverage of OH species, which effectively reduce the number of active Pt sites available for the ORR. The RRDE results also highlight how the surface structure of small Pt nanoparticles influences the production of H_2O_2. The exact reasons for this increase H_2O_2 formation are not clear, but it can be speculated from literature and this study that the surface morphology and electronic structure of the Pt nanoparticles have a significant influence on the electrocatalytic activity of Pt towards the ORR and subsequent side reactions including H_2O_2 formation.

In addition to the work by Schwanitz *et al*. (2012) it was found that in general the ECSA calculated from the CO-stripping method is slightly higher than that obtained from the H_{upd} method, except for the low loading samples where the two ECSA calculation methods are similar. It was also found that at higher Pt loadings i.e 50 and 100 $\mu g_{Pt}/cm^2$, a double voltammeric peak was observed for the CO oxidation reaction. This finding correlates with findings by Maillard *et al*. (2005) and indicates the different surface morphologies present.

University of Cape Town

5.4 MOCVD supported catalysts

In an attempt to understand how the results obtained for the model system can be mirrored by a practical system, carbon supported platinum catalysts were prepared with weight % of 20, 40, 60 and 80 wt.% Pt by MOCVD. Similar physical and electrochemical characterisation as the sputtered model electrodes, was carried out on the MOCVD catalysts.

A theoretical ideal model for the MOCVD catalysts was developed in a similar fashion to the ideal sputtered l electrode model with a few differences. The following assumptions were made to develop the model.

- Platinum and carbon particles are perfects spheres with diameters of 3 nm and 40 nm respectively.
- Platinum particle size remains constant as platinum loading increases.
- Platinum particles are homogenously dispersed over the carbon surface.
- Platinum utilisation is 100%.
- Platinum surface roughness factor 1.8
- 100 % availability of carbon surface for platinum deposition

The Figure 5.14 below illustrates the ideal model particles used to develop the system.

University of Cape Town

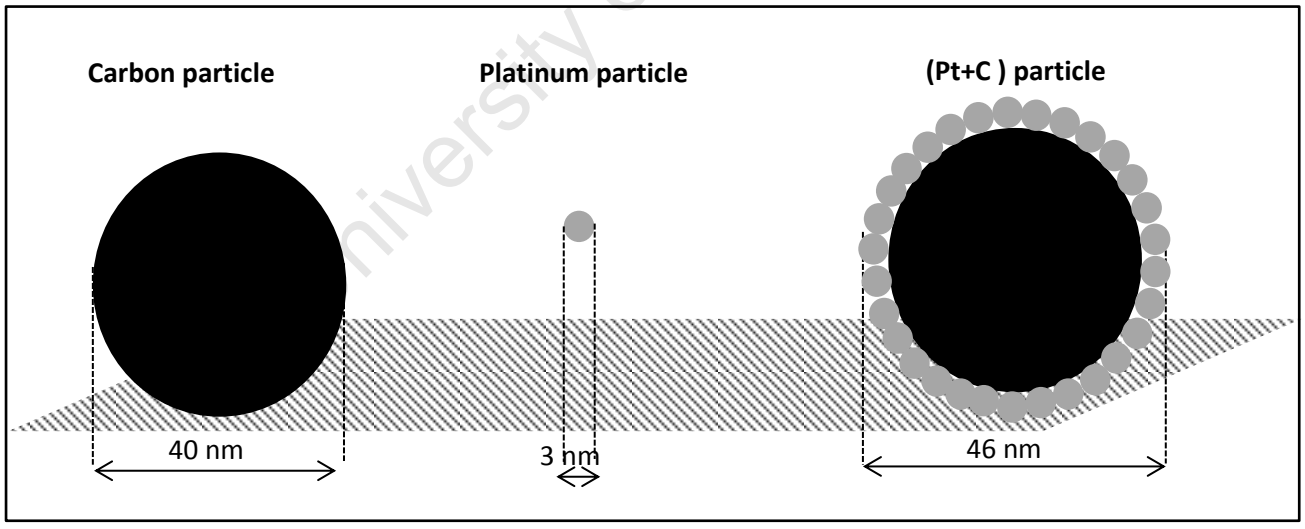

Figure 5.14 : Illustration of (a) carbon particle diameter, (b) Platinum particle diameter and (c) overall diameter of a single carbon particle with a 3 nm platinum film.

Table 5.6 below summarises the physical properties of single carbon and platinum particles.

Table 5.6: Physical properties of a single carbon particle and a single platinum particle

Property	units	Symbol	Formula	Value
Carbon particle				
diameter	cm	d_c	-	0.00004
radius	cm	r_c	-	0.000003
Surface area	cm^2	SA_c	$SA_c = 4.\pi.r_c^2$	5.03 x10^{-11}
Cross-sectional	cm^2	XA_c	$XA_c = \pi.r_c^2$	1.26 x10^{-11}
volume	cm^3	V_c	$V_c = \frac{4}{3}.\pi.r_c^3$	3.35 x10^{-17}
Platinum particle				
diameter	cm	d_{Pt}	-	0.0000003
radius	cm	r_{Pt}	-	0.00000015
density	g/cm^3	P_{Pt}	-	21.46
Surface area	cm^2	SA_{Pt}	$SA_{Pt} = 4.\pi.r_{Pt}^2$	2.83 x10^{-13}
Volume	cm^3	V_{Pt}	$V_{Pt} = \frac{4}{3}.\pi.r_{Pt}^3$	1.41 x10^{-20}

Table 5.7 summarises the physical properties and formulas used to calculate the required information for a single carbon particle with 50 % of its surface covered by a complete 2 nm platinum film.

Table 5.7 Summary of physical properties and formulas used for a single carbon particle covered by a 2 nm thick platinum film

Property	units	Symbol	Formula	Value
Platinum film +carbon particle				
Diameter Pt + Carbon	cm	$d_{(Pt+C)}$	$d_{(Pt+C)} = 2.d_{Pt} + d_c$	0.0000046
Radius Pt + Carbon	cm	$r_{(Pt+C)}$	$r_{(Pt+C)} = r_{Pt} + r_C$	0.0000023
Pt surface roughness factor	-	rf	-	1.8
Surface area Pt film	cm^2	$SA_{Pt\ film}$	$SA_{Pt\ film} = rf.4.\pi.r_{(Pt+C)}^2$	1.20 x10^{-10}
Volume Pt + C	cm^3	$V_{(Pt+C)}$	$V_{Pt} = \frac{4}{3}.\pi.r_{(Pt+C)}^3$	5.10 x10^{-17}
Volume platinum film	cm^3	$V_{Pt\ film}$	$V_{Pt\ film} = V_{(Pt+C)} - V_c$	1.75 x10^{-17}
Electrode diameter	cm	d_E	-	0.561
Electrode radius	cm	r_E	-	0.25
Electrode Surface area	cm^2	A_E	$SA_E = \pi.r_E^2$	0.196
Number carbon particles	-	n_c	$n_c = \frac{SA_E}{XA_c}$	1.56E x10^{10}

Figure 5.15 below illustrates the overall model system used to create and ideal model to calculate the ECSA for the sputtered electrodes. A monolayer of carbon particles with diameters of 40 nm deposited onto the

University of Cape Town

surface of a glassy carbon electrode disk with a diameter of 5 mm, is covered with a 2 nm thick film of platinum on 50 % of the carbon particle surface.

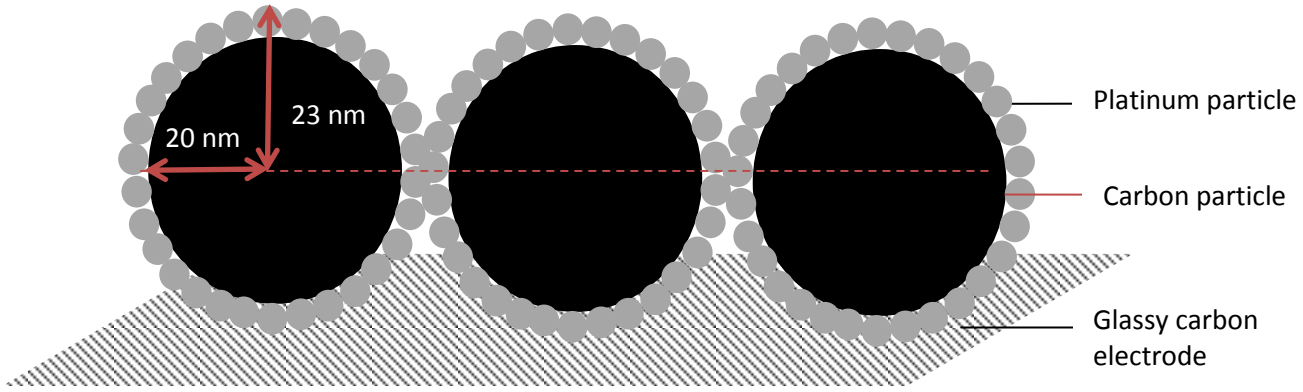

Figure 5.15 : Ideal model system for MOCV catalysts. Illustrating a single layer of platinum nanoparticles deposited onto a monolayer of spherical carbon particles supported on a glassy carbon electrode surface

Table 5.8 below summarises the variables used to calculate the idealised ECSA for the MOCVD model.

Table 5.8 Summary of variables used to calculate the model Pt loading and ECSA

Property	units	Symbol	Formula	Value
Pt particles supported on a monolayer of carbon on glassy carbon electrode				
% carbon surface available	%	a	-	100
Total carbon surface area	cm^2	$SA_{c,total}$	$SA_{C,total} = a.n_c.SA_c$	9.887×10^{-01}
Total platinum surface area	cm^2	$SA_{Pt,\ total}$	$SA_{Pt,total} = n_c.SA_{Pt\ film}$	2.354
Total platinum volume	cm^3	$V_{Pt,\ total}$	$V_{Pt,total} = n_c.V_{Pt\ film}$	3.43×10^{-07}
Total mass platinum on electrode	g	$m_{Pt,\ total}$	$m_{Pt,total} = V_{Pt,total} \cdot \rho_{Pt}$	7.37×10^{-06}
Total carbon volume	cm^3	$V_{C,\ total}$	$V_{C,total} = n_c.V_C$	6.59×10^{-07}
Total mass carbon	g	$m_{C,\ total}$	$m_{C,total} = V_{C,total} \cdot \rho_C$	1.19×10^{-06}
wt.%Pt for 100% coverage	**wt.% Pt**	**w_{Pt}**	$\boldsymbol{w_{Pt} = \frac{m_{Pt,total} \cdot 100}{(m_{Pt,total} + m_{C,total})}}$	**86**
ECSA	**cm^2_{Pt}/cm^2_{carbon}**	**ECSA**	$\boldsymbol{ECSA = \frac{SA_{Pt,total}}{SA_{C,total}}}$	**2.38**

The calculations above assume a 100% availability of the carbon surface, which is completely covered by a 3 nm platinum film. Therefore the model predicts a continuous platinum surface with a film thickness of 3 nm at a platinum weight % of 86 wt.%Pt, which corresponds to an ECSA of 2.38 cm^2_{Pt}/cm^2_{carbon}. These values were used as the basis of calculation of the ideal model system, and were used to scale the ideal values from 86 wt.% Pt to the required values of 20, 40, 60 and 80 wt.% Pt. Table 5.9 below summarises the results for the ideal theoretical model ECSA versus the experimentally determined ECSA measured in cm^2_{Pt}/cm^2_{carbon}.

Table 5.9 Ideal CSA and experimental ECAS for each sputtered platinum loading

wt.% Pt	Ideal ECSA (cm^2_{Pt}/cm_{carbon}^2)	Expt. ECSA (cm^2_{Pt}/cm_{carbon}^2)
20	0.553	0.0687
40	1.11	0.154
60	1.66	0.231
80	2.21	0.365

University of Cape Town

5.4.1 **TEM and STEM**

The TEM and STEM images illustrate the progression from low to high platinum loadings and the subsequent increase in the platinum density per unit area depicted by the increase in the white areas representing platinum metal.

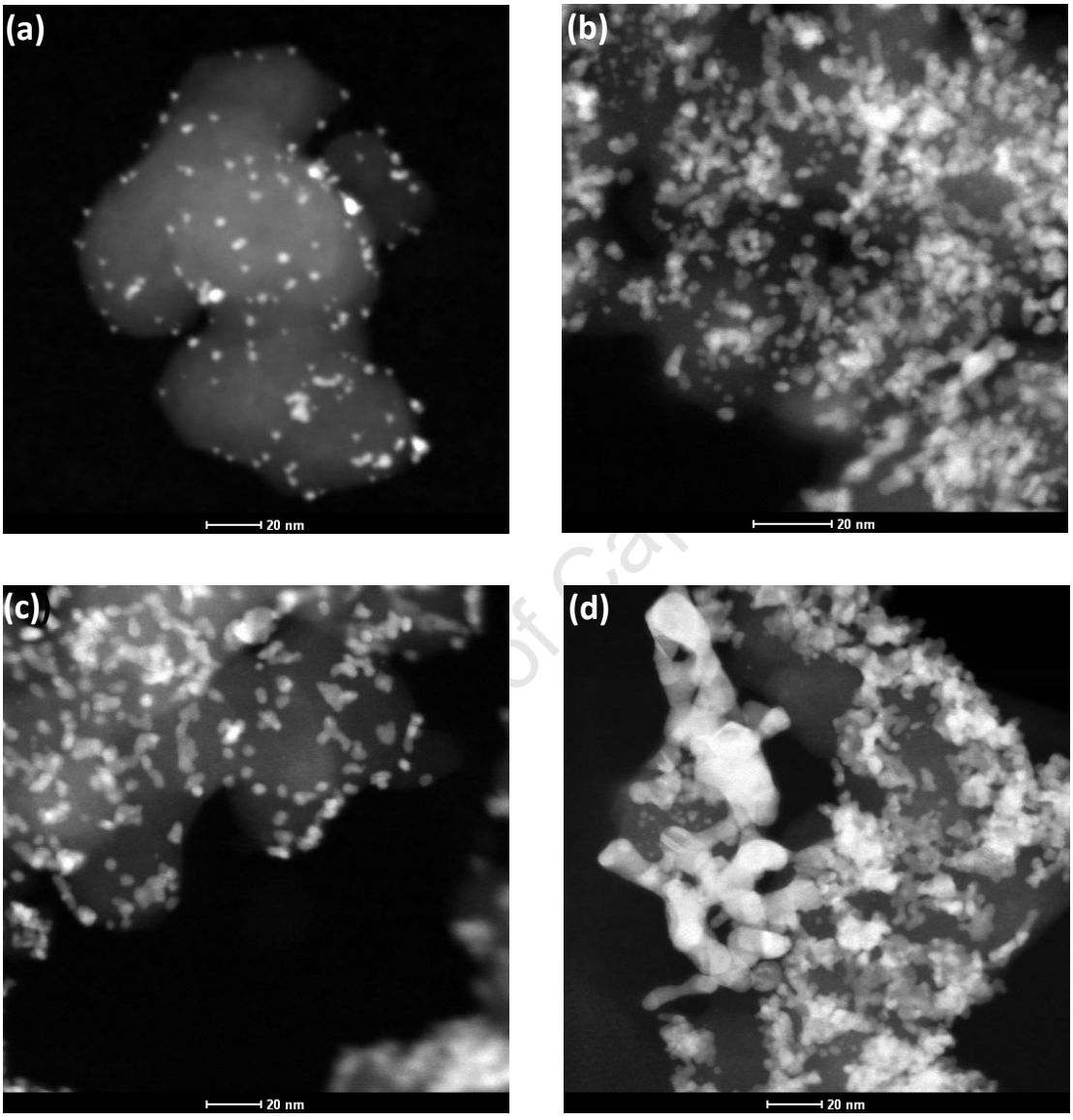

Figure 5.16 : STEM images at 20 nm resolution of MOCVD catalysts with (a) 20 wt.%Pt, (b) 40 wt.% Pt, (c) 60 wt.% Pt and (d) 80 wt.% Pt.

The STEM images above illustrate the increasing platinum density as platinum loading increases from 20 to 80 wt.% Pt. The platinum is represented by the bright white areas in the image while the grey areas represent the carbon support particles. When comparing Figure 5.16 (a) and (d) there is a distinct difference between the particles, the 20 Wt% Pt sample in Figure 5.16 (a) has distinct nanoparticles whereas the 80

wt.% Pt sample shows areas where the bright white seems to have merged which may indicate particle agglomeration.

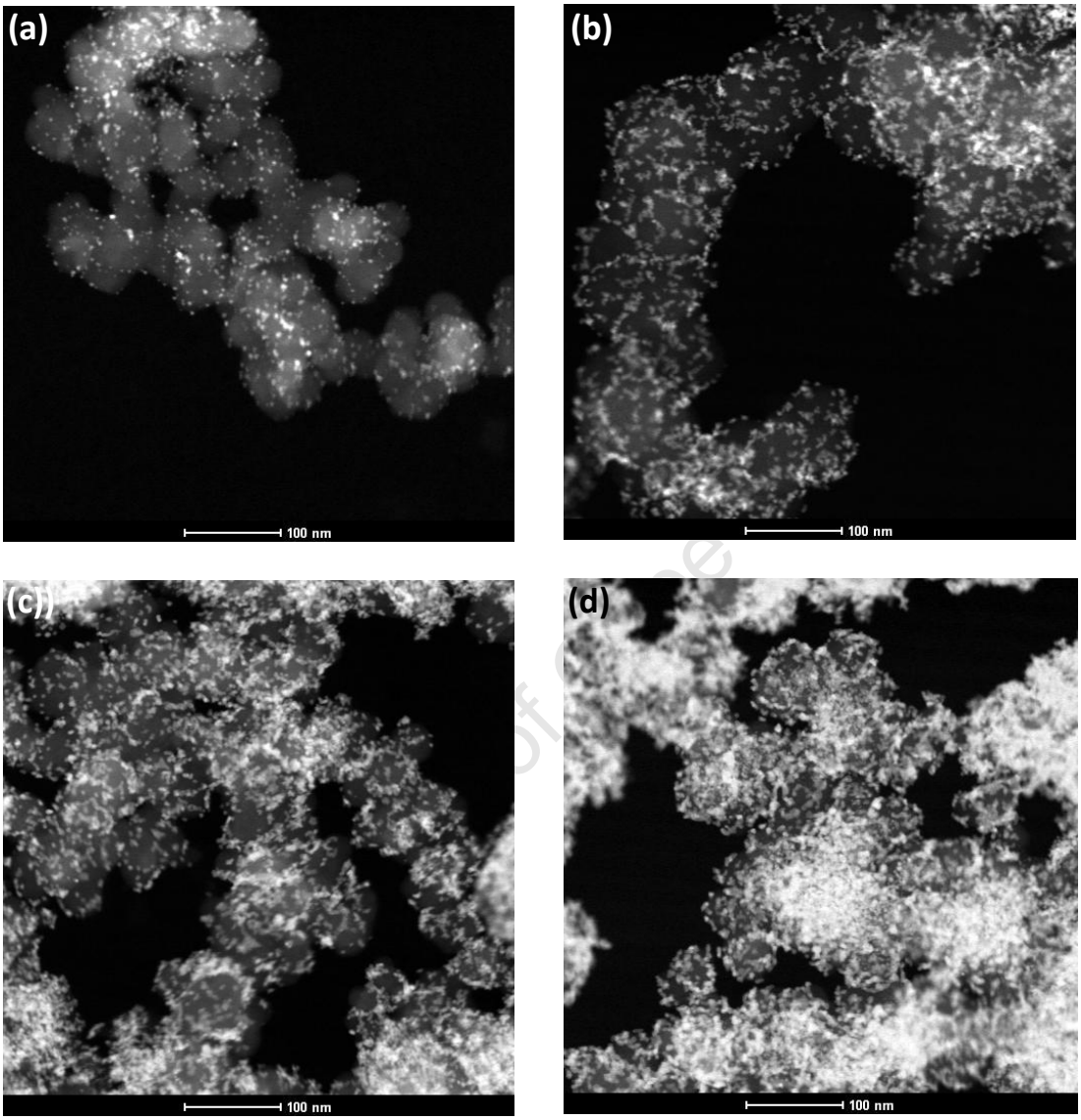

Figure 5.17 : STEM images at 100 nm resolution of MOCVD catalysts with (a) 20 wt.%Pt, (b) 40 wt.% Pt, (c) 60 wt.% Pt and (d) 80 wt.% Pt with the associated particle size distributions.

The STEM images above give a broader view of the catalysts systems. The most significant observation is the increasing platinum density with increased platinum loading indicated by the bright white areas. It is also interesting to note that there is very little carbon visible for the 80 wt. % sample at this magnification, which indicates a very densely packed platinum surface. It is difficult to identify single platinum particles in the very dense areas of the 80 wt.% sample, and the particle size distribution indicates a size increase from 20 to 80 wt.% which indicates particle agglomeration. The TEM images of the MOCVD catalysts are illustrated in Figure 5.18 below.

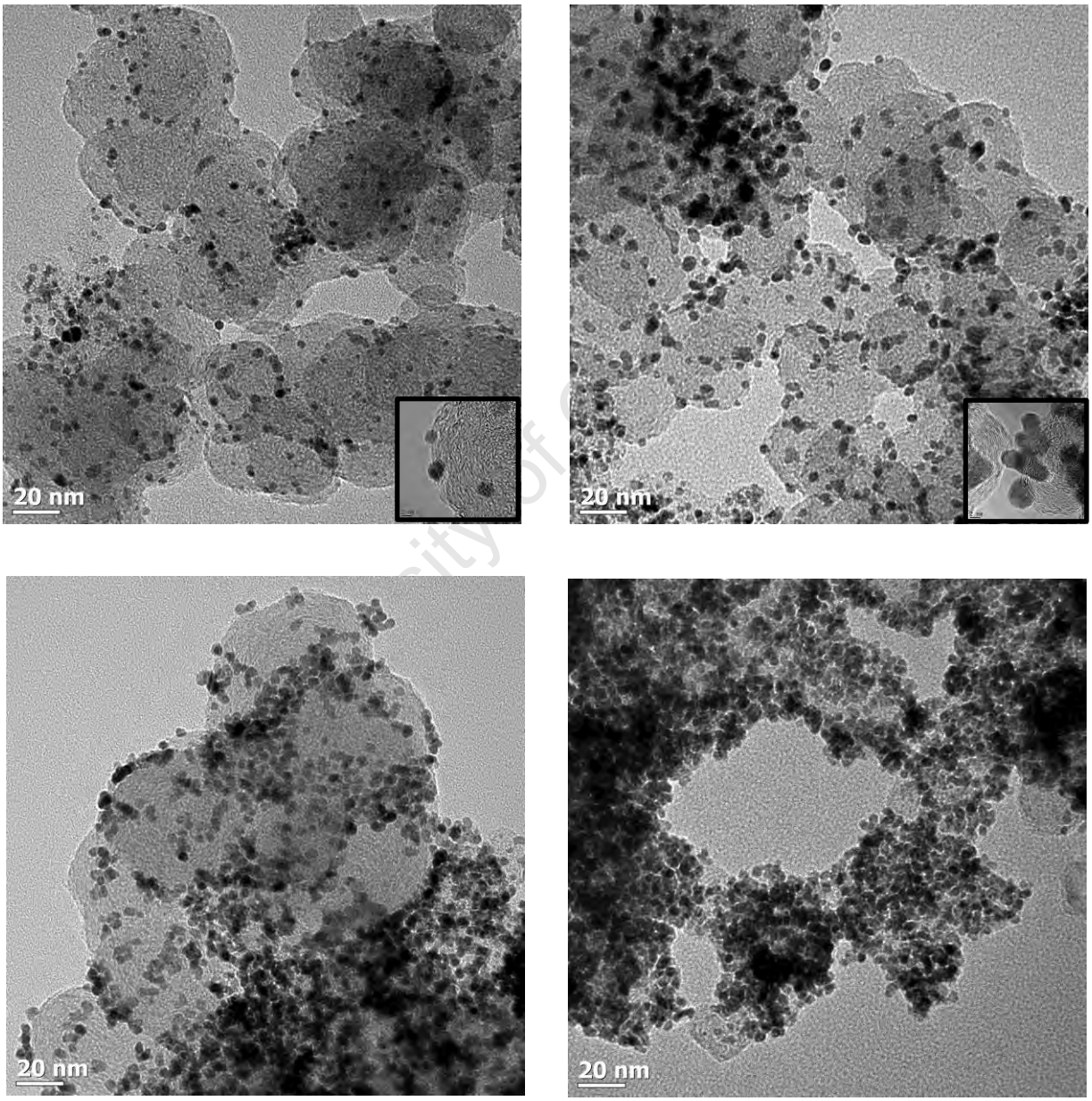

Figure 5.18 : TEM images at 20 nm resolution of MOCVD catalysts with (a) 20 wt.%Pt, (b) 40 wt.% Pt, (c) 60 wt.% Pt and (d) 80 wt.% Pt.

It is evident from the TEM images that the average particle size is increasing as platinum loading is increased. This is confirmed by the particle size distributions (see Appendix, Figure 7.1) which confirm an increase in average particle size from the 20 to the 80 wt.% Pt catalysts.

5.4.2 **ThermoGravimtetric Analysis (TGA)**

TGA was carried out for each MOCVD prepared catalyst to confirm the correct amount of platinum was deposited on the carbon support surface.

Table 5.10: TGA results showing initial and final masses after the carbon support has been oxidised in air

Theoretical wt.% Pt	Initial mass (mg)	Final mass (mg)	Actual wt.% Pt
20	1.41	0.250	18
40	2.01	0.934	46
60	5.62	3.33	59
80	6.18	4.87	79

The results from TGA showed that the MOCVD catalysts were relatively close to the theoretical wt.% Pt expected.

University of Cape Town

5.4.3 **XRD**

XRD analysis was carried out on all the MOCVD samples and the results of this analysis are illustrated in Figure 5.19 below.

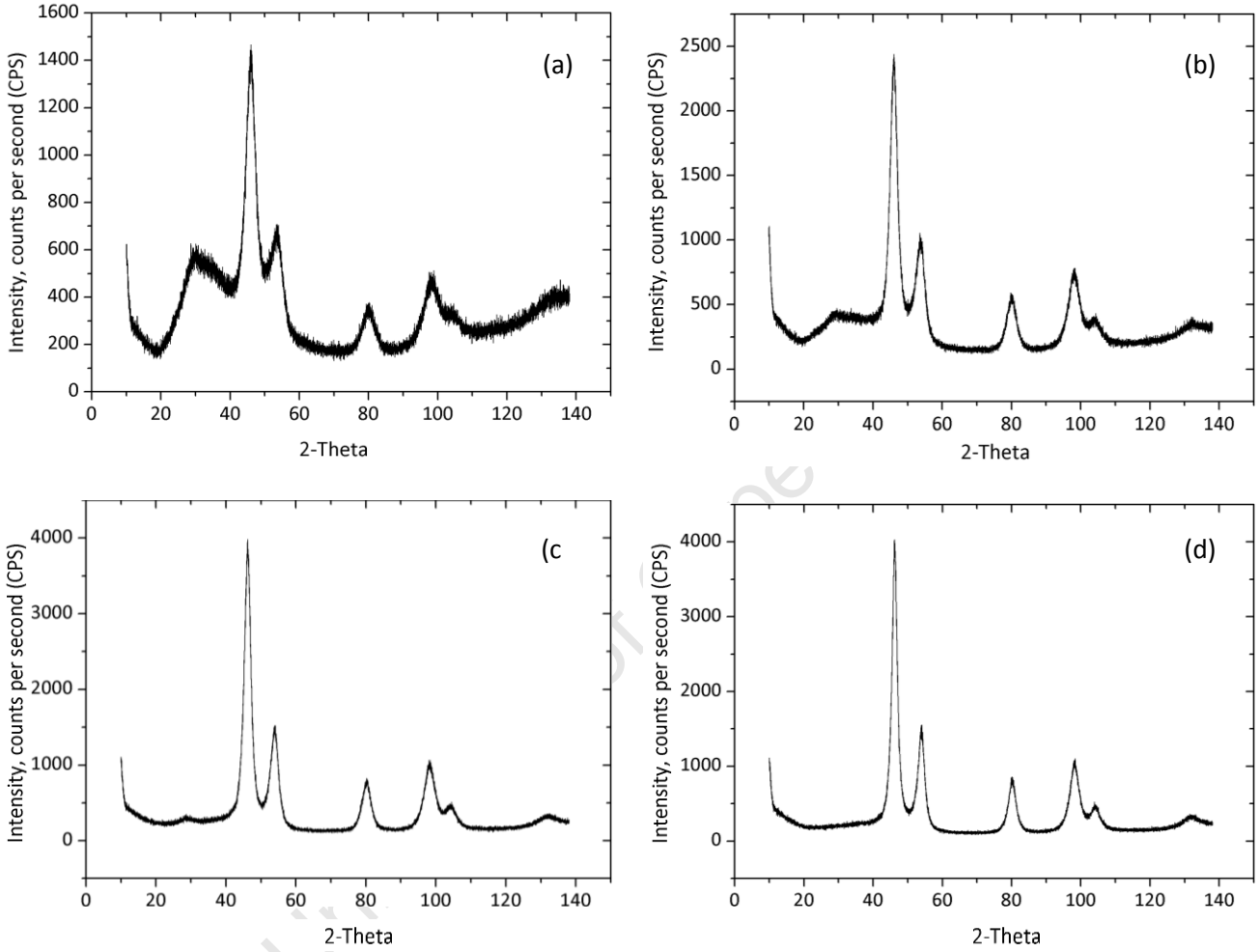

Figure 5.19 ; XRD graphs for platinum supported on carbon catalysts prepared by MOCVD with increasing platinum loadings of (a) 20 wt.% Pt. (b) 40 wt.% Pt. (c) 60 wt.% Pt and (d) 80 wt.% Pt.

The Scherrer equation below was used to calculate the average platinum crystallite size (L) in all the samples. The table below summarises the average crystallite sizes for the different platinum weight percent MOCVD catalysts. The (111), (200) and (220) peaks were used to calculate the average crystallite sizes, these peaks are indicated in Figure 5.19 (a).

Table 5.11: Average crystallite size calculated using the Scherrer equation for MOCVD catalyst samples

Weight percent	Average crystallite size (nm)
20	3.37
40	4.11
60	4.56
80	5.41

The XRD analysis of the average crystallite size indicates an increase in particle size from 3.37 nm to 5.41 nm as the platinum loading is increased. This result is in line with the findings by TEM analysis.

University of Cape Town

5.4.4 **Electrochemical characterisation -**

Figure 5.20 (a) below illustrates the cyclic voltammograms for the various weight percentages of platinum supported on Vulcan. Figure 5.20 (b) shows the trend of ECSA with increasing platinum weight %. The ECSA values were normalised with respect to the surface area of the carbon support present on the electrode during measurements.

Table 5.12: Summary of ECSA calculated by the H_{upd} charge area

	$ECSA_{Hupd}$		
wt.% Pt	**$\mu g_{Pt}/cm^2$**	**cm^2_{Pt}/cm^2**	**cm^2_{Pt}/cm^2_{Carbon}**
20	8.88	4.34	0.0517
40	16.6	8.51	0.114
60	50.8	17.32	0.213
80	64.7	22.17	0.410

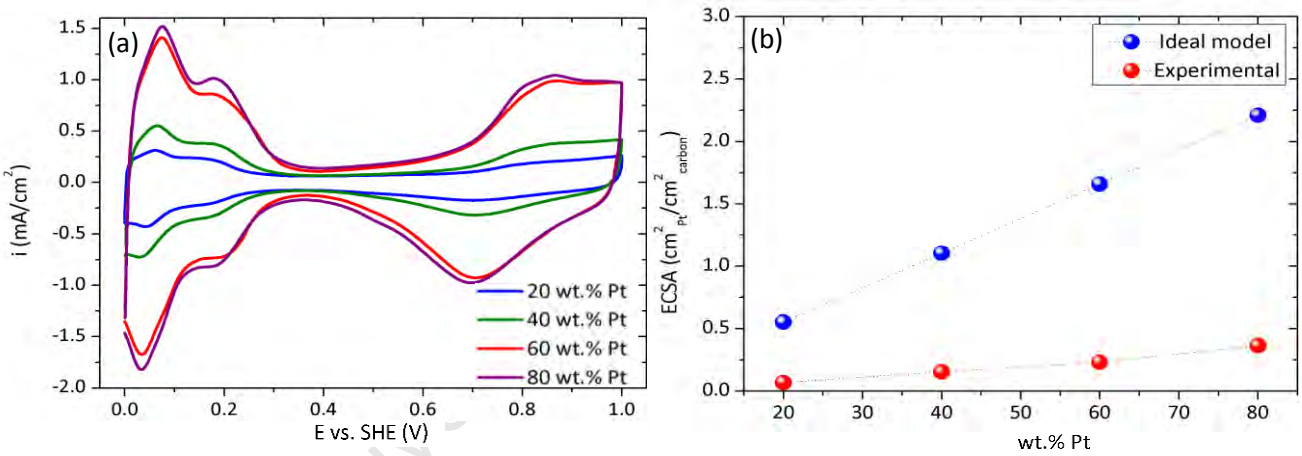

Figure 5.20 : Cyclic voltammograms carried out in an Ar saturated 0.1 M $HClO_4$ solution at room temperature, sweep rate 50 mV/s for different wt.% Pt catalysts (a) Comparison of CV's for 20, 40, 60 and 80 wt.% Pt. (b) ECSA calculated by H_{upd} area versus wt.% Pt.

The ECSA is seen to increase as Pt weight % on carbon is increased from 20 to 80 wt.% Pt, this can be seen by the increasing H_{upd} area in Figure 5.20 (a).The increase in ECSA can be explained by an increasing amount of available platinum active sites as the amount of platinum on the carbon surface increases, while the relative amount of carbon decreases. The curve representing the ideal theoretical ECSA lies a significant amount above the experimental curve. The model predicts a 100% surface coverage of a 40 nm carbon particle with platinum nanoparticles of 3 nm, at a total weight % platinum of 86%. In reality however, complete carbon coverage was not obtained at 80%, this was confirmed by the TEM images in Section 5.4.1. The experimental system follows the ideal model trend, but since the model has been developed with simplifying assumptions such as 100% catalyst utilisation, the experimental results will inevitably be lower than the ideal case.

Figure 5.20 (a) below illustrates the CO stripping voltammograms used to calculate the ECSA using the area under the CO oxidation peaks. Figure 5.21 (b) illustrates the CO stripping peaks observed between 0.5 and 0.9 V vs SHE. The low potential peak is assigned as Peak I and the high potential peak is assigned as Peak II. Figure 5.21 (c) indicates the ratio of peak I to the total peak area, illustrating how the peak ratio changes with wt. % Pt. and Figure 5.21 (d) shows the relationship between the $ECSA_{CO\ stripping}/ECSA_{Hupd}$ with wt.% Pt.

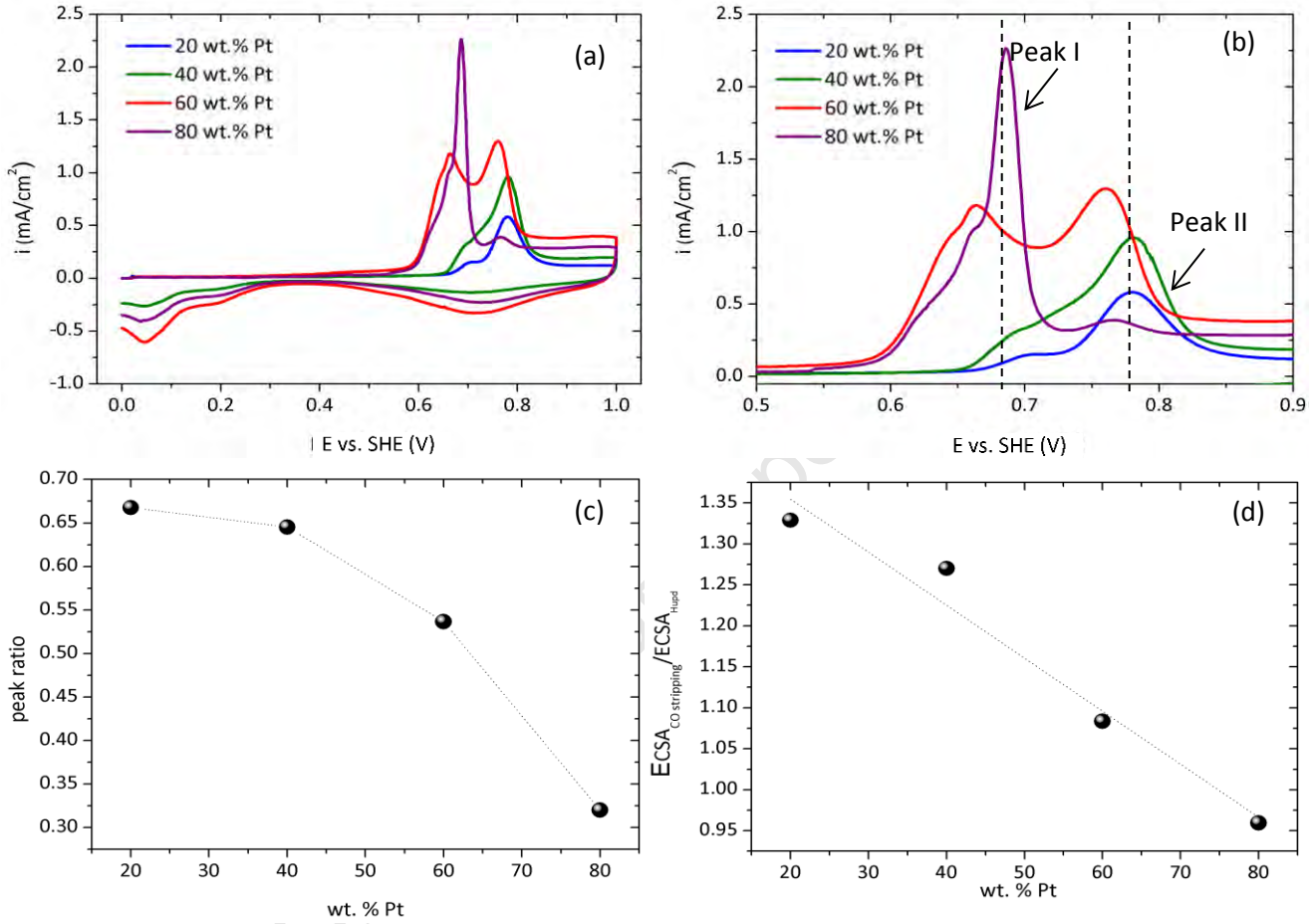

Figure 5.21 : (a) CO stripping voltammograms in an Ar saturated 0.1 M $HClO_4$ solution at a sweep rate of 20 mV/s for 20, 40, 60 and 80 wt.% Pt catalysts, at room temperature. (b) CO oxidation peaks 20, 40, 60 and 80 wt.% Pt catalysts, where Peak I indicates the low potential peak and Peak II indicates the high potential peak. (c) ratio of (peak II/total peak area) versus wt.% Pt in each MOCVD catalyst.

Table 5.2 below summarises the results of the ECSA calculated by H_{upd} and CO stripping methods.

Table 5.13: Summary of ECSA calculated by H_{upd} area and CO stripping oxidation peak area

wt. % Pt	$ECSA_{Hupd}$ (cm^2_{Pt}/cm^2_{carbon})	$ECSA_{COstripping}$ (cm^2_{Pt}/cm^2_{carbon})	$ECSA_{CO\ stripping}/ECSA_{Hupd}$
20	0.0517	0.0687	1.33
40	0.120	0.150	1.27
60	0.213	0.231	1.08
80	0.380	0.365	0.96

The most striking feature of the CO stripping voltammograms in Figure 5.21 (a) is the double voltammeric peak observed between 0.76 and 0.95 V *vs* SHE wich corresponds to the findings by Maillard *et al*., (2005). Maillard *et al*. (2005) attributed the double peak to the effect of increasing platinum loading above the threshold of particle agglomeration, which gives rise to "peak splitting". He also concluded that platinum agglomerates show a high electrocatalytic activity and are accountable for the low potential peak in the CO stripping voltammogram, while the high potential peak is attributed to the isolated platinum nanoparticles with a lower electrocatalytic activity.

The number and position of CO oxidation peaks varies with wt.% Pt. As the wt.% Pt increases the intensity of peak I increases, while peak II intensity decreases. This could indicate increasing particle agglomeration with increasing Pt loading. The ratio of peak II/(total peak area) shown in Figure 5.21 (c) was determined by deconvolution of the CO stripping peaks in Figure 5.21 (a) (See Appendix, Figure 7.2). As the platinum loading is increased from 20 to 80 wt.% Pt, the ratio of peak I/(total peak area) decreases from 0.67 to 0.32. Peak I area and amplitude increases as platinum loading increases, according to Maillard *et al*. (2005), this indicates an increase in the amount of platinum agglomerates present and can be confirmed by the TEM and XRD where particle agglomerates and increased particle size were observed (See Section 5.4.1). Peak I dominates the overall CO oxidation peak area after 50 wt.% (See Figure 5.21 (c)) which gives a rough estimation of the point at which particle agglomeration becomes the dominating particle size effect in this catalyst system.

Many authors have corroborated the findings by Maillard *et al.* (2005). Komatsu and Osawa, (2009) confirmed the presence of multiple CO stripping peaks by IR spectroscopy and attributed the differernt peaks to CO oxidation on terrace and edge sites, which are essentially a particle size dependent property of platinum. After a survey of available literature on CO stripping peak multiplicity, Ciapina *et al*., (2010) found that there are various possibilities for the multiple peaks observed. These possibilities include (i) preferred

University of Cape Town

surface plane orientation, (ii) CO oxidation occurring on edge and terrace sites, (iii) particle size effects, (iv) the presence of particle agglomerates and surface defects and (v) the role of CO surface diffusion between the different facets on a platinum nanoparticle (Ciapina *et al.*, 2010). All these possibilities indicate an effect on CO oxidation by the surface properties or structure of the platinum particles. Figure 5.21 (d) indicates that the two different ECSA calculation methods are comparable at high platinum loadings, indicated by a $ECSA_{CO\ stripping}/ECSA_{Hupd}$ ratio approximately equal to 1.

5.4.5 **Electrocatalytic activity of MOCVD catalysts**

The oxygen reduction reaction curves are illustrated in Figure 5.22, these curves were used to determine the limiting diffusion current and equation 2.7 was used to calculate and plot the kinetic current (i_k). The trends in kinetic current density (i_k) and the subsequent mass and specific activities are illustrated in Figure 5.22 respectively.

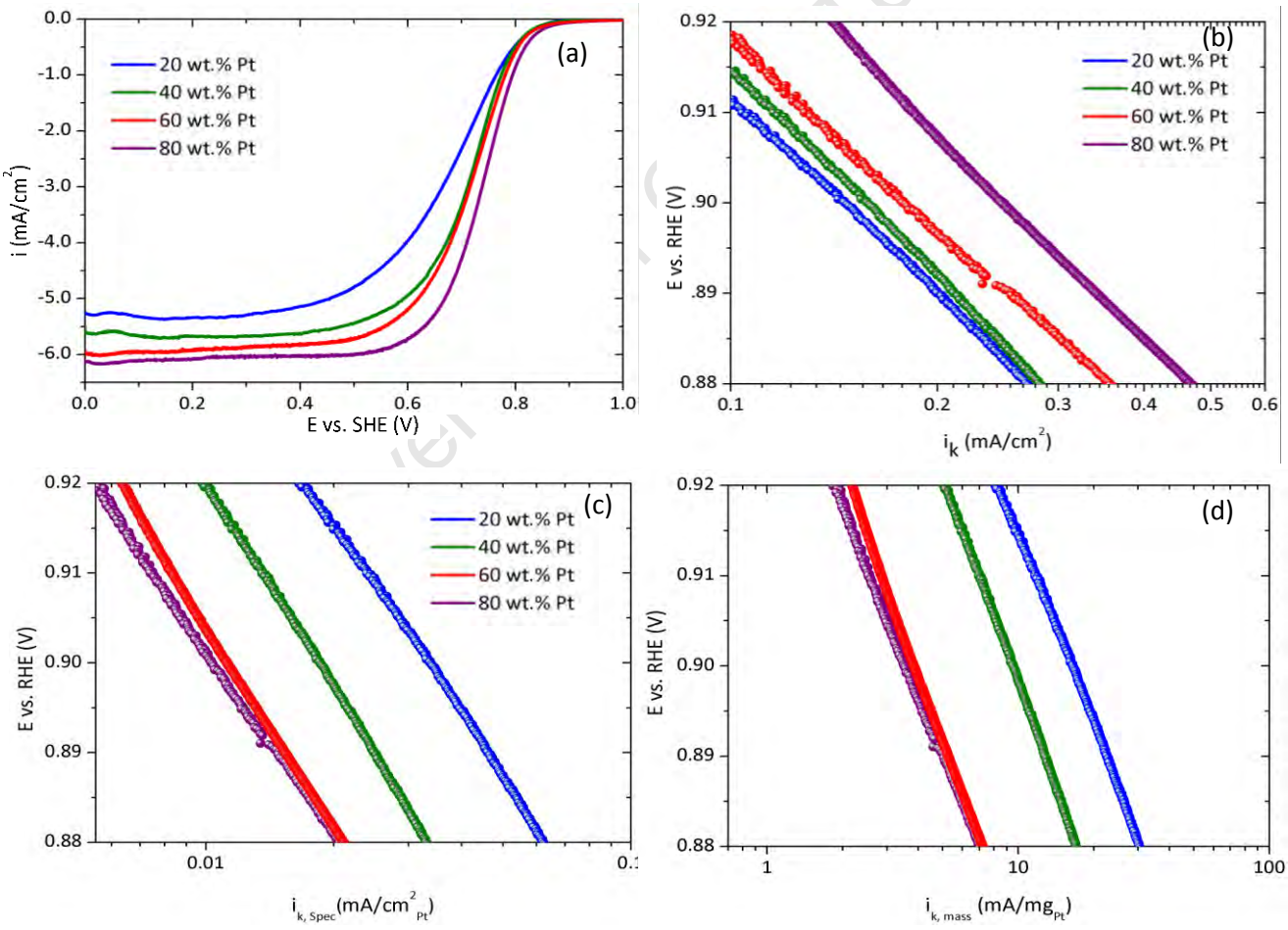

Figure 5.22 : (a) Oxygen reduction current densities for cathodic sweeps (5 mV/s, 1600 rpm) in oxygen saturated 0.1 M $HClO_4$ solution at room temperature for MOCVD catalysts with different wt.% Pt (b) oxygen reduction tafel plot showing mass transport corrected current densities (i_k) for the ORR, obtained from the cathodic sweeps (5 mV/s, 1600 rpm) in an oxygen saturated 0.1 M $HClO_4$ solution (log i_k versus potential). (c) Comparison of oxygen reduction (a) mass activity ($i_{K,\ mass}$) and (b) surface specific activity ($i_{K,\ spec}$) of MOCVD catalysts with different wt.% Pt at room temperature, current densities measured at a constant potential of 0.9 V vs. RHE, indicated by the horizontal line at 0.9 V vs. RHE on (c) and (d).

Table 5.3 below summarises the diffusion (i_d) and kinetic currents (i_k) and the mass and area specific activities for the MOCVD catalysts with 20 to 80 wt.% Pt.

Table 5.14: Summary of diffusion limiting current, kinetic current, specific activity and mass activity for20, 40, 60 and 80 wt.% Pt MOCVD catalysts

wt.% Pt	I_d (mA/cm^2)	$i_{k\ (0.9\ V)\ vs.\ SHE}$	$i_{k,spec\ (0.9\ V)}$ (mA/cm$^2_{Pt}$)	$i_{k,mass\ (0.9\ V)}$ (mA/mg$_{Pt}$)
20	5.37	0.142	0.0338	15.8
40	5.69	0.159	0.0187	9.49
60	5.93	0.174	0.0113	3.93
80	6.11	0.248	0.0102	3.50

Figure 5.22 (a) shows that the theoretical limiting current for a 5.61 mm diameter disk electrode of 6.04 mA/cm^2, was not reached by the 20 and 40 wt.% Pt catalysts and this was most likely due to H_2O_2 formation and will be further discussed in Section 5.4.6. The kinetic current densities (i_k) measured at 0.9 V vs. SHE, were seen to increase with increasing wt.% Pt. However the specific and mass activities were seen to decrease with increasing wt.% Pt . The mass and surface area specific activity trends measured at 0.9 V vs. SHE are plotted in Figure 5.23 below.

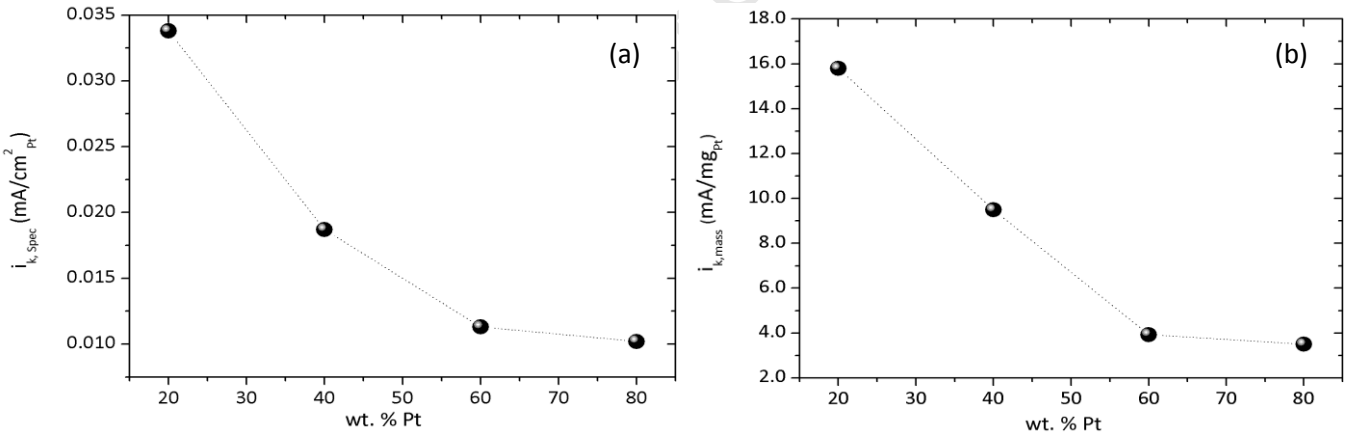

Figure 5.23 : Comparison of (a) surface specific and (b) mass activity for the oxygen reduction reaction measured at 0.9 V vs. SHE for MOCVD catalysts versus wt.% Pt

The surface specific activity is seen to decrease with increasing Pt loading. The 80 and 60 wt.% Pt catalysts show similar surface activities indicating similar surface properties of the two catalysts. The 20 and 40 wt.% Pt catalysts show a significantly higher area specific activity than the 60 and 80 wt. % Pt catalysts. The separation between the low and high loading catalyst specific activities could indicate a change in surface properties form low to high Pt loading. The mass specific activities decrease with increasing Pt loading, this trend is expected since as the platinum loading increases, the average particle size increases confirmed by XRD and TEM and indicates particle agglomeration. Hence the platinum utilisation per unit mass decreases,

hence the decreasing trend observed in Figure 5.23 (b). The overall activity of the MOCVD catalysts is lower than expected and could be attributed to the fact that the cathodic sweep was used to determine the kinetic current and the sweep rate used was 5 mV/s as opposed to 20 mV/s.

5.4.6 **RRDE results – hydrogen peroxide formation**

Figure 5.24 below illustrates the RRDE results obtained for the MOCVD catalysts with different wt.% Pt. Figure 5.24 (a) shows the contribution of the peroxide current (% H_2O_2) to the overall current produced during the ORR reaction, Figure 5.24 (b) shows the corresponding peroxide formation curves measured at the same time as the ORR curves.

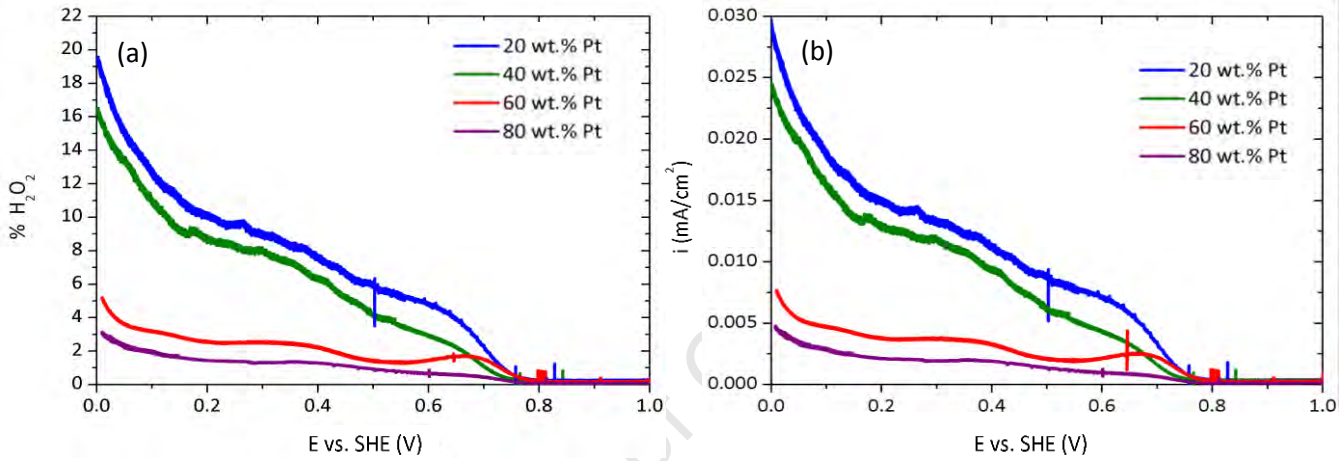

Figure 5.24 : a) H_2O_2 yield for oxygen reduction in an oxygen saturated, 0.1 M $HClO_4$ solution at room temperature. Disk electrode: GC electrode with 15 µL of MOCVD catalyst ink on the surface of a glassy carbon electrode, Ring electrode: Pt. Rotation speed 1600 rpm H_2O_2 yield plotted versus Disk potential (b) current density versus disk potential for the different wt.% Pt MOCVD catalysts

Hydrogen peroxide formation is seen to occur at potentials below 0.8 V vs SHE, which corresponds to the sputtered model electrode system in Section 5.2. The 20 wt.% Pt catalyst is seen to produce the most H_2O_2 during the ORR, which could be used to explain the reduced diffusion current observed for this catalyst in Figure 5.24 (a) as the 2 electron pathway for H_2O_2 formation reduces the overall efficiency of the ORR which is predominantly a 4 electron reaction. A similar argument could be used to explain the reduced diffusion current observed for the 40 wt.% Pt catalyst. Figure 5.25 below depicts the theoretical reaction pathways which H_2O_2 species could form on low loading, highly dispersed isolated Pt nanoparticles (Katsounaros *et al.*, 2012).

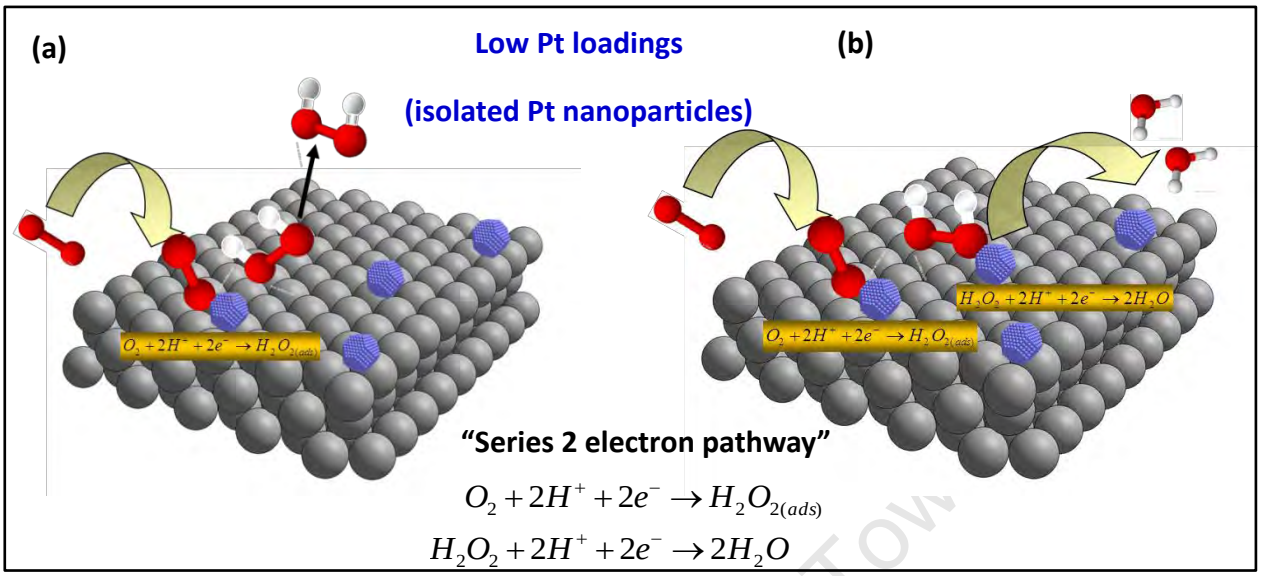

Figure 5.25 : H_2O_2 formation on low platinum loading supported catalysts forming (a) H_2O_2 as the final product of the reaction by a 2 electron pathway and (b) formation of H_2O as the final reaction product by a series 2 electron pathway with a H_2O_2 intermediate (Adapted from Fabbri *et al.*, 2013)

Figure 5.25 (a) illustrates how an adsorbed H_2O_2 species is formed on the surface of an active platinum nanoparticle by a 2 electron transfer process. The H_2O_2 molecule then desorbs from the platinum surface and diffuses into the bulk solution. Since the H_2O_2 species did not come into contact with a neighbouring active platinum nanoparticle, it could not be further reduced to H_2O. Thus the efficiency of the ORR was reduced by this process. Alternatively in Figure 5.25 (b), the desorbed H_2O_2 molecule encounters an active platinum site before diffusion into the bulk solution. Hence it is further reduced to H_2O by a transfer of 2 electrons. This overall "series" pathway still results in a 4 electron transfer and as such the ORR efficiency is not reduced in this case.

It is important therefore for each H_2O_2 molecule formed and desorbed from the platinum surface, to encounter a neighbouring platinum active site for further reduction to H_2O. Thus it can be inferred from this argument that the higher the platinum loading, the closer each platinum nanoparticle to its neighbour and hence the greater the probability of a H_2O_2 molecule being further reduced to H_2O by a neighbouring platinum active site. Figure 5.26 illustrates this process.

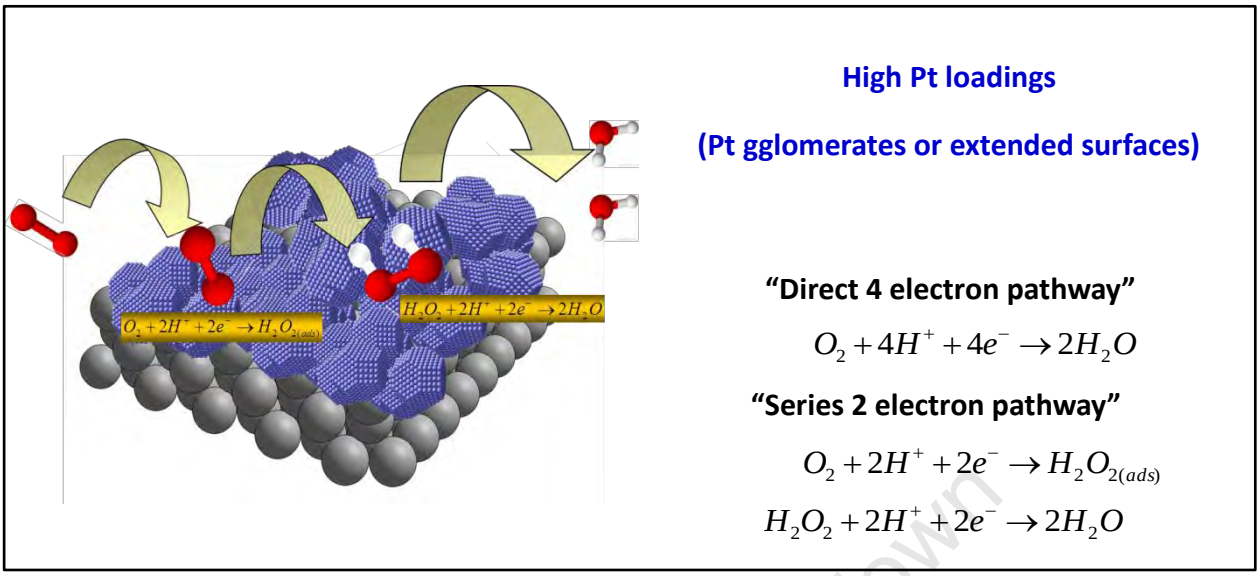

Figure 5.26 : Oxygen reduction reaction pathway on high platinum loading catalysts, via a direct 4 electron pathway or by a series 2 electron pathway (Fabbri, 2013)

Figure 5.26 above illustrates how the probability of any H_2O_2 molecule formed coming in contact with a neighbouring platinum active site after desorption is high. This theory is in line with the H_2O_2 formation results observed for both the sputtered model electrodes and the MOCVD catalysts (Sections 5.2.5 and 5.3.3). As the platinum loading is increased, the proximity of platinum particles to one another decreases, and the probability of a H_2O_2 molecule being further reduced to H_2O_2 is increased. This is seen by the reduced ring currents observed for the high loading samples.

It is difficult however to investigate the particle size effect on H_2O_2 formation, independent of other variables. There are many parameters which influence H_2O_2 formation such as inter-particle distance, carbon support contribution and H_2O_2 reaction pathway. Antoine & Durand (2000), found that the carbon support itself made a significant contribution to the amount of H_2O_2 formed during the ORR.

Therefore although this study indicates a dependence of H_2O_2 formation on particle size, it cannot be concluded that this is the only effect at play. Hence further investigations into this phenomena must be carried out in such a way as to isolate the different variable and determine their effect on H_2O_2 formation. This study has opened up new areas of interest for gaining a better insight into the properties that affect H_2O_2 formation and is a good starting point for further investigation.

University of Cape Town

5.5 Summary and comparison of model and practical catalyst systems

There are many similarities between the results obtained from the sputtered model electrode study and the MOCVD catalyst study. Although the two catalyst systems cannot be quantitatively compared, they can be qualitatively compared, and as such it was found that both systems showed an increasing ECSA trend with increasing Pt loading. The ECSA calculated by the H_{upd} method and by CO stripping were found to be comparable at higher Pt loadings in both the model and MOCVD catalyst system, this was indicated by a $ECSA_{Hupd}/ECSA_{CO\ stripping}$ ratio approximately equal to one. At low platinum loadings the exposure and hence the capacitive effect of the carbon support is more significant than for higher Pt loadings, this leads to inaccuracies in the H_{upd} area calculation as the double layer charge is so large relative to the H_{upd} area.

One of the most significant findings that was determined in both the model and practical catalyst system, was the occurrence of multiple CO oxidation peaks observed during CO stripping voltammetry measurements. Based on the abundant literature supporting the stance that the double voltammeric peak is indicative of the presence of isolated platinum nanoparticles and platinum agglomerates or in general, a difference in surface structure respectively, it can be concluded that the findings in this study are in line with the literature on the topic. As the platinum loading increases in both the sputtered model system and the MOCVD catalyst system, there is an increase in the amplitude of the low potential peak (Pt agglomerates) relative to the high potential peak (isolated particles), as the platinum loading is increased. There is further evidence of a particle size increase and particle agglomeration at high Pt loadings, seen by the increased particle size determined by XRD for the case of the MOCVD catalysts and the TEM and SEM images also show visually an increase in particle size and agglomeration as platinum loading increases in both systems. These results are significant as they could provide a platform for the quantitative determination of the extent of particle agglomeration in a specific catalyst system. It is also evident from this study that the intrinsic control of the structural properties of platinum particles is necessary to attain a better understanding of how particle size and surface structure affect the electrocatalytic properties of the catalyst itself.

In terms of catalytic activity of the two different catalysts systems, the kinetic current (i_k) was observed to increases with platinum loading. This is expected as there are effectively more active platinum sites available for the oxygen reduction reaction to occur at higher platinum loadings. It was also noted that the oxygen reduction reaction diffusion limiting current was not reached by the low loading model electrodes (2 and 10 $\mu g/cm^2$) and for the low wt.% Pt MOCVD catalysts (20 and 40 wt.% Pt). This finding could be explained through the use of RRDE measurements. It was found that H_2O_2 production was generally greater on the low loading model electrodes and the low wt.% Pt MOCVD catalysts. This could explain the reduced ORR current observed for these samples, as H_2O_2 formation is effectively a 2 electron process, therefore the greater the

University of Cape Town

amount of H_2O_2 detected the less efficient the 4 electron ORR will be. There are several reasons to explain the increased H_2O_2 that have been discussed throughout the literature, the effect of particle size and interparticle distance are not mutually exclusive so it is difficult to pinpoint which variable is accountable for the increased H_2O_2 formation observed, however it is likely that both variables contribute (Nesselberger *et al*., 2013). This is in line with the observations of higher H_2O_2 formation at low platinum loadings and hence smaller platinum particle sizes, see Section 5.4.6 for a detailed explanation on this phenomenon.

The main differences observed between the model electrode study and the MOCVD catalyst system were that an extended surface was not achieved in the case of the MOCVD catalysts and the area specific activity ($i_{k,spec}$) of the MOCVD catalysts was seen to decrease while that of the sputtered electrode system increased with platinum loading. This could indicate the limitations of the range of catalysts prepared for the MOCVD system. The ideal MOCVD model developed in Section 5.4 predicted a continuous platinum surface at a platinum loading on carbon of 86 wt.% Pt. The prepared MOCVD catalysts did not exceed 80 wt.% Pt and it is only speculation that higher loadings may have seen an increase in specific activity as in the model electrode system. This would have to be verified by further investigations.

This study has formed a basis for further investigations into more specific areas of the electrochemical behaviour of different platinum surfaces created by varying platinum loading, on different parameters such as particle size, ECSA, catalytic activity and hydrogen peroxide formation. It would be particularly useful to create a directly comparable model electrode system to a practical system such as the MOCVD system developed in this study. In that way the quantitative comparison may be useful in defining the limitations of the model system or the practical catalyst system

University of Cape Town

6. CONCLUSIONS

This study has overseen the development of a model catalyst system and a corresponding practical MOCVD prepared catalysts system. The results have proven to be reproducible and many of the findings have been in line with similar findings in the literature.

One of the most significant findings is related to the CO stripping voltammetry, the double voltammeric peak observed could be attributed to the presence of isolated platinum nanoparticles and platinum agglomerates. The low potential peak pertaining to platinum agglomerates was seen to increase in amplitude as platinum loading increased, and the corresponding high potential peak decreased in amplitude with platinum loading. Physical characterisation showed that as the platinum content increased in both the model system and the MOCVD catalysts system, the average particle size increased, indicating agglomeration, thus supporting the findings of the CO stripping voltammetry. CO stripping voltammetry is a potential quantitative measure of particle agglomeration in platinum supported on carbon catalyst systems.

Hydrogen peroxide formation was observed in both systems at potentials below 0.8 V vs. SHE. The most significant H_2O_2 formation was observed for the low loading sputtered model electrodes and the low platinum weight % MOCVD catalysts. H_2O_2 formation is a plausible reason for the reduced diffusion limiting currents observed for the low loading model electrodes and MOCVD catalysts. The CO stripping results combined with the RRDE findings allude to a particle size effect taking place as platinum loading is increased in both the model and MOCVD catalyst system.

There still remains a considerable scope of unanswered questions with reference to particle size effects, however there have been many parallels in this study with well documented and undisputed literature (Maillard *et al.,* (2005); Mayrhofer *et al.,* (2005); Katsounaros *et al.,* (2012) & Ciapina *et al.,* (2010)). Particular interest in creating extended platinum surfaces could be investigated as the properties of such surfaces have proven to have several advantages in this study including reduced hydrogen peroxide formation and high specific activities ($i_{k,\ spec}$) relative to dispersed platinum nanoparticles. This study could serve as a compass for further investigations into the particle size effects and the electrocatalytic properties of extended platinum surfaces.

University of Cape Town

7. APPENDIX

7.1 Particle size distribution determined by TEM

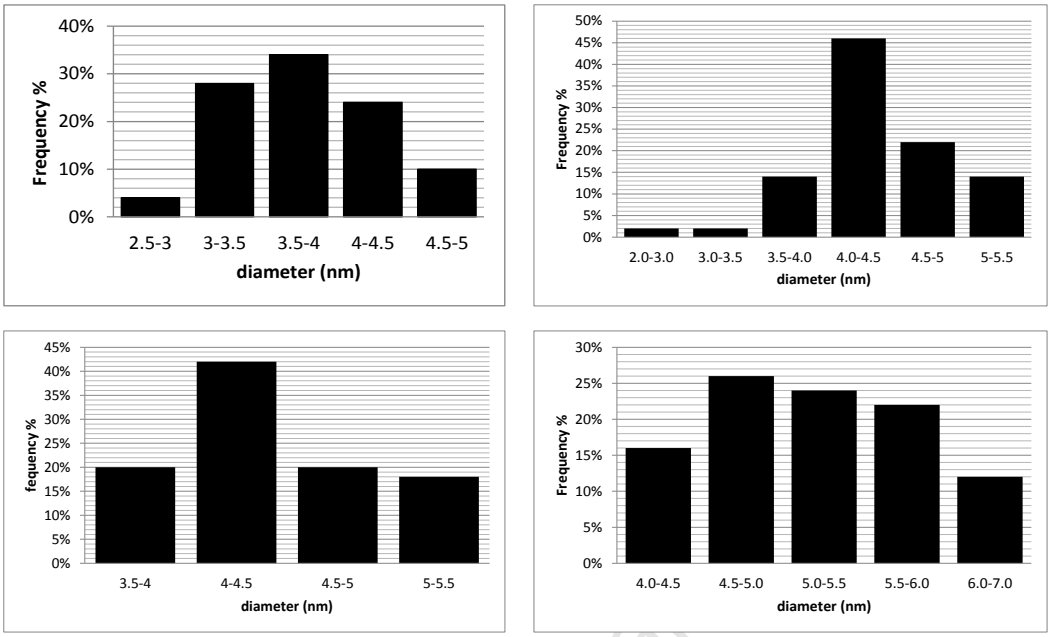

Figure 7.1 : Particle size distributions for MOCVD catalyst detrmined using TEM images

7.2 Deconvolution of CO stripping peaks – MOCVD

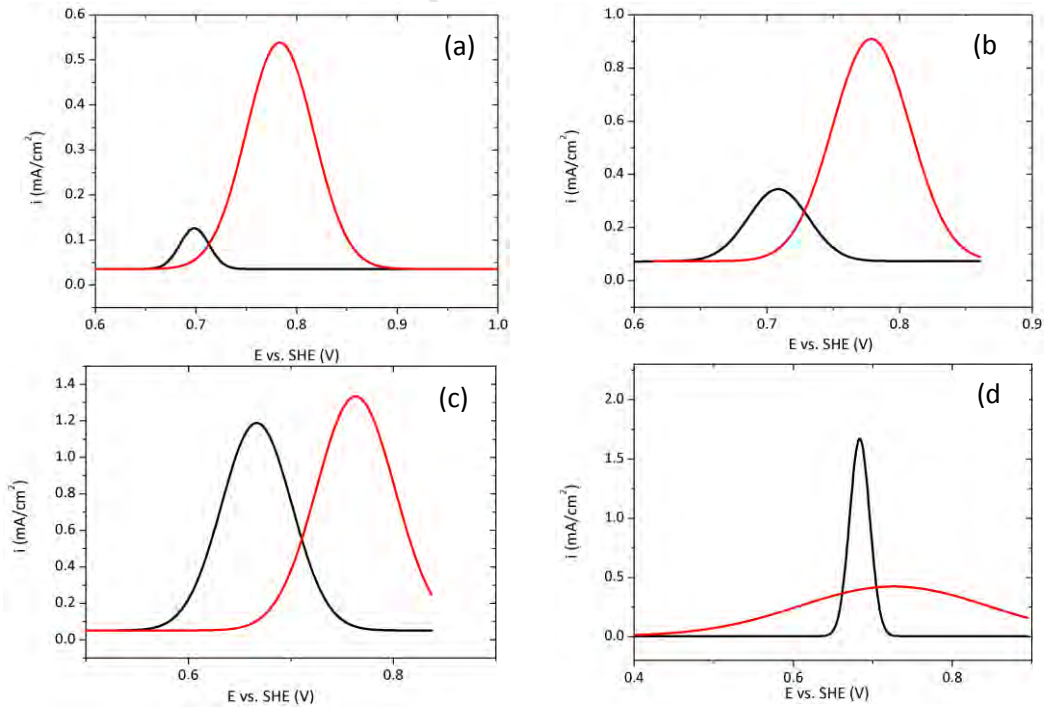

Figure 7.2 : Deconvoluted CO stripping peaks for MOCVD catalysts with (a) 20 wt.% Pt, (b) 40 wt.% Pt, (c) 60 wt.% Pt and (d) 80 wt. % Pt. Black line represents low potential peak and red curve represents the high potential peak.

8. REFERENCE LIST

.

Aksoylu, E.; Faria, J. L.; Pereira, M. F. R.; Figueiredo, J. L.; Serp, P.; Hierso, J. C.; Feurer, R.; Kihn, Y. & Kalck, P. (2003), "Highly dispersed activated carbon supported platinum catalysts prepared by OMCVD: a comparison with wet impregnated catalysts", Applied Catalysis A: General, **243**, pp. 357-365.

Alia, S. M.; Zhang, G.; Kisailus, D.; Li, D.; Gu, S.; Jensen, K. & Yan, Y. (2010), "Porous Platinum Nanotubes for Oxygen Reduction and Methanol Oxidation Reactions", Advanced Functional Materials, **20**, pp. 3742-3746.

Antoine, O. & Durand, R. (2000), "RRDE study of oxygen reduction on Pt nanoparticles inside Nafion : H_2O_2 production in PEMFC cathode conditions", pp. 839-844.

Auer, E.; Freund, A.; Pietsch, J. & Tacke, T. (1998), "Carbons as supports for industrial precious metal catalysts", **173**, pp.

Bahlawane, N.; Kohse-h, K.; Premkumar, A. & Lenoble, D. (2012), "Advances in the deposition chemistry of metal-containing thin films using gas phase processes", pp. 929-941.

Barbir, F. (2005), "PEM Fuel Cells: Theory and Practice", Elsevier Academic Press.

Bard, A. J. & Faulkner, L. R. (2001), "Electrochemical Methods: Fundamentals and Applications", 2nd ed. Massachusett, John Wiley & Sons, Inc.

Battiston, G.; Gerbasi, R. & Rodriguez (2005), "A Novel Study of the Growth and Resistivity of Nanocrystalline Pt Films Obtained from Pt(acac)2 in the Presence of Oxygen or Water Vapor", Chemical Vapor Deposition, **11**, pp. 130-135.

Bett, J.; Lundquist, J.; Washington, E. & Stonehart, P. (1973), "Platinum crystallite size considerations for electrocatalytic oxygen reduction—I", Electrochimica Acta, **18**, pp. 343-348.

Borup, R.; Meyers, J.; Pivovar, B.; Kim, Y. S.; Mukundan, R.; Garland, N.; Myers, D.; Wilson, M.; Garzon, F.; Wood, D.; Zelenay, P.; More, K.; Stroh, K.; Zawodzinski, T.; Boncella, J.; McGrath, J. E.; Inaba, M.; Miyatake, K.; Hori, M.; Ota, K.; Ogumi, Z.; Miyata, S.; Nishikata, A.; Siroma, Z.; Uchimoto, Y.; Yasuda, K.; Kimijima, K.-I. & Iwashita, N. (2007), "Scientific aspects of polymer electrolyte fuel cell durability and degradation", Chemical reviews, **107**, pp. 3904-3951.

Chen, S. & Kucernak, A. (2004), "Electrocatalysis under conditions of high mass transport rate: Oxygen reduction on single submicrometer-sized Pt particles supported on carbon", The Journal of Physical Chemistry B, **108**, pp. 3262-3276.

Chu, H. P.; Lei, L.; Hu, X.; Yue, P.-l.; Bay, C. W. & Kong, H. (1998), "Metallo-Organic Chemical Vapor Deposition (MOCVD) for the Development of Heterogeneous Catalysts", pp. 1108-1113.

University of Cape Town

Ciapina, E. G.; Santos, S. F. & Gonzalez, E. R. (2010), "The electrooxidation of carbon monoxide on unsupported Pt agglomerates", Journal of Electroanalytical Chemistry, **644**, pp. 132-143.

Climent, V. & Feliu, J. M. (2011), "Thirty years of platinum single crystal electrochemistry", pp. 1297-1315.

Debe, M. K. (2012), "Nanostructured Thin Film Electrocatalysts for PEM Fuel Cells – A Tutorial on the Fundamental Characteristics and Practical Properties of NSTF Catalysts", Journal of The Electrochemical Society, **c**, pp. 47-68.

Kurt J. Lesker (2013) RF magnetron sputtering system for deposition of transparent conductive oxides Delft University of Technology

Fabbri, E. (2013) Electrochemical investigation of Pt model electrodes for application in polymer electrolyte fuel cells (PEFCs). Powerpoint presentation. Paul Scherrer Institute. Switzerland

Ferreira, P. J.; la O', G. J.; Shao-Horn, Y.; Morgan, D.; Makharia, R.; Kocha, S. & Gasteiger, H. a. (2005), "Instability of Pt⁄C Electrocatalysts in Proton Exchange Membrane Fuel Cells", Journal of The Electrochemical Society, **152**, pp. A2256-A2256.

Garsany, Y.; Singer, I. L. & Swider-Lyons, K. E. (2011), "Impact of film drying procedures on RDE characterization of Pt/VC electrocatalysts", Journal of Electroanalytical Chemistry, **662**, pp. 396-406.

Gasteiger, H. A.; Kocha, S. S.; Sompalli, B. & Wagner, F. T. (2005), "Activity benchmarks and requirements for Pt, Pt-alloy, and non-Pt oxygen reduction catalysts for PEMFCs", Applied Catalysis B: Environmental, **56**, pp. 9-35.

Gottesfeld, S. & Zawodzinski, T. A. (1997), "Polymer Electrolyte Fuel Cells", *In:* Alkire, R. C. & Tobias, C. W. (eds.) *Advances in Electrochemical Science and Engineering*. John Wiley & Sons.

Inaba, M., Yamada, H., Tokunaga, J., & Tasaka, A. (2004), "Effect of Agglomeration of Pt/C Catalyst on Hydrogen Peroxide Formation", Electrochemical and Solid-State Letters, pp. A474.

Jones, A. C. & Hitchman, M. L. (2009), "Overview of Chemical Vapour Deposition".

Karakoc, H.; Midilli, A. & Turan, O. (2013), "Green hydrogen and fuel cell systems", International journal of Energy Research, pp. 3037-3037.

Katsounaros, I.; Schneider, W. B.; Meier, J. C.; Benedikt, U.; Biedermann, P. U.; Auer, A. a. & Mayrhofer, K. J. J. (2012), "Hydrogen peroxide electrochemistry on platinum: towards understanding the oxygen reduction reaction mechanism", Physical chemistry chemical physics : PCCP, **14**, pp. 7384-7391.

Ke, K.; Hiroshima, K.; Kamitaka, Y.; Hatanaka, T. & Morimoto, Y. (2012), "Electrochimica Acta An accurate evaluation for the activity of nano-sized electrocatalysts by a thin-film rotating disk electrode : Oxygen reduction on Pt / C", **72**, pp. 120-128.

University of Cape Town

Kibsgaard, J.; Gorlin, Y.; Chen, Z. & Jaramillo, T. F. (2012), "Meso-structured platinum thin films: active and stable electrocatalysts for the oxygen reduction reaction", Journal of the American Chemical Society, **134**, pp. 7758-7765.

Kinoshita, K. (1990), "Particle Size Effects for Oxygen Reduction on Highly Dispersed Platinum in Acid Electrolytes", Society, E, pp. 137(133), 133-136.

Komatsu, K.-i. & Osawa, M. (2009), "Dynamics of CO Oxidation on a Polycrystalline Platinum Electrode : A Time-Resolved", pp. 10222-10228.

Kongkanand, a.; Dioguardi, M.; Ji, C. & Thompson, E. L. (2012), "Improving Operational Robustness of NSTF Electrodes in PEM Fuel Cells", Journal of The Electrochemical Society, **159**, pp. F405-F411.

Kounaves, S. P. (1997), "Voltammetric Techniques", pp. 709-726.

Maillard, F.; Schreier, S.; Hanzlik, M.; Savinova, E. R.; Weinkauf, S.; Stimming, U. & Federation, R. (2005), "Influence of particle agglomeration on the catalytic activity of carbon-supported Pt nanoparticles in CO monolayer oxidation", pp. 385-393.

Mayrhofer, K. J. J.; Blizanac, B. B.; Arenz, M.; Stamenkovic, V. R.; Ross, P. N. & Markovic, N. M. (2005), "The Impact of Geometric and Surface Electronic Properties of Pt-Catalysts on the Particle Size Effect in Electrocatalysis", Journal of Physical Chemistry, pp. 14433-14440.

Mayrhofer, K. J. J.; Strmcnik, D.; Blizanac, B. B.; Stamenkovic, V.; Arenz, M. & Markovic, N. M. (2008), "Measurement of oxygen reduction activities via the rotating disc electrode method : From Pt model surfaces to carbon-supported high surface area catalysts", **53**, pp. 3181-3188.

McBreen, J. (1985), "Voltammetric Studies of Electrodes in Contact with Ionomeric Membranes", Journal of The Electrochemical Society, **132(5)**, pp. 1112-1116.

Meier, J. C.; Galeano, C.; Katsounaros, I.; Topalov, A. A.; Kostka, A.; Schu, F. & Mayrhofer, K. J. J. (2012), "Degradation Mechanisms of Pt/C Fuel Cell Catalysts under Simulated Start–Stop Conditions", pp.

Mukerjee, S. (1989), "Paticle size and structural effects in platinum electrocatalysis", Journal of applied electrochemistry, pp. 537-548.

Nesselberger, M.; Ashton, S.; Meier, J. C.; Katsounaros, I.; Mayrhofer, K. J. J. & Arenz, M. (2011), "The Particle Size Effect on the Oxygen Reduction Reaction Activity of Pt Catalysts : Influence of Electrolyte and Relation to Single Crystal Models", pp. 17428-17433.

Nesselberger, M.; Roefzaad, M.; Fayçal Hamou, R.; Ulrich Biedermann, P.; Schweinberger, F. F.; Kunz, S.; Schloegl, K.; Wiberg, G. K. H.; Ashton, S.; Heiz, U.; Mayrhofer, K. J. J. & Arenz, M. (2013), "The effect of particle proximity on the oxygen reduction rate of size-selected platinum clusters", Nature materials, **12**, pp. 1-6.

University of Cape Town

Niinisto, L. (2000), "Studies of metallic thin film growth in an atomic layer epitaxy", pp. 151-158.

Paulus, U. A.; Veziridis, Z.; Schnyder, B.; Kuhnke, M.; Scherer, G. G. & Wokaun, A. (2003), "Fundamental investigation of catalyst utilization at the electrode / solid polymer electrolyte interface Part I . Development of a model system", **541**, pp. 77-91.

Peuckert, M. (1986), "Oxygen Reduction on Small Supported Platinum Particles", Journal of The Electrochemical Society, **133**, pp. 944-944.

Qi, Z. (2008), "Electrochemical Method for Catalyst Activity Evaluation", *In:* Zhang, J. (ed.) *PEM Fuel Cell Electrocatalysts and Catalyst Layers*. London: Springer.

Rabis, A.; Rodriguez, P. & Schmidt, T. J. (2012), "Electrocatalysis for Polymer Electrolyte Fuel Cells : Recent Achievements and Future Challenges", pp.

Sattler, M. L. & Ross, P. N. (1986), "The surface structure of Pt crystallites supported on carbon black", Ultramicroscopy, **20**, pp. 21-28.

Schmidt, T. J.; Gasteiger, H.; Stab, G.; Urban, P.; Kolb, D. M. & Behm, R. J. (1998), "Characterization of High-Surface-Area Electrocatalysts Using a Rotating Disk Electrode Configuration 1", **145**, pp. 2354-2358.

Schwanitz, B.; Rabis, A.; Horisberger, M. & Scherer, G. G. (2012), "Sputtered Cathodes for Polymer Electrolyte Fuel Cells : Insights into Potentials , Challenges and Limitations", Chimia, **66**, pp. 110-119.

Shao, M.; Peles, A. & Shoemaker, K. (2011), "Electrocatalysis on Platinum Nanoparticles : Particle Size Effect on", pp. 3714-3719.

Sharma, S. & Pollet, B. G. (2012), "Support materials for PEMFC and DMFC electrocatalysts—A review", Journal of Power Sources, **208**, pp. 96-119.

Sheng, W.; Chen, S.; Vescovo, E. & Shao-horn, Y. (2012), "Size Influence on the Oxygen Reduction Reaction Activity and Instability of Supported Pt Nanoparticles", **159**, pp. 96-103.

Sinha, P. K.; Wenbin, G. U.; Kongkanand, A. & Thompson, E. (2011), "Performance of Nano Structured Thin Film (NSTF) Electrodes under Partially-Humidified Conditions", Journal of The Electrochemical Society, **158**, pp.

Slavcheva, E.; Ganske, G.; Topalov, G.; Mokwa, W. & Schnakenberg, U. (2009), "Effect of sputtering parameters on surface morphology and catalytic efficiency of thin platinum films", Applied Surface Science, **255**, pp. 6479-6486.

Stonehart, P. & Ross, P. N. (1976), "The use of porous electrodes to obtain kinetic rate constants for rapid reactions and adsorption isotherms of poisons", Electrochimica Acta, **21**, pp. 441-445.

Thurier, C. & Doppelt, P. (2008), "Platinum OMCVD processes and precursor chemistry", **252**, pp. 155-169.

University of Cape Town

van Hardeveld, R. & Hartog, F. (1972), "Influence of Metal Particle Size in Nickel-on-Aerosil Catalysts on Surface Site Distribution, Catalytic Activity, and Selectivity", *In:* D.D. Eley, H. P. & Paul, B. W. (eds.) *Advances in Catalysis*. Academic Press.

Wang, J. X.; Inada, H.; Wu, L.; Zhu, Y.; Choi, Y.; Liu, P.; Zhou, W.-P. & Adzic, R. R. (2009), "Oxygen reduction on well-defined core-shell nanocatalysts: particle size, facet, and Pt shell thickness effects", Journal of the American Chemical Society, **131**, pp. 17298-17302.

Watanabe, M.; Makita, K.; Usami, H. & Motoo, S. (1986), "New preparation method of a high performance gas diffusion electrode working at 100% utilization of catalyst clusters and analysis of the reaction layer", Journal of Electroanalytical Chemistry and Interfacial Electrochemistry, **197**, pp. 195-208.

Watanabe, M.; Tryk, D. a.; Wakisaka, M.; Yano, H. & Uchida, H. (2012), "Overview of recent developments in oxygen reduction electrocatalysis", Electrochimica Acta, pp.

Wroblowa, H. S.; Yen Chi, P. & Razumney, G. (1976), "Electroreduction of oxygen: A new mechanistic criterion", Journal of Electroanalytical Chemistry and Interfacial Electrochemistry, **69**, pp. 195-201.

Wu, J.; Yuan, X.; Wang, H.; Blanco, M.; Martin, J. & Zhang, J. (2008), "Diagnostic tools in PEM fuel cell research: Part I Electrochemical techniques", International Journal of Hydrogen Energy, **33**, pp. 1735-1746.

Xu, Z.; Zhang, H.; Zhong, H.; Lu, Q.; Wang, Y. & Su, D. (2012), "Effect of particle size on the activity and durability of the Pt/C electrocatalyst for proton exchange membrane fuel cells", Applied Catalysis B: Environmental, **111-112**, pp. 264-270.

Yang, H.; Kumar, S. & Zou, S. (2013), "Electroreduction of O2 on uniform arrays of Pt nanoparticles", Journal of Electroanalytical Chemistry, **688**, pp. 180-188.

Zainoodin, A. M.; Kamarudin, S. K. & Daud, W. R. W. (2010), "Electrode in direct methanol fuel cells", International Journal of Hydrogen Energy, **35**, pp. 4606-4621.

Zhang, S., Shao, Y., Yin, G., & Lin, Y. (2013), "Recent progress in nanostructured electrocatalysts for PEM fuel cells", Journal of Materials Chemistry A, pp. 4631.

Zhang, S.; Yuan, X.-Z.; Hin, J. N. C.; Wang, H.; Friedrich, K. A. & Schulze, M. (2009), "A review of platinum-based catalyst layer degradation in proton exchange membrane fuel cells", Journal of Power Sources, **194**, pp. 588-600.

University of Cape Town